New Approaches to Particle Spectra in Lattice QCD

Robert M. Baxter

Submitted for the degree of

Doctor of Philosophy

University of Edinburgh

1993

To my parents,
for their support
and encouragement
over all these years,

and

to Alison,
without whom...

Abstract

I present a series of calculations of the spectrum of low-lying hadron states using the formalism of lattice QCD. I discuss the approach taken by the UKQCD Collaboration in the simulation of QCD on the Grand Challenge supercomputer at Edinburgh, and the use of an improved action to reduce the discretisation errors of the computer model.

I describe the techniques used in calculating hadron masses and decay constants from first principles and discuss the implementation of a spectrum-analysis program on the massively-parallel Grand Challenge machine.

I introduce a new method of smearing hadron operators to improve their signals in simulations and describe the development and implementation of the Jacobi smearing algorithm.

I present the results of UKQCD's light hadron spectrum calculations, including a new method of analysing $SU(3)$ flavour symmetry breaking for hadrons composed of non-degenerate quarks. I discuss the calculation of the masses of hadrons composed of u, d and s quarks and present mass estimates for the a_0, a_1, b_1, K^*, ϕ and η_s mesons and the nucleon, Ξ, Σ, $\Delta(\frac{3}{2})$, Ω, $\Delta(\frac{1}{2})$, $\tilde{N}$ and $\tilde{\Delta}(\frac{3}{2})$ baryons.

Finally, I extend the ideas of combining degenerate and non-degenerate datasets to include calculations of mesons composed of one heavy and one light quark. I indicate how the quark mass dependence of the pseudoscalar and vector mesons may be described by a single function for the regime $0 \leq m_{quark} \lesssim m_{charm}$. Using this method, I present mass estimates for the D, D^*, D_s, D_s^*, η_c and J/Ψ mesons.

Declaration

This thesis has been composed, wholly and solely, by me and contains my own work, except as indicated below.

The computer program described in Chapter 2 is a product of the work of many people, including Stephen Booth, Ken Bowler, Craig McNeile, David Richards, Alan Simpson, and myself. The study described in Chapter 3 was performed with the guidance of David Henty. The running of Maxwell which produced the data for me to analyse for Chapters 4 and 5 was performed by many good people at Edinburgh, most especially all those listed above. The analysis programs used in these final chapters derive in part from codes produced by Jim Simone.

Some of the work presented in Chapter 3 has been published in

- C.R. Allton et al. (UKQCD Collaboration), Phys. Rev. **D47** (1993) 5128.

Some of the results in Chapter 4 are to appear in

- C.R. Allton et al. (UKQCD Collaboration), Phys. Rev. **D**, to be published.

Other works to which I have contributed:

- C.R. Allton et al. (UKQCD Collaboration), Phys. Lett. **B 284** (1992) 377.
- C.R. Allton et al. (UKQCD Collaboration), Nucl.Phys. **B**, to be published.

Robert M. Baxter.

Acknowledgements

I suspect that everyone who arrives at this point in finishing a thesis must look back over the three ($N\ldots$) years and ask *am I glad I did it?* With me, the answer is a definite *yes*, and much of the reason lies with the many good people I have worked with during my time at Edinburgh.

My thanks, first, to my supervisors, Richard Kenway and Ken Bowler, for their support and encouragement, and not least their keen-eyed reading of this thesis. I am grateful to them for providing the belief and faith which I sometimes failed to find myself.

My gratitude, also, to the people with whom I have worked most closely as part of the EDQCD family — Stephen Booth, Sara Collins, David Henty, Craig McNeile, Brian Pendleton, David Richards, Jim Simone, Alan Simpson and Barry Wilkes. Their's has been the burden of answering many stupid questions over the years, and of teaching me (almost) everything I know about QCD, C, UNIX, statistics, Mexican food...

Perhaps my greatest thanks must go to three people outwith the arena of physics; to Mum and Dad for unswerving encouragement and enthusiasm over many years of education, even when they didn't know what I was talking about, and to my fiancée Alison, who makes everything worthwhile...

Contents

Abstract i

Declaration ii

Acknowledgements iii

1 The Lattice Formulation of QCD **1**

1.1 QCD — A Brief Look 1

1.2 The Lattice Action 2

1.2.1 The gluon term, S_G 4

1.2.2 The fermion term, S_F 4

1.3 The Path Integral 6

1.4 The UKQCD Programme 7

1.4.1 Gauge configurations 8

1.4.2 The clover action for quarks 9

1.4.3 UKQCD spectroscopy — a summary 10

1.5 The Problems of Lattice QCD 11

1.5.1 Finite lattice spacing — a case for improvement 11

1.5.2 Signals and statistics — a case for smearing 11

1.5.3 Quenching — a case for dynamical simulations? 11

1.5.4 Heavy quarks and small volumes — a case for bigger computers 12

2 Hadron Spectroscopy on the Lattice 14

2.1 A Fundamental Goal 14

2.2 Theoretical Considerations 15

2.3 Definitions of Hadronic Operators 17

2.3.1 Meson operators 17

2.3.2 Baryon operators 19

2.4 Computational Refinements 20

2.4.1 Approximating the limit $t \to \infty$ 22

2.4.2 Making contact with the "real world" 22

2.4.3 A prescription for spectrum calculations 24

2.5 Development of Parallelised Spectrum Codes 24

2.5.1 Overview 25

2.5.2 Code conventions 27

2.5.3 3-d neighbour tables 28

2.5.4 Phase factors for $\vec{k} \neq \vec{0}$ 30

2.5.5 Propagator formats and reordering 31

2.6 The State of the Art 31

2.6.1 Quenched Wilson calculations 31

2.6.2 Quenched staggered calculations 33

2.6.3 Summary of progress 33

3 Jacobi Smearing **35**

3.1 What is Smearing? 35

3.2 Rationale Behind Gauge-Covariant Smearing 36

3.3 Source and Sink Smearing 37

3.4 Wuppertal Smearing 40

3.4.1 Free-field Wuppertal smearing in the continuum 41

3.4.2 Wuppertal smearing on the lattice 42

3.5 The Jacobi Smearing Algorithm 45

3.5.1 Dependence of $S(x, y)$ on κ_{sc} and N 47

3.6 Effects of Smearing 54

3.7 Summary 56

4 Results for Light-Hadron Spectroscopy **58**

4.1 Statistics and Fitting Procedure 58

4.1.1 Fit functions for hadron correlators 59

4.1.2 Correlated-χ^2 fitting 60

4.1.3 Statistical errors 62

4.1.4 Determination of t-fit ranges 62

4.2 Examination of Systematic Errors 69

4.3 Spectrum Data in Lattice Units 73

4.4 Quark Mass Dependence 77

4.5 Chiral Extrapolations 80

4.6 Strange Quark Mass 85

4.7 Results in Physical Units — the Light and Strange Regimes 86

4.8 A Digression — the R Parameter in Chiral Perturbation Theory . 92

5 Combining Light- and Heavy-Quark Spectroscopy 98

5.1 Data in the Heavy-Light Regime 98

5.2 Combined Extrapolations 101

5.2.1 SS versus LS data 103

5.2.2 Quark mass dependence 103

5.2.3 κ_{crit}, κ_s and $a^{-1}(m_\rho)$ 104

5.2.4 How far can we go? 106

5.3 Charm Quark Mass 108

5.4 Results from Combined Data Sets 110

6 Summary and Conclusions 114

Bibliography 118

Out yonder was this huge world,
which exists independently of us human beings
and which stands before us like a great, eternal riddle,
at least partially accessible to our inspection and thinking.
The contemplation of this world beckoned
like a liberation.

Albert Einstein.

Chapter 1

The Lattice Formulation of QCD

In this chapter I present a brief introduction to the basics of QCD, followed by a prècis of the lattice formulation. I describe the background to the hadron spectrum programme of the UKQCD Collaboration and, finally, give a brief discussion of some of the problems that arise in simulating QCD on a computer.

1.1 QCD — A Brief Look

QCD — quantum chromodynamics — is a theory of the interactions of quarks and gluons, the "strong nuclear" interactions of particle physics. It is perhaps surprising that in the twenty years since its inception [1, 2, 3] it has not yet become *the* theory of the strong interaction, although it is, as they say, real close.

A major reason for this "almost-but-not-quite" status is that QCD is a difficult theory to solve. The perturbative methods applied with such astounding success to quantum *electro*dynamics rely on the fact that the coupling constant between electrons and photons is a small number ($\mathcal{O}(1/137)$). The corresponding number in QCD is $\mathcal{O}(1)$ at the energy scales of the everyday world. However, the QCD coupling possesses the quality of *decreasing* at short distance — a feature of the self-interacting Yang-Mills fields that describe gluons — and hence the important strong interaction property of *asymptotic freedom* can be analysed using perturbative QCD.

The other major feature of the strong interaction, *confinement* cannot be obtained from perturbative analyses— you start with a theory of free quarks and gluons, do perturbation theory, and you finish up with a theory of free quarks and gluons. Nowhere along the line do quark-gluon bound states — hadrons — leap off the page. The long distance behaviour of QCD demands non-perturbative methods to solve, and herein lies the major stumbling block and the motivation for the lattice formulation.

Perturbative QCD, then, is fine for analysing short-distance, high-energy phenomena such as Bjorken scaling; for QCD to be recognised truly as the theory of strong interactions it must be able to predict medium and low energy results such as quark confinement and the hadron spectrum. This entails non-perturbative approaches, leading to computer simulation and numerical calculations, and *this* is lattice QCD.

Below, I present a brief discussion of the formulation of lattice QCD suitable for computer modelling. For detailed reviews of the subject, I direct readers to references [4, 5].

1.2 The Lattice Action

The Lagrangian of continuum QCD is

$$\mathcal{L} = \bar{\psi}\left(\not{D} + m\right)\psi + \tfrac{1}{4}F_{\mu\nu}F^{\mu\nu}; \tag{1.1}$$

ψ and $\bar{\psi}$ are the fermionic fields representing quarks and $F_{\mu\nu}$ is the gluon field strength tensor, defined as

$$F_{\mu\nu} \equiv \partial_\mu A_\nu - \partial_\nu A_\mu - ig\left[A_\mu, A_\nu\right],$$

for gluon field operators A_μ and coupling g. In the lattice theory, ideas are more easily expressed in terms of the action

$$S \equiv \int d^4x\mathcal{L} \tag{1.2}$$

which we may divide into a purely gluonic part involving $F_{\mu\nu}$ and a fermionic part concerning $\not{D}$:

$$S = S_G + S_F$$

The prescription for modelling this on a computer is

- discretise spacetime into a 4-dimensional lattice with lattice spacing a;
- place fermion variables on the lattice sites;
- represent the gluon fields by $SU(3)$ colour matrices on the lattice links;
- replace the covariant derivative $\not{D}$ by a finite difference.

The discretisation of spacetime may be thought of instead as the replacement of continuous field variables by some "average" field over a unit cube of small size. The introduction in this way of a minimum length scale a is equivalent to the enforcement of a maximum energy-momentum cutoff, a^{-1}; the lattice theory is thus an ultra-violet regulated theory.

The representation of the gluon fields by $SU(3)$ matrices on the lattice links follows from the demands of gauge-invariance:

> if $g \in SU(3)$ and the quark fields transform as $\psi \to g\psi$ and $\bar{\psi} \to \bar{\psi}g^{-1}$ then the fermion bilinear $\bar{\psi}(x)\psi(y)$ can be made gauge invariant by introducing the path-ordered parallel transporter
>
> $$U(x,y) = \mathcal{P}e^{ig\int_x^y A_\mu(z)dz}.$$
>
> If x and y are neighbouring sites on the lattice, the path-ordered integral runs along the connecting link, and if we approximate the integral using the midpoint rule for small $|x-y| = a$, we get
>
> $$U(x, x+a\hat{\mu}) \simeq e^{igA_\mu(x+a\hat{\mu})} \quad \in SU(3). \tag{1.3}$$

Hence, gauge invariance directs that the links be $SU(3)$ matrices. The convention is that $U_\mu(x)$ represents a link extending from x one lattice spacing in the positive μ direction and $U_\mu^\dagger(x)$ represents the same link traced in the *negative* μ direction, ie. starting at $x - a\hat{\mu}$ and finishing at x.

Gauge invariance, and the requirement that S reduce to the continuum form in the limit $a \to 0$, dictate the appearance of the terms in the lattice action.

1.2.1 The gluon term, S_G

The only gauge-invariant gluonic objects are products of links around a closed loop, the smallest of which is the *plaquette*:

$$U_\Box \equiv U_\mu(x)U_\nu(x+\hat{\mu})U^\dagger_\mu(x+\hat{\nu})U^\dagger_\nu(x), \tag{1.4}$$

where I have set $a = 1$.

The $SU(3)$ gauge action is then defined as [6]

$$S_G \equiv -\frac{\beta}{6}\sum_\Box Tr(U_\Box + U^\dagger_\Box), \tag{1.5}$$

where $\beta \equiv 6/g^2$ and the sum runs over all plaquettes on the lattice.

If one expands this, replacing an explicit a and looking at the continuum limit $a \to 0$, S_G reduces to the Yang-Mills form $\int \frac{1}{4}F_{\mu\nu}F^{\mu\nu}d^4x$, with correction terms of $\mathcal{O}(a^2)$.

1.2.2 The fermion term, S_F

Putting fermions on the lattice poses problems. The most naïve discretisation of $\bar{\psi}(\not{D} + m)\psi$, replacing $\not{D}$ with a (covariant) finite difference, produces a theory whose continuum limit contains 2^4 fermion species. This *species doubling* is an unavoidable feature of lattice-regularised theories, a statement embodied in the No-Go Theorem of Nielsen and Ninomiya [7]. One way of sidestepping the problem, proposed by Wilson [8], involves adding a term to the action that is proportional to a as $a \to 0$ and which has the effect of giving $2^4 - 1$ of the fermions masses proportional to a^{-1}. The resulting fermion action is

$$\begin{aligned} S_{WF} \;=\; & -\sum_x \Big\{ \sum_\mu \tfrac{1}{2}\bar{\psi}(x) \Big[U_\mu(x)\,(r-\gamma_\mu)\,\psi(x+\hat{\mu}) \\ & \qquad + U^\dagger_\mu(x-\hat{\mu})\,(r+\gamma_\mu)\,\psi(x-\hat{\mu})\Big] \\ & \qquad\quad + (m+4r)\bar{\psi}(x)\psi(x)\Big\}. \end{aligned} \tag{1.6}$$

The terms proportional to the number r are the *Wilson terms*, added to the naïve action to avoid the doubling problem. Usually, we set $r = 1$.

For computational purposes, S_{WF} can be rewritten in matrix form as

$$S_{WF} = \frac{1}{2\kappa}\,\bar{\psi}(x)\,M_{WF}(x,y)\,\psi(y). \tag{1.7}$$

The Wilson fermion matrix $M_{WF}(x,y)$ is defined as

$$M_{WF}(x,y) = \delta(x,y) - \kappa \not{D}(x,y) \tag{1.8}$$

where

$$\not{D}(x,y) \equiv \sum_{\mu}\Big(U_{\mu}(x)\,(r-\gamma_{\mu})\,\delta(x+\hat{\mu},y) + U^{\dagger}_{\mu}(x-\hat{\mu})\,(r+\gamma_{\mu})\,\delta(x-\hat{\mu},y)\Big), \tag{1.9}$$

and κ parametrises the quark mass. For free fermions,

$$\kappa = \frac{1}{2m+8r} \quad \Rightarrow \quad m = \frac{1}{2}\left(\frac{1}{\kappa} - \frac{1}{1/(8r)}\right).$$

κ measures the point at which the Wilson quark mass m, in units of the lattice spacing a, vanishes. This is equivalent to taking the cutoff a^{-1}, in physical units, to infinity, ie. removing it; $m \to 0$ thus defines the continuum limit. In the presence of gauge fields, the number $8r$ is replaced by κ_{crit}:

$$m = \frac{1}{2}\left(\frac{1}{\kappa} - \frac{1}{\kappa_{crit}}\right), \tag{1.10}$$

since interaction with the gauge fields adds a self-energy contribution to the lattice quark mass.

If we look at the free-field Wilson fermion matrix in momentum space we can understand how the fermion doubling problem is alleviated:

$$M_{WF}(p) = m + \sum_{\mu}\Big(i\gamma_{\mu}\sin p_{\mu} + r(1-\cos p_{\mu})\Big). \tag{1.11}$$

The inverse Fourier transform of $M^{-1}_{WF}(p)$ yields the free-fermion propagator. As $m \to 0$, the poles in the propagator occur when the $\sum_{\mu}(\ldots)$ term is zero. Without the r term, the sine function gives zeros for $p_{\mu} = 0$ *and* $p_{\mu} = \pi$, leading to doubling. The Wilson r term gives all but the $p_{\mu} = 0$ fermion an additional mass proportional to r in lattice units. Thus, the additional fermions decouple as the cutoff is removed.

The Wilson fermion action reduces to the Dirac action in the $a \to 0$ limit, but has corrections of $\mathcal{O}(a)$. These corrections can be reduced to $\mathcal{O}(a^2)$ and beyond by the addition of *improvement terms*. I shall delay discussion of improved actions until a little later.

1.3 The Path Integral

For now, though, we have successfully discretised the QCD action; we now wish to use it to calculate the hadron spectrum from first principles. The formalism most readily applicable to the lattice theory is that of the Feynman path integral. For the vacuum expectation value of an arbitrary function of the gauge and quark fields, $f(U,\psi,\bar{\psi})$, the path integral is

$$\left\langle 0 \left| f(U,\psi,\bar{\psi}) \right| 0 \right\rangle = \frac{1}{Z} \int \mathcal{D}U\, \mathcal{D}\psi\, \mathcal{D}\bar{\psi}\, f(U,\psi,\bar{\psi})\, e^{-S(U,\psi,\bar{\psi})}, \tag{1.12}$$

where Z is defined such that $\langle 0 | 1 | 0 \rangle = 1$.

The Haar measures $\mathcal{D}U$, $\mathcal{D}\psi$ and $\mathcal{D}\bar{\psi}$ are defined similarly:

$$\begin{aligned} \mathcal{D}U &= \prod_{x,\mu} dU_\mu(x) \\ \mathcal{D}\psi\mathcal{D}\bar{\psi} &= \prod_{x} d\psi(x) d\bar{\psi}(x) \end{aligned} \tag{1.13}$$

ie., $\mathcal{D}U$ is defined over every link in the lattice, and $\mathcal{D}\psi\mathcal{D}\bar{\psi}$ over every site.

The quark fields are Grassman variables and as such difficult to deal with computationally. Fortunately, for calculations of the hadron mass spectrum, one only ever needs to solve the path integral for products of quark propagators $G(x,y) = \psi(x)\bar{\psi}(y)$ (see Chapter 2). The Grassman integrals can then be done by hand:

$$\begin{aligned} \langle 0 | G(x,y) | 0 \rangle &= \frac{1}{Z} \int \mathcal{D}U\, \mathcal{D}\psi\, \mathcal{D}\bar{\psi}\, \psi(x)\bar{\psi}(y)\, e^{-S_G - \bar{\psi} M_F \psi} \\ &= \frac{1}{Z} \int \mathcal{D}U\, M_F^{-1}(x,y)\, \det M_F\, e^{-S_G}. \end{aligned} \tag{1.14}$$

In a computer simulation, the lattice necessarily has a finite number of links; hence Equation (1.14) is a multi-dimensional but finite integral. It can be done using Monte Carlo integration with importance sampling:

- generate a gauge-field configuration $U^{(1)}$ (one random $SU(3)$ matrix for each link $U_\mu(x)$), with probability measure $\mathcal{D}U \det M_F\, e^{-S_G}$;
- repeat this process until one has an ensemble of N_{cfg} such configurations, $\left\{U^{(i)}, i = 1 \ldots N_{cfg}\right\}$;

- estimate the expectation value by

$$\left\langle 0 \left| \psi(x) \bar{\psi}(y) \right| 0 \right\rangle \simeq \frac{1}{N_{cfg}} \sum_{i=1}^{N_{cfg}} G\left(x, y; U^{(i)}\right), \tag{1.15}$$

  where $G(x, y; U^{(i)})$ means "the quark propagator between y and x, evaluated on the i'th gauge configuration".

Generating gauge configurations with the probability measure $\mathcal{D}U \det M_F \, e^{-S_G}$ is extremely difficult; at each stage in the generating algorithm one must re-evaluate the determinant of a matrix connecting all lattice fermion states (typically, $\mathcal{O}(8{,}000{,}000 \times 8{,}000{,}000)$). This can be done using various ingenious algorithms, but it can be avoided by setting $\det M_F = 1$. This defines the *quenched approximation* to lattice QCD. In the language of Feynman diagrams, this amounts to neglecting internal fermion loops. Configuration generation is then *much* faster.

As can be seen in Equation (1.14), calculating a quark propagator on a given gauge configuration entails inverting the fermion matrix M_F. This can be done by solving the linear equation

$$M_F(x, y) \, G(y, 0) = \eta(x, 0), \tag{1.16}$$

where $\eta(x, 0)$ is a suitable source function. $\eta(x, 0)$ is most often a delta function (actually a Kronecker delta on the lattice) but can be some non-local function used to produce a *smeared* propagator — see Chapter 3. $G(y, 0)$ is then the quark propagator from a fixed origin 0 to the lattice site y. Numerous algorithms are available for the solution of such sparse sets of linear equations — see reference [9] for a discussion.

Having obtained $G(y, 0)$ on each gauge configuration, hadron correlators can be constructed simply from products of these and the configuration average in Equation (1.15) performed. Thus, one is able to derive the hadron spectrum, via the lattice, from QCD.

1.4 The UKQCD Programme

In this section I shall outline the "dialect" of lattice QCD adopted by the UKQCD Collaboration for its light hadron spectrum calculations. I shall give a brief outline of the procedure we use to generate the ensemble of gauge configurations and describe the clover fermion action, an $\mathcal{O}(a)$-improved action used in the inversion of M_F.

1.4.1 Gauge configurations

The calculations of Chapters 4 and 5 were performed on an ensemble of 60 gauge configurations, calculated on a $24^3 \times 48$ lattice with a β value of 6.2.

The gauge configurations were generated using an $SU(2)$-subgroup heatbath algorithm [10] together with over-relaxation steps. In essence, each $SU(3)$ link is decomposed into three $SU(2)$ subgroups and these subgroups are updated according to the probability distribution e^{-S_G}.

The reason for this is that updating $SU(3)$ matrices in this fashion is difficult, but efficient algorithms exist for the $SU(2)$ case [11, 12]. In outline, the update step for each link of the lattice is

1. decompose the $SU(3)$ matrix into three $SU(2)$ subgroup matrices;
2. perform an over-relaxation update for each subgroup and reconstruct the $SU(3)$ link;
3. repeat steps 1 and 2 another four times, performing five over-relaxations in total; [1]
4. decompose the $SU(3)$ matrix and perform a single Cabibbo-Marinari heatbath update on each subgroup;
5. reconstruct the $SU(3)$ matrix and move on to the next one.

Details of the implementation of this algorithm can be found in references [9, 26].

The lattice was thermalised for 16,800 such combined sweeps before gauge configurations were sampled. We recorded subsequent configurations 2400 sweeps apart.

[1] The choice of five OR steps was based on test runs and an analysis of autocorrelation times between configurations; further information can be found in reference [26].

1.4.2 The clover action for quarks

As discussed in §(1.2), the various terms in the lattice action reduce to their continuum QCD forms in the limit $a \to 0$, but with correction terms proportional to some power of a. For the gluon action S_G, the corrections are $\mathcal{O}(a^2)$ but for S_{WF} there are terms of $\mathcal{O}(a)$. To reduce the effects of the finite lattice spacing, we use an *improved* action in which the $\mathcal{O}(a)$ effects are removed. This new action is termed the *Sheikholeslami-Wohlert* action or, for reasons that will become clear, the *clover* action.

The formation of the $\mathcal{O}(a)$-improved clover action, first discussed in reference [13], involves the addition of a term to the fermion action and a change of variables for the fermion fields. If we rotate the fermion fields as follows:

$$\begin{aligned} \psi &\to \psi' = \left(1 - \frac{r}{4}\left(\gamma \cdot \overrightarrow{D} - m\right)\right)\psi, \\ \bar{\psi} &\to \bar{\psi}' = \bar{\psi}\left(1 + \frac{r}{4}\left(\gamma \cdot \overleftarrow{D} + m\right)\right), \end{aligned} \tag{1.17}$$

and add the following term to the fermion action:

$$\Delta S = -ig\,\frac{r}{4}\sum_{x,\mu,\nu} \bar{\psi}(x) F^{\mu\nu} \sigma_{\mu\nu} \psi(x), \tag{1.18}$$

then the action

$$S_{CF} = S_{WF} + \Delta S \tag{1.19}$$

has no discretisation errors of $\mathcal{O}(a)$.

In Equation (1.18), $\sigma_{\mu\nu} = \frac{1}{2}[\gamma_\mu, \gamma_\nu]$ and

$$F^{\mu\nu} = \frac{1}{4}\sum_P \frac{1}{2gi}\left[U_\square^{(P)} - U_\square^{(P)\dagger}\right], \tag{1.20}$$

where the sum runs over the four plaquettes in the μ-ν plane centered on the site x, as shown in Figure 1.1. In both Equations 1.17 and 1.18, r is the Wilson parameter of Equation (1.6).

One of the major advantages of the clover action over other $\mathcal{O}(a)$-improved actions can clearly be seen if we write it in matrix form,

$$S_{CF} = \frac{1}{2\kappa}\,\bar{\psi}(x)\,M_{CF}(x,y)\,\psi(y). \tag{1.21}$$

where

$$M_{CF}(x,y) = L\,\delta(x,y) - \kappa \not{D}(x,y). \tag{1.22}$$

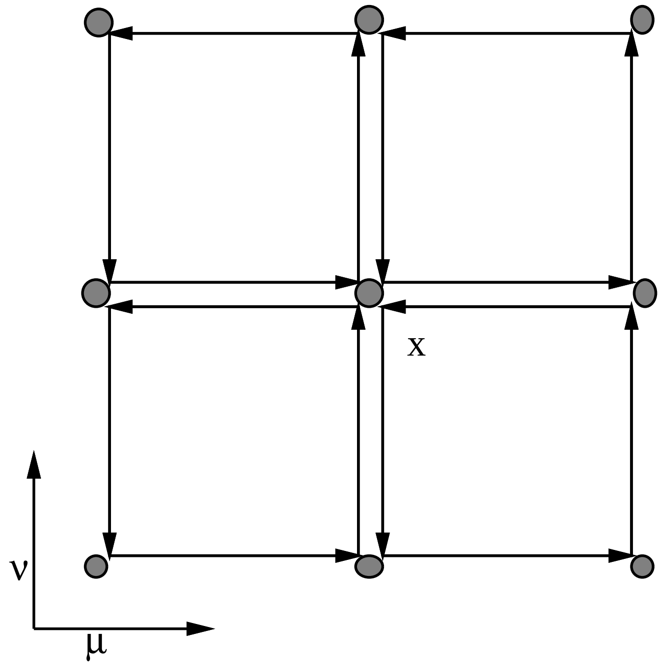

Figure 1.1: Diagram representing $F^{\mu\nu}$, as defined in Equation (1.20).

The first term L is purely local:-

$$L = 1 - \frac{ig\kappa}{2} F^{\mu\nu} \sigma_{\mu\nu},$$

and thus poses no major problems for an efficient implementation on a parallel computer.

1.4.3 UKQCD spectroscopy — a summary

In summary, then, the UKQCD light hadron spectrum programme, the results of which appear in later chapters, involves the following:

- a $24^3 \times 48$ lattice at gauge coupling $\beta = 6.2$;
- 60 gauge configurations, generated using the Wilson gauge action and an over-relaxation/Cabibbo-Marinari $SU(2)$ pseudo-heatbath algorithm;
- quark propagators calculated using an $\mathcal{O}(a)$-improved clover action, at a range of κ values corresponding to pseudoscalar mesons of masses 450 MeV and upwards;

- circa 100,000 lines of C and FORTRAN code on a range of hardware platforms, from workstations to the Grand Challenge Supercomputer Maxwell.

1.5 The Problems of Lattice QCD

Discretising QCD on the lattice causes several problems, each of which can lead to systematic errors in any results. I shall discuss the most important ones below, and outline possible solutions to alleviate the worst effects.

1.5.1 Finite lattice spacing — a case for improvement

As already discussed, the latticisation of QCD begets errors due to the imposition of the cutoff a^{-1}. Careful choice of the lattice action can reduce the size and importance of these errors; the clover action is one such choice. However, systematic improvement beyond $\mathcal{O}(a^2)$ is difficult, due to the increasing complexity of the requisite terms in the action. Studying the effects of these improved actions is an important programme for lattice studies.

1.5.2 Signals and statistics — a case for smearing

The evaluation of the path integral, Equation (1.15), is a statistical affair in the lattice model, requiring more and more configurations for increased accuracy. More configurations means more computer time which means more money. Methods to make the most of a given set of configurations are thus of significant importance. Since hadron spectroscopy involves extracting ground-state masses from an infinite sum of states, anything which facilitates this extraction is of benefit. Operator smearing (Chapter 3) is one technical trick to achieve this.

1.5.3 Quenching — a case for dynamical simulations?

Use of the quenched approximation means neglecting fermion loops in any diagrams concerning the process of interest. In the lattice model, quarks are never created or annihilated by interacting with the gauge fields — they propagate from source to sink through a background gluon field. The setting of $\det M_F = 1$ in the path integral is an *ad hoc* expedient, although some physical justification can be had from the *Zweig rule* [14] — strong processes in which the final states can only be reached by quark-antiquark annihilation are suppressed relative to other processes.

Without quenching, the generation of gauge configurations takes *much* longer but can be done. It is, however, a relatively new branch of the field and results to date have not been encouraging (see reference [17] for a review of current progress). Eventually, one would hope that all QCD simulations would include the effects of dynamical quarks in the gauge configurations, but it seems that a significant increase in computational power will be needed before this becomes viable.

1.5.4 Heavy quarks and small volumes — a case for bigger computers

As noted in §(1.4.3), our lightest quark mass corresponds to a pseudoscalar meson mass of 450 MeV, a long way away from the physical pion mass of 135–140 MeV. The simulation quark masses we use actually lie around the mass of the strange quark rather than the up or down quark. The problem lies in the conditioning of the fermion matrix M_F. As the quark mass $m \to 0$ (a good approximation to m_u and m_d), M_F becomes more singular and any given inversion algorithm will take progressively more and more iterations to calculate M_F^{-1}. Thus, direct simulation of the physical u and d quark regime is heavily restricted by the power of the available computer.

Similar hardware restrictions limit the size of the lattice in the simulation. The size of the computer lattice in turn restricts the physical region accessible to inspection. Fixing the gauge coupling β fixes the lattice spacing a and hence the physical size of the box. If the characteristic size of a hadron (measured in terms of its charge radius, r.m.s. wavefunction radius etc.) exceeds that of the box into which one is attempting to squeeze it, distortions will occur, leading to systematic errors in measurements of the hadron's properties.

These problems can only be alleviated by using bigger, faster machines; to some extent, the same can be said of *all* the problems of lattice QCD. Nevertheless, despite its difficulties, the lattice is the major tool with which we can hope to divine the non-perturbative behaviour of QCD. With continued work, and perhaps a quantum leap in computational power, we may yet remove the "almost-but-not-quite"...

Chapter 2

Hadron Spectroscopy on the Lattice

In this chapter I present an overview of the techniques involved in calculating masses and matrix elements from two-point hadronic correlators. I shall review the particular techniques used in the UKQCD hadron spectrum programme, as well as the more general details of the calculations involved.

In §(2.1) I discuss the importance of hadron-spectrum calculations in the context of general lattice QCD programmes. §(2.2) introduces the basic theory behind the computer calculations and in §(2.3) I define the hadron operators used in the calculations presented in later chapters. In §(2.4) I discuss the augmentations required to extract physical masses from a computer simulation and in §(2.5) I describe work I undertook in the development of a parallelised spectrum-calculation program for use on the Edinburgh Grand Challenge machine. Finally, in §(2.6) I present an overview of current lattice spectroscopy and indicate the status of present results.

2.1 A Fundamental Goal

It must surely be the case that if lattice QCD is to be at all useful as a tool for the study of the strong interactions of particle physics, it should, at the very least, be able to predict the masses of the lightest hadrons from first principles. This must be the most fundamental goal of the lattice theory. Physicists in other fields will have a hard time believing predictive calculations of, for instance, CKM matrix elements if our "simple" calculations of hadron masses are far from real-world values. In any series of lattice calculations the results of the hadron-spectrum programme must be viewed as vitally important.

2.2 Theoretical Considerations

The masses of light hadron states, and some simple matrix elements such as meson decay constants, are extracted from the large-time behaviour of the appropriate propagators

$$G_H(x,0) = \left\langle 0 \left| \phi(x)\phi^\dagger(0) \right| 0 \right\rangle , \tag{2.23}$$

for generic hadron operator $\phi(x)$.

In practice, the hadron propagator is always Wick-decomposed into products of quark and antiquark propagators; as a familiar example, consider the pseudoscalar meson. An appropriate hadronic operator to create a lattice pseudoscalar would be

$$P(x) = \bar{\psi}_u(x)\gamma^5\psi_d(x), \tag{2.24}$$

where $\bar{\psi}_u$ and ψ_d are lattice field operators for up and down quarks respectively, and γ^5 ensures the operator transforms with parity -1. We then have

$$\begin{aligned} P^\dagger(x) &= \left(\bar{\psi}_u(x)\gamma^5\psi_d(x)\right)^\dagger \\ &= \left(\psi_u^\dagger(x)\gamma_4\gamma^5\psi_d(x)\right)^\dagger \\ &= \psi_d^\dagger(x)\gamma^5\gamma_4\psi_u(x) \\ &= -\bar{\psi}_d(x)\gamma^5\psi_u(x) \end{aligned} \tag{2.25}$$

(we denote the Euclidean-time-like Dirac matrix by γ_4). Denoting spin indices by α, β, etc. and $SU(3)$ colour indices by i, j, etc. the pseudoscalar propagator would be

$$\begin{aligned} G_P(x,0) &= \left\langle 0 \left| P(x)\, P^\dagger(0) \right| 0 \right\rangle \\ &= \left\langle 0 \left| -\bar{\psi}^\alpha_{ui}(x)\, \gamma^5_{\alpha\beta}\, \psi^\beta_{di}(x)\, \bar{\psi}^\delta_{dj}(0)\, \gamma^5_{\delta\epsilon}\, \psi^\epsilon_{uj}(0) \right| 0 \right\rangle \\ &= -G'^{\beta\delta}_{ij}(x,0)\, \gamma^5_{\delta\epsilon}\, (-1) G^{\epsilon\alpha}_{ji}(0,x)\, \gamma^5_{\alpha\beta} \\ &= SpTr\, \left(G(x,0)\, \gamma^5\, G(0,x)\, \gamma^5\right) \\ &= SpTr\, \left(G(x,0)\, G^\dagger(x,0)\right), \end{aligned} \tag{2.26}$$

where $G(0,x) = \left\langle 0 \left| \psi_u(0)\bar{\psi}_u(x) \right| 0 \right\rangle = \left\langle 0 \left| \psi_d(0)\bar{\psi}_d(x) \right| 0 \right\rangle$ is the lattice quark propagator for u or d quarks and the trace is taken over spin and colour indices. I take $m_u = m_d$. In this way, the problem of calculating propagators for arbitrary hadron operators, Equation (2.23), becomes one of calculating simple quark propagators and then combining appropriate spin and colour components to yield an object with the correct hadronic quantum numbers.

In the Euclidean space of the lattice these two-point correlation functions decay exponentially with time with an exponent equal to the energy of the hadronic state in question. To extract the energy we Fourier transform the propagator over all spatial sites and examines the large-time limit of the resulting function. If $\vec{k}$ is the three-momentum of our generic hadron and $\{|n\rangle\}$ is some complete set of hadron states states with the right quantum numbers, we define

$$\begin{aligned}
C_H(t) &\equiv \sum_{\vec{x}} G_H(x,0) e^{i\vec{k}.\vec{x}} \\
&= \sum_{\vec{x}} \left\langle 0 \left| \phi(x)\ \phi^\dagger(0) \right| 0 \right\rangle e^{i\vec{k}.\vec{x}} \\
&= \sum_{\vec{x}} \left\langle 0 \left| e^{i\hat{p}\cdot x} \phi(0) e^{-i\hat{p}\cdot x} \phi^\dagger(0) \right| 0 \right\rangle e^{i\vec{k}\cdot\vec{x}} \\
&= \sum_{\vec{x}} \sum_n \int \frac{d^3 q_n}{(2\pi)^3} \frac{1}{2E_n(\vec{q}_n)} \left\langle 0 \left| e^{i\hat{p}\cdot x} \phi(0) e^{-i\hat{p}\cdot x} \right| n \right\rangle \left\langle n \left| \phi^\dagger(0) \right| 0 \right\rangle e^{i\vec{k}\cdot\vec{x}} \\
&= \sum_{\vec{x}} \sum_n \int \frac{d^3 q_n}{(2\pi)^3} \frac{1}{2E_n(\vec{q}_n)} e^{-iq_n\cdot x} e^{i\vec{k}\cdot\vec{x}} \left| \langle 0 \left| \phi(0) \right| n \rangle \right|^2 \\
&= \sum_n \int \frac{d^3 q_n}{(2\pi)^3} A_n e^{-E_n(\vec{q}_n)t} \frac{1}{2E_n(\vec{q}_n)} \sum_{\vec{x}} e^{-i(\vec{q}_n - \vec{k})\cdot\vec{x}} \\
&= \sum_n \int \frac{d^3 q_n}{(2\pi)^3} A_n e^{-E_n(\vec{q}_n)t} \frac{1}{2E_n(\vec{q}_n)} (2\pi)^3 \delta^3(\vec{q}_n - \vec{k}) \\
&= \sum_n \frac{A_n}{2E_n(\vec{k})} e^{-E_n(\vec{k})\ t} \qquad (2.27)
\end{aligned}$$

where $A_n \equiv \left| \langle 0 \left| \phi(0) \right| n \rangle \right|^2$ and $E_n(\vec{k})$ is the energy of the hadron state $|n\rangle$ with momentum $\vec{k}$. If we take the large-t limit of this expression, the state of lowest energy dominates the sum. In addition, restricting ourselves to states with zero three-momentum so that $E_n(\vec{0}) = m_n$, we arrive at the key formula for hadron spectroscopy on the lattice:

$$\lim_{t\to\infty} C_H(t) = \frac{A_1}{2m_1} e^{-m_1 t}. \qquad (2.28)$$

I use the subscript 1 to denote the lightest hadron state with the quantum numbers of the operator ϕ. For example, if ϕ had spin 0 and parity -1, the state $|1\rangle$ would be the pion.

For hadrons at rest the Fourier transform in Equation (2.27) becomes a simple sum over spatial sites and the resulting object $C_H(t)$ is known as a *timesliced* propagator. Examination of Equations (2.26) and (2.27) shows that we can build a timesliced hadron propagator from timesliced quark propagators, i.e. we can do calculations for any and all hadrons timeslice by timeslice.

A useful tool in diagnosing the point in time at which all the higher-mass states have decayed away is the *effective mass* function:

$$m_{eff}(t) \equiv \log\left(\frac{C_H(t)}{C_H(t+1)}\right). \tag{2.29}$$

As $t \to \infty$ this function levels out into a plateau at m_1, enabling one to identify the ground state. The effective mass can be used as sole determination of the ground state, though in practice it is usual to use it only to identify the time-region in which the ground state dominates. The hadron mass is then extracted by fitting the timesliced propagator to an exponential function $A\,e^{-mt}$ over this range.

2.3 Definitions of Hadronic Operators

In Equation (2.24) I defined one possible pseudoscalar meson operator in terms of its constituent quark fields. In this section I shall define operators for creating other hadron states and indicate how they are calculated on the lattice by means of their Wick decompositions.

2.3.1 Meson operators

In the quark model mesons are defined as quark-antiquark pairs. On the lattice a generic meson operator is

$$\phi_M(x) \equiv \bar{\psi}(x)\;\Gamma\;\psi(x), \tag{2.30}$$

where Γ is one of the 16 independent Dirac matrices $1, \gamma^5, \gamma_\mu, \gamma_\mu\gamma^5, \sigma_{\mu\nu}$. The Wick decompositions for mesons follow the same pattern as in Equation (2.26). If we denote the meson operators by their γ matrix content a and b then, in general,

$$\begin{aligned} G_{\phi_a\phi_b}(x,0) &= \left\langle 0 \left| \phi_a(x)\ \phi^{\dagger}{}_b(0) \right| 0 \right\rangle \\ &= \left\langle 0 \left| \bar{\psi}(x)\Gamma_a\psi(x) \left(\bar{\psi}(0)\Gamma_b\psi(0)\right)^{\dagger} \right| 0 \right\rangle \\ &= \left\langle 0 \left| \bar{\psi}(x)\Gamma_a\psi(x)\bar{\psi}(0)\Gamma_b^{\dagger}\psi(0) \right| 0 \right\rangle \\ &= SpTr\left(-G(x,0)\Gamma_a G(0,x)\Gamma_b^{\dagger}\right). \end{aligned} \tag{2.31}$$

We use the following assignments for the meson channels of interest:

Pseudoscalar: Operator $P \equiv \bar{\psi}\ \gamma^5\ \psi$, $J^{PC} = 0^{-+}$.
The lightest state is the pion; we can also extract the K-meson provided we identify the mass of the strange quark on the lattice.

Vector: Operator $V \equiv \sum_{i=1}^{3} \bar{\psi}\ \gamma_i\ \psi$, $J^{PC} = 1^{--}$.
For the lightest state, each γ_i gives us one polarisation state of the ρ-meson. The sum over polarisation states gives us the "total" ρ. We can also extract K^* and ϕ mesons using the strange quark mass.

Axial Vector: Operator $A_\mu \equiv \bar{\psi}\ \gamma_\mu\gamma^5\ \psi$.
The fourth component, A_4 ($J^{PC} = 0^{-+}$), can be used to create a pseudoscalar meson. Usually, we use A_4 in conjunction with the pseudoscalar density P in the calculation of the pseudoscalar decay constant f_P.

The sum over the first three components of A_μ, $A \equiv \sum_{i=1}^{3} A_i$, projects onto the state with $J^{PC} = 1^{+-}$; the lightest particle with these quantum numbers is the $b_1(1235)$ meson, though in practice the signal is hard to extract. For states with non-zero 3-momentum p_i, this combination also has a projection onto $p_i\ \bar{\psi}\gamma^5\psi$, the pseudoscalar state.

Scalar: Operator $S \equiv \bar{\psi}\ \psi$, $J^{PC} = 0^{++}$.
The signal from this operator is poor; we would expect the lightest state to correspond to the $a_0(980)$ or the $f_0(975)$.

Tensor: Operator $T_{\mu\nu} \equiv \bar{\psi}\ \sigma_{\mu\nu}\ \psi$.
The combination $\sum_{i,j=1}^{3} T_{ij}$ projects onto the $J^{PC} = 1^{--}$ vector meson state, though with a poorer signal than the V operator.

The operator $T \equiv \sum_{i=1}^{3} T_{i0}$ has $J^{PC} = 1^{++}$; the lightest corresponding state is the $a_1(1260)$, though again, the signal is poor.

2.3.2 Baryon operators

The definitions of lattice baryon operators are a little more involved. Baryons are composed of three quarks of different $SU(3)$ colour. A generic baryon operator looks like

$$\phi_B(x) \equiv \epsilon_{ijk} \left(\psi_1^i(x)\ C\ \Gamma\ \psi_2^j(x)\right) \psi_3^k(x) \tag{2.32}$$

for quark flavours $1, 2, 3$ and colours i, j, k. Γ is again an appropriate Dirac matrix and C is the charge conjugation matrix. For calculations we choose operators that create states in the $J = \frac{1}{2}$ $SU(3)$-flavour octet and the $J = \frac{3}{2}$ decuplet.

Nucleon: $I(J) = \frac{1}{2}(\frac{1}{2})$. Operator $N_\alpha \equiv \epsilon_{ijk} \left(u^i C\gamma^5 d^j\right) u_\alpha^k$.
Creates both $\frac{1}{2}^+$ and $\frac{1}{2}^-$ states; the lightest $\frac{1}{2}^+$ state is the nucleon. The created state is a Dirac spinor, the index carried by the un-contracted u_α^k.

Wick decomposition:

$$\begin{aligned}
G_N(x,0) &= \left\langle 0 \left| N_\epsilon(x)\overline{N_\zeta}(0) \right| 0 \right\rangle \\
&= \left\langle 0 \left| \epsilon_{ijk}\epsilon_{lmn} \left(u^i(x) C\gamma^5 d^j(x)\right) u_\epsilon^k(x) \left[\overline{\left(u^l(0) C\gamma^5 d^m(0)\right) u_\zeta^n(0)}\right] \right| 0 \right\rangle \\
&= \left\langle 0 \left| -\epsilon_{ijk}\epsilon_{lmn} u^i(x) C\gamma^5 d^j(x) u_\epsilon^k(x) \bar{u}_\zeta^l(0) \bar{d}^m(0) \overline{C\gamma^5} \bar{u}^n(0) \right| 0 \right\rangle \\
&= \epsilon_{ijk}\epsilon_{lmn} (C\gamma^5)^{\alpha\beta} (\overline{C\gamma^5})^{\gamma\delta} \times \\
&\qquad \left(G_{\alpha\zeta}^{il}(x,0) G_{\epsilon\gamma}^{kn}(x,0) - G_{\alpha\gamma}^{in}(x,0) G_{\epsilon\zeta}^{kl}(x,0)\right) G_{\beta\delta}^{jm}(x,0).
\end{aligned} \tag{2.33}$$

The bar over a quantity, $\overline{N}$, is the usual Dirac notation for $N^\dagger\gamma_4$. In addition, to extract the $\frac{1}{2}^+$ nucleon we average the $(\epsilon\zeta) = (11)$ and (22) components. The (33) and (44) components yield the $\frac{1}{2}^-$ state, the lightest of which is the $N(1535)$. In practice it is difficult to calculate this mass due to the poor nature of the signal.

Delta: $I(J) = \frac{3}{2}(\frac{3}{2})$. Operator $\Delta_{\mu,\alpha} \equiv \epsilon_{ijk} \left(u^i C\gamma_\mu u^j\right) u^k_\alpha$.
This operator has both a Lorentz and a Dirac index and creates states in the $1 \otimes \frac{1}{2} \sim \frac{3}{2} \oplus \frac{1}{2}$ representation. To extract the lightest state, the lattice version of the $\Delta(1232)$, we must average over the three Lorentz polarisations and project out the spin-$\frac{3}{2}$ component.

Wick decomposition:

$$\begin{aligned}
G_\Delta(x,0) &= \left\langle 0 \left| \Delta_\epsilon(x)\overline{\Delta_\zeta}(0) \right| 0 \right\rangle \\
&= \left\langle 0 \left| \epsilon_{ijk}\epsilon_{lmn} \left(u^i(x)C\gamma_\mu u^j(x)\right) u^k_\epsilon(x) \left[\overline{\left(u^l(0)C\gamma_\mu u^m(0)\right) u^n_\zeta(0)}\right] \right| 0 \right\rangle \\
&= \left\langle 0 \left| -\epsilon_{ijk}\epsilon_{lmn} u^i(x)C\gamma_\mu u^j(x)u^k_\epsilon(x)\bar{u}^l_\zeta(0)\bar{u}^m(0)\overline{C\gamma_\mu}\bar{u}^n(0) \right| 0 \right\rangle \\
&= \epsilon_{ijk}\epsilon_{lmn}(C\gamma_\mu)^{\alpha\beta}(\overline{C\gamma_\mu})^{\gamma\delta} \times \\
&\qquad \left(4\, G^{il}_{\alpha\zeta}(x,0)G^{kn}_{\epsilon\gamma}(x,0) - 2\, G^{in}_{\alpha\gamma}(x,0)G^{kl}_{\epsilon\zeta}(x,0)\right) G^{jm}_{\beta\delta}(x,0).
\end{aligned} \tag{2.34}$$

Again we average over the spinor combinations $(\epsilon\zeta) = (11)$ and (22). The fourth Lorentz component, Δ_4, is pure spin-$\frac{1}{2}$ and can be used to project out the desired pure spin-$\frac{3}{2}$ state: $\Delta(\frac{3}{2}) = \Delta_1 + \Delta_2 + \Delta_3 - \Delta_4/3$. Since the $\Delta(\frac{3}{2})$ operator is fully flavour-symmetric, evaluating the mass of the created state at the strange-quark mass will give us the (sss) state, the Ω.

All these various hadron operators are summarised in Table 2.1.

2.4 Computational Refinements

The implementation of the mathematics of the previous sections in an actual computer calculation requires some further thought. Ideally, we would want to

- calculate our quark propagators for up, down, strange, etc., quarks;
- combine the right quark propagators to make hadrons of interest;
- fit the timesliced hadron correlators to $A\, e^{-mt}$ and write down the hadron mass in MeV.

For several reasons, some outlined in Chapter 1, things are not as simple as this.

Meson Operators			
Channel	J^{PC}	Operator	Lightest state
P	0^{-+}	$\bar{\psi}\gamma^5\psi$	pion
V	1^{--}	$\sum_{i=1}^{3}\bar{\psi}\gamma_i\psi$	$\rho(770)$
A_4	0^{-+}	$\bar{\psi}\gamma_4\gamma^5\psi$	pion
A	1^{+-}	$\sum_{i=1}^{3}\bar{\psi}\gamma_i\gamma^5\psi$	$b_1(1235)$
S	0^{++}	$\bar{\psi}\psi$	$a_0(980),\ f_0(975)$
T	1^{++}	$\sum_{i=1}^{3}\bar{\psi}\sigma_{i0}\psi$	$a_1(1260)$

Baryon Operators			
Channel	$I(J^P)$	Operator	Lightest state
N	$\frac{1}{2}(\frac{1}{2}^+)$	$\frac{1}{2}(1+\gamma_4)\,\epsilon_{ijk}(u^iC\gamma^5d^j)u^k_\alpha$	nucleon(940)
$\tilde{N}$	$\frac{1}{2}(\frac{1}{2}^-)$	$\frac{1}{2}(1-\gamma_4)\,\epsilon_{ijk}(u^iC\gamma^5d^j)u^k_\alpha$	$N(1535)$
$\Delta(\frac{3}{2})$	$\frac{3}{2}(\frac{3}{2}^+)$	$\frac{1}{2}(1+\gamma_4)\,\epsilon_{ijk}(u^iC\gamma_iu^j)u^k_\alpha$	$\Delta(1232)$
$\tilde{\Delta}(\frac{3}{2})$	$\frac{3}{2}(\frac{3}{2}^-)$	$\frac{1}{2}(1-\gamma_4)\,\epsilon_{ijk}(u^iC\gamma_iu^j)u^k_\alpha$	$\Delta(1700)$
$\Delta(\frac{1}{2})$	$\frac{3}{2}(\frac{1}{2}^+)$	$\frac{1}{2}(1+\gamma_4)\,\epsilon_{ijk}(u^iC\gamma_4u^j)u^k_\alpha$	$\Delta(1550)$
$\tilde{\Delta}(\frac{1}{2})$	$\frac{3}{2}(\frac{1}{2}^-)$	$\frac{1}{2}(1-\gamma_4)\,\epsilon_{ijk}(u^iC\gamma_4u^j)u^k_\alpha$	$\Delta(1620)$

Table 2.1: Summary of operators used in the calculation of hadron propagators

2.4.1 Approximating the limit $t \to \infty$

An obvious first problem is that, for want of an infinite-memory computer, the limit $t \to \infty$ in Equation (2.28) cannot, in practice, be taken. Instead one can only make t as large as possible and hope that one's hadron signal is not swamped by statistical noise before the higher-mass states have died away. A typical "good" temporal size for current lattice simulations is $T = 48$; the results I present in Chapters 4 and 5 were obtained on a lattice of this size. A further subtlety is that the maximum *propagation* time for the hadron is only $T/2$ due to the imposition on the lattice of periodic boundary conditions in time. Because of this the hadron propagates both forwards and backwards in time from its creation point and conventionally one averages the signals from the two temporal halves of the lattice. Consequently, for mesons the fit-function used to extract the mass becomes

$$A(e^{-mt} + e^{-m(T-t)}). \tag{2.35}$$

For baryons, the operators in Table 2.1 create forward-moving baryon states but backward-moving parity partner states. Consequently, we cannot perform a simple average of the baryon signal and we must combine signals from the two different parity channels in a fit over half the lattice:

$$Ae^{-mt}, \qquad t < L_t/2. \tag{2.36}$$

2.4.2 Making contact with the "real world"

Another feature of computer calculations is that the masses extracted from Equation (2.35) are pure numbers, not dimensional masses. We cannot extract physical masses directly for two reasons:

1. we cannot simulate quarks with the correct masses to correspond to up and down flavours;

2. the lattice model has no intrinsic physical scale.

The action of lattice QCD has two free parameters — the bare gauge coupling g_0 and the bare quark mass m (alternatively we may think of the gauge coupling as defining the physical length of the lattice spacing a). In simulations we choose numerical values for g_0 and m, constrained in large part by the size of the computer available. In order to make contact between the computer simulation and the "real world" we require two inputs to the theory — something to enable us to extract results at physical quark masses and something to define the lattice scale.

To resolve the first question we make use of the *partially conserved axial current hypothesis* (PCAC) [15], which implies that

$$m_P^2 \propto m \tag{2.37}$$

where m_P is the mass of the lattice pseudoscalar meson, the generic pion. In the real world the pion is the pseudo-Goldstone boson resulting from the spontaneous and explicit breaking of the chiral $SU(2)_L \times SU(2)_R$ symmetry of the QCD Lagrangian. Its mass is small, corresponding to the small symmetry-breaking term proportional to the up- and down-quark masses. We define our physical regime to be the chiral regime in which $SU(2)_L \times SU(2)_R$ symmetry is restored and $m = m_u = m_d \to 0$. Since on the lattice the quark mass is written in terms of the hopping parameter κ (Equation (1.10)), this involves using the data for m_P^2 to establish the point, κ_{crit}, at which $m = 0$.

To set the lattice scale one simply fixes a given calculated quantity, a hadron mass m_H for instance, to its physical value:

$$a^{-1} = m_H^{phys}/m_H \quad \text{MeV}. \tag{2.38}$$

Using this relation, all other lattice quantities can be converted into physical units for comparison with experiment. Typical candidates for scale-setting quantities include the vector-meson mass m_V, the pseudoscalar decay constant f_P and the purely gluonic quantity $\sqrt{K}$, the string tension (see, for example, reference [26]). Ideally, one would hope to obtain the same scale whatever the chosen quantity. This desirable state, known as *scaling*, indicates that the lattice simulation is close to the $a \to 0$ continuum limit and engenders confidence in the accuracy of the lattice calculations.

2.4.3 A prescription for spectrum calculations

The general prescription for our spectrum calculations is then as follows:

1. calculate hadron propagators at a number of different κ values;
2. fit the timesliced propagators to a suitable exponential function of time, taking boundary effects into account;
3. extrapolate data for $m_P^2 \rightarrow 0$ to identify κ_{crit} and the chiral regime;
4. establish the lattice scale using some suitable quantity;
5. extrapolate the mass data in κ to κ_{crit} and multiply by the scale a^{-1} to obtain lattice predictions for physical masses.

2.5 Development of Parallelised Spectrum Codes

In this penultimate section I shall outline the work that went into the development of a program to perform step 1 in the prescription of §(2.4.3), namely the actual calculations of hadron correlators from quark propagators. This program was designed to be the main spectrum-calculation platform for the UKQCD collaboration and to run on the Grand Challenge Machine at Edinburgh.

The Grand Challenge Machine, Maxwell, is a massively parallel supercomputer built by the British company Meiko Ltd. It is based on 64 Intel i860 processors, each with 16Mbytes of memory, connected together through 128 T800 transputers. The connectivity is such that different processor topologies can be set up as required for different simulations. Further details of Maxwell can be found in references [9, 16].

The main technicalities for the design of a spectroscopy program derive from the distribution of the QCD lattice over the processor grid. For instance, distributing one timeslice of a $24^3 \times 48$ lattice over 16 processors means that each processor "knows of" only a sublattice one sixteenth the size of the full lattice. This has connotations for any operation requiring communication between lattice sites (e.g.

Jacobi smearing) or knowledge of a site's position in the full lattice (e.g. finite momentum phase factors $e^{i\vec{k}\cdot\vec{x}}$).

The design and development of this multiprocessor spectrum code were done in conjunction with Craig McNeile, Alan Simpson and David Richards as part of UKQCD. The program grew from older Cray/D.A.P. codes written by David Richards and Ken Bowler. The fine details of processor communication for this and other Maxwell projects were masterfully handled by Stephen Booth. The finished product comprises 22,600 lines of both C and FORTRAN.

2.5.1 Overview

A pseudocode overview of the spectrum program is shown in Table 2.2. I use the notation h and l to refer to timesliced quark propagators corresponding to one of four heavy-quark masses and one of three light-quark masses respectively. Notation for smeared (non-local) propagators is of the form ($\langle$sink$\rangle\langle$source$\rangle$) where S denotes an operator smeared using the Jacobi algorithm of Chapter 3 and L denotes a local (single-site) operator.

The main requirements for the design of the code were

- the ability to handle multiple quark propagators and combine propagators of different quark mass to produce non-degenerate hadrons;
- the implementation of correlator calculations at non-zero momentum;
- the ability to smear propagators at the sink "online".

In Table 2.2, steps 1–4 involve the definition of various parameters for the current run — number of propagators, size of lattice, smearing parameters etc. Step 2 is concerned with defining the spatial neighbours for each site on the processor sublattice, including neighbours on adjacent processors. These *neighbour tables* are used later in the Jacobi smearing step (13). Step 4 defines a table of phase factors $e^{i\vec{k}\cdot\vec{x}}$ over the global lattice.

The calculations are performed timeslice by timeslice; the whole process lives inside a loop over t. Step 6 reads in a timeslice of the appropriate gauge field, if

```
SET UP SIMULATION PARAMETERS;
SET UP 3-D NEIGHBOUR TABLES;
SET UP $\gamma$-MATRICES FOR ALL DESIRED CORRELATOR CHANNELS;
SET UP TABLE OF PHASE FACTORS FOR $\vec{p} \neq \vec{0}$;
BEGIN LOOP $t$ OVER TIMESLICE;
   READ IN GAUGE-FIELD TIMESLICE NEEDED FOR JACOBI SMEARING;
   BEGIN LOOP PROP OVER $h^{(LS)}$ AND $l$ PROPAGATORS;
      READ IN PROPAGATOR IN I860 FORMAT FOR TIMESLICE $t$;
      REORDER I860 PROPAGATOR TO VECTOR FORMAT AND STORE;
      COMPUTE DEGENERATE HADRON CORRELATORS USING VECTOR
      PROPAGATOR PROP;
      SAVE HADRON CORRELATORS FOR TIMESLICE $t$;
      IF PROP CORRESPONDS TO $h^{(LS)}$ THEN
         SMEAR I860 PROPAGATOR AT SINK;
         REORDER SMEARED I860 PROPAGATOR TO VECTOR FORMAT
         AND STORE AS $h^{(SS)}$;
         COMPUTE DEGENERATE HADRON CORRELATORS USING $h^{(SS)}$
         PROPAGATOR;
         SAVE $(SS)$ HADRON CORRELATORS FOR TIMESLICE $t$;
   END LOOP PROP;
   BEGIN LOOP PROP1 OVER $h^{(LS)}$, $l$ AND NEW $h^{(SS)}$ PROPAGATORS;
      BEGIN LOOP PROP2 OVER $l$ PROPAGATORS ONLY;
         IF ($prop1 = h$ AND $prop2 = l$) OR ($prop1 = l$ AND $prop2 = l$)
         THEN
            COMPUTE NON-DEGENERATE HADRON CORRELATORS USING
            THE TWO PROPAGATORS PROP1 AND PROP2;
            SAVE NON-DEGENERATE HADRON CORRELATORS FOR
            TIMESLICE $t$;
      END LOOP PROP2;
   END LOOP PROP1;
END LOOP $t$;
```

Table 2.2: Pseudocode outline of design for multiprocessor spectrum code. The notation is such that h refers to a heavy-quark propagator and l to a light-quark propagator. (LS) indicates a source-smeared propagator and (SS) a propagator smeared at sink and source.

Jacobi smearing is required later and step 7 begins the loop over heavy (source-smeared) and light (local) propagators. These have been calculated previously and pre-loaded onto disk.

One point here is that the quark propagators are calculated and stored in a certain component order which differs (for technical and historical reasons) from the order required by the hadron correlator code. Steps 8 and 9 read in the propagator and then reorder it into the appropriate form.

Step 10 performs the actual "tying up" of quark propagators with appropriate γ-matrices and projections to yield hadron correlators. Here we use only a single quark propagator, giving us degenerate hadrons. Step 11 writes out the computed hadrons for timeslice t; in all the program will produce 48 files, each of length $\sim$16.5 kbytes. Thus the spectrum code reduces one (or two) quark propagators of size $\sim$730 Mbytes each to a set of hadron correlators of $\sim$800 kbytes — a factor of 900 reduction.

Steps 12–16 note whether the current propagator is of the heavy-smeared-source type and, if so, smear it at the sink and compute a set of heavy-quark smeared-smeared correlators.

Steps 18–24 perform two loops, one over all quark propagators — the read-in $h^{(LS)}$ and l and the newly-computed $h^{(SS)}$ — the other over the l only. For certain combinations, steps 21–22 compute and save correlators using the non-degenerate propagators.

In the following subsections I shall present short descriptions of some of the technically more interesting areas of the spectrum code that I worked on.

2.5.2 Code conventions

In all the UKQCD code written on Maxwell and elsewhere, the lattice sites are parametrised by two numbers — a *parity* and a *label*. The parity of each site is alternately "even" and "odd" such that the lattice looks like a (multi-dimensional) chessboard. The label labels all sites of the same parity in some unique way. This "red-black" partition of the lattice adds some technicalities to code development but is vital in preconditioning fermion-matrix inversion routines for optimal performance (see [9] and references therein).

Quark fields are stored as arrays of complex numbers indexed by colour, spin, site label and parity. A quark propagator, being the partial contraction of two quark fields, one of which lives at a fixed origin, is a complex array indexed by source colour, source spin, site label, parity, sink colour and sink spin.

2.5.3 3-d neighbour tables

For operations that require information exchange between lattice sites, we must have some way of "telling" each site where to find its neighbours. When the lattice is distributed over a processor array as a set of sublattices, the neighbours of some sites will live on different processors. A set of *neighbour tables* is needed to record the location of each site's neighbours in each direction, and how to access those neighbours if they lie on another processor.

Neighbour tables in four-dimensional spacetime are used in the inversion of the fermion matrix (see, for example, reference [9]). For the smearing algorithm presented in Chapter 3 we also require a set of four *three*-dimensional neighbour tables. Two of these tables — "up" and "down", indexed by direction — give the label of the site in the positive (up) or negative (down) directions respectively. The definition is such that, for example, up[μ][parity][label] holds the label of the site adjacent to site (label, parity) in the positive μ direction (the parity of this neighbour is, by construction, opposite to that of the site). Here μ runs from 1–3, the number of spatial directions.

The other two tables, "upper" and "lower", also with a direction index, describe the layout of the upper and lower boundaries. These tables are used for inter-processor communication. If we look at a two-dimensional example of a small 4×4 lattice, Table 2.3 shows the labelling of the lattice and upper and lower boundary tables. Table 2.4 indicates the layout of the up and down neighbour tables for this lattice. In Table 2.4 some of the up/down entries refer to *ts*, the index of the start of the *tail*. The tail is the object used to pass information between processors; its layout is described by the appropriate boundary table, lower or upper, depending on which way communication is proceeding. The label

6_o	6_e	7_o	7_e

$\uparrow$

upper[1]

6_o
4_e
2_o
0_e

$\leftarrow$ lower[0]

6_o	6_e	7_o	7_e
4_e	4_o	5_e	5_o
2_o	2_e	3_o	3_e
0_e	0_o	1_e	1_o

upper[0] $\rightarrow$

7_e
5_o
3_e
1_o

lower[1]

$\downarrow$

0_e	0_o	1_e	1_o

Table 2.3: Illustration of lattice labelling and upper/lower boundary neighbour tables for a two-dimensional 4×4 lattice. Directions are labelled as 0 (left-right) and 1 (up-down).

up[0]

6	7	7	*ts*+1
4	5	5	*ts*+1
2	3	3	*ts*
0	1	1	*ts*

up[1]

ts	*ts*	*ts*+1	*ts*+1
6	6	7	7
4	4	5	5
2	2	3	3

down[0]

ts+1	6	6	7
ts+1	4	4	5
ts	2	2	3
ts	0	0	1

down[1]

4	4	5	5
2	2	3	3
0	0	1	1
ts	*ts*	*ts*+1	*ts*+1

Table 2.4: Up and down neighbour tables for the 4×4 lattice of Table 2.3. *ts* refers to the index of the start of the tail — see the text.

ts is defined to be one bigger than the maximum label required to index the parity half-lattice; in our example, *ts* would be 8. Thus, any time a neighbour table points to a site that is greater than the maximum site on the local lattice we know to look for the appropriate datum in the tail which will contain information passed from a neighbouring processor.

As an example of how this works, the Jacobi smearing code requires the multiplication

$$U_\mu(x) \times \psi(x + \mu).$$

Referring to Table 2.3, consider the $\mu = \hat{0}$ case. When $x = 1_o, 3_e, 5_o$ or 7_e the $(x + \hat{0})$'th element of the vector ψ is off the right hand edge of our 4×4 sublattice; it lies, in fact, in the *lower boundary* of the neighbouring sublattice. Thus we would fill our local tail with the elements of ψ dictated by the labels in the lower boundary table and call the communications routines. Our tail would be passed onto the processor "to the left" and we would receive a tail with the elements of ψ from the lower boundary of our neighbour "on the right".

Thus, for the on-line Jacobi smearing all the necessary information concerning the topology of the spatial lattice layout is defined in the neighbour tables. Once set up, any communication between lattice sites is achieved through these.

2.5.4 Phase factors for $\vec{k} \neq \vec{0}$

If we look again at Equation (2.27) we see that to obtain the propagator of a hadron with non-zero three-momentum $\vec{k}$ we must introduce a factor of $e^{i\vec{k}\cdot\vec{x}}$ into the calculation. Since the lattice is finite in extent, with periodic boundary conditions, the smallest unit of momentum in any direction is

$$p_i \equiv \frac{2\,\pi}{L_i}, \qquad (i = 1 \ldots 3).$$

L_i is the extent of the lattice in the i'th direction. Using these basic units we define a table of phase factors over the whole lattice by

$$e^{i n_i\, p_i\, x_i}, \quad n_i \in \mathbb{N}$$

for coordinate x_i. The tricky part lies in the fact that the x_i must be position coordinates *in the global lattice*, not the sublattice that the processor "knows" about.

Thus, defining this table of phase factors involves interrogating the processor grid to determine the absolute values of coordinates on each processor. This, as with all other communication routines on Maxwell, is done via the CSTools harness — see [16] for further details.

2.5.5 Propagator formats and reordering

In the spectrum code, timesliced quark propagators are stored in two different formats, one labelled "i860" and one "vector". The reasons for this are largely technical: for ease of development the Maxwell code was built up from existing FORTRAN routines which performed the actual correlator calculations. These codes were designed originally to run on vector computers which demanded a very particular layout of the propagators. This layout is somewhat different to the optimal layout on Maxwell; hence the code which generates the quark propagators produces them in a different form to that required by our correlator routines. Consequently, it was necessary to build into the code "filters" to reorder propagators from one format to the other, a somewhat technical exercise in 'C' pointer swapping...

2.6 The State of the Art

In this last section I wish to present a prècis of the current state of quenched light hadron spectrum calculations in lattice QCD and indicate the approximate whereabouts on the world stage of the results presented here in later chapters. A good review of current calculations, in both quenched and full QCD, is to be found in reference [17].

2.6.1 Quenched Wilson calculations

A number of collaborations are currently involved in detailed calculations of the hadron spectrum in the quenched approximation using Wilson-formulation fermions. The most notable of these include the GF11 group in the U.S., QCDPAX and QCD_TARO in Japan and APE and UKQCD in Europe.

The current results of the GF11 group [18] may arguably provide a yardstick for present simulations. They have calculated a number of hadron masses on a range of lattices of different sizes and β values using Gaussian smeared operators. With relatively high statistics ($N_{cfg} \sim \mathcal{O}(200)$ for most of their lattices) they have been able to extrapolate fitted masses to an infinite-volume, zero-lattice-spacing limit. Their results for most quantities — m_{K^*}, m_N, m_Δ etc. — show agreement with experimental data to within their statistical errors of 1–5%.

Of the Japanese groups, QCD_TARO [19] have studied finite size effects at $\beta = 6.3$ for lattices of spatial size $L_s = 16$, 24 and 32. For mesons, they find no significant effect in masses due to the finite size of the lattice; for baryons they see higher masses on the smaller lattices, though the differences are less than one standard deviation from $L_s = 24 \to 32$. Their work suggests that effects due to the spatial size of the lattice for this coupling are negligible for the lightest mesons and baryons for $L_s \gtrsim 24$.

QCDPAX [20] have performed a study of excited-state contamination of light hadron ground states on a large-L_t lattice at couplings $\beta = 5.85$ and 6.0. Analysing 100 configurations (200 for $\beta = 6.0$) they demonstrated that extraction of a reliable ground-state signal for light mesons (ρ-meson, nucleon e.g.) may entail going to much later lattice times than was previously thought necessary (cf. Equation (2.28)). They note that fitting in this later "true plateau" region reduces mass estimates by $\sim$3–7%.

Their results suggest that, for meson signals, the *minimum* times from which to extract the ground state are $t \sim 11$ for $\beta = 5.85$ and $t \sim 15$ for $\beta = 6.0$. For baryons, the situation is worse; they postulate minima for the nucleon of $t \sim 15$ at $\beta = 5.85$ and $t \sim 19$ at $\beta = 6.0$. They suggest a "rule of thumb" to the effect that the earliest timeslice of the ground-state signal between lattices at different β's seems to scale approximately as the ratio of the lattice scales. Following this argument, at $\beta = 6.2$ one might expect to find the true ground states of mesons beginning at $t \sim 19$ and baryons at $t \sim 24$. Their work is an important step forward in quantifying systematic errors in procedures used to extract hadron masses.

The APE-100 computer [21], a custom-built dedicated QCD engine based in Rome, is a candidate for "current best QCD machine". In reference [22] the

APE Collaboration present results at $\beta = 6.3$ for 128 configurations of a $24^3 \times 32$ lattice. They find difficulty in extracting ground state signals, concluding that the time extent of $L_t = 32$ is insufficient at this β value. Consequently, their mass estimates lie above experimental values, in some cases by several standard deviations. Additional APE spectrum calculations can be found in reference [24], in which they compare results from the standard Wilson action with the $\mathcal{O}(a)$-improved clover. Their statistical errors on mesonic quantities are of $\mathcal{O}(4\%)$.

The earlier results from the UKQCD Collaboration can be found in references [25, 26] which again compare the hadron mass spectra for the Wilson and clover actions. The current UKQCD spectrum results provide the backbone of Chapter 4 of this work and can also be found in [27]. These results use the clover action exclusively and cover a range of light and strange mesons and baryons; statistical errors are of $\mathcal{O}(10\%)$ for baryons, $\mathcal{O}(5\%)$ for mesons and $\mathcal{O}(3\%)$ for meson decay constants. The full splendour of these results can be found in Chapter 4.

2.6.2 Quenched staggered calculations

There are also several collaborations working in the quenched approximation using *staggered* or *Kogut-Susskind* fermions: the Argonne Group, the Staggered Collaboration and the HEMCGC Collaboration in the U.S., the APE group again in Europe and the Japanese Kyoto-Tsukuba collaboration.

Argonne, working at high β (6.5) on large-L_t lattices ($L_t = 64$), [28] have produced preliminary results with errors of $\mathcal{O}(3–7\%)$. The Staggered group have results for a number of lattice sizes and β's [29] with similar errors and a good investigation of finite-size effects. APE's results at $\beta = 6.0$ and 5.7 [30, 31] show errors of $\mathcal{O}(8\%)$ and indicate that staggered fermions may have the edge over Wilson fermions for certain heavy mesons (the a_1, a_0 etc.).

2.6.3 Summary of progress

Progress has indeed been made in the ten years since $8^3 \times 16$ quenched lattices (see, for example, [32]), although perhaps not quite as much as might have been hoped then. Despite spectacular advances in computer technology (factors of $\mathcal{O}(100)$

in flops), algorithm design and theoretical understanding of chiral behaviour, the light hadron spectrum remains a hard nut to crack, even in quenched calculations. In current simulations, finite-size effects are being understood and controlled, finite-spacing effects are being tackled with improved actions and β values are being pushed well beyond 6.0 into (one hopes) the scaling regime. Errors on hadron masses, for an ever wider array of mesons and baryons, are of order a few percent, and central values are one or two standard deviations away from experiment.

Chapter 3

Jacobi Smearing

In this chapter I present the analysis and development of a technique designed to improve the signals for lightest-state hadrons in spectroscopic calculations. This technique, known as *smearing*, involves the use of improved hadron operators designed to have a larger overlap with the lightest s-wave states. The algorithm described here is comparatively cheap in terms of computer time and possesses the desirable property of maintaining the gauge-covariance of the operators.

In §(3.1) I discuss what is meant by smearing and why it is used. I develop the idea of gauge-covariant smearing in §(3.2) and discuss the details of general smearing at the source or sink in §(3.3). The ideas behind Wuppertal scalar-propagator smearing are given in §(3.4) and the details and development of the Jacobi smearing algorithm in §(3.5). I present some early results in §(3.6) to illustrate the kind of effects one hopes to achieve with smearing, and finally I summarise the findings of this chapter in §(3.7).

3.1 What is Smearing?

Let us re-examine Equation (2.27):

$$\begin{aligned} C_H(t) &\equiv \left\langle \sum_{\vec{x}} G_H(x,0) \right\rangle \\ &= \sum_n \frac{A_n}{2m_n}\, e^{-m_n t}. \end{aligned} \tag{3.39}$$

The coefficient A_n is the modulus squared of the overlap of the hadron operator with the state $|n\rangle$:

$$A_n \equiv |\langle 0\,|\phi(0)|\,n\rangle|^2 . \tag{3.40}$$

Recall that to extract the mass of the ground state $|1\rangle$ we need to eliminate contributions from all the higher-mass excited states $|n\rangle, n > 1$. There are, in practice, two ways to achieve this.

1. **The expensive way**. Perform the computer calculations on a lattice of extremely large time extent ($T\sim$100, say) with a sufficiently large number of configurations to ensure signals are not lost in statistical noise. This, of course, requires (a) a *very* large computer, and (b) a great deal of runtime.
2. **The cheap way**. Choose the hadron operator ϕ in such a way that the ground-state overlap $A_1 \gg A_m, (m > 1)$. The ground state will then dominate from small t onwards.

Naturally, the cheap way is to be preferred.

The ideal choice of hadron operator would be one that reproduces exactly the wavefunction of the s-wave ground state. Since the s-wave wavefunction is spherically symmetric with some characteristic non-zero radius, an acceptable choice for the lattice would be any finite-size operator with maximal reflection and rotation symmetry. Since the lattice possesses only a finite hypercubic sub-group of the usual reflection and rotation symmetries, this could be realised as some form of cube or octahedron.

3.2 Rationale Behind Gauge-Covariant Smearing

This idea of choosing hadron operators of extended size is no longer new. The earliest such operators proposed [33, 34] comprised a sum of the usual point operators over all spatial sites on the source timeslice. As can be appreciated, these choices are not gauge-covariant; while providing some improvement in the signal at small times, they lead to increased noise at later times. The problem of statistical noise can be alleviated by fixing the gauge so that noncovariance is no longer an issue, yielding "cube" [35] and "wall" [36] operators. However, fixing the gauge on the lattice raises the possibility of Gribov copies [37, 38, 39] and recent results using cube sources [40, 41] seem to show a worrying sensitivity of calculated masses to the size of the cube.

The possible problems involved in gauge-fixing can be avoided by choosing gauge-covariant operators. Such operators were first discussed in [42, 43]; the algorithm I shall use is a simpler version of the "Wuppertal" smearing described by Güsken [42] and first presented in [44].

The use of such gauge-covariant operator has a number of advantages over gauge-dependent ones such as cubes or walls:

- it obviates the need to fix the gauge, a process requiring additional stages in the generation of lattice gauge configurations;
- there exists no possibility of effects arising from the lattice Gribov ambiguity;
- it preserves an extremely important test for the development of new computer codes, namely the ability to perform random gauge transformations on data and check that calculations are unaffected, configuration by configuration;
- it is perhaps a more "intuitively correct" object to choose to represent a colour-singlet hadron.

3.3 Source and Sink Smearing

In lattice calculations of two-point hadron correlation functions the hadron is created at a single *source point*, usually the origin of the lattice at $t = 0$, and annihilated at all possible *sink points*. These sink points are then summed over the three spatial directions to obtain the timesliced hadron propagator from which masses are extracted. There are thus three choices for improving our hadron operators using smearing; smear the sink, the source or both.

Since the source lives on only a single timeslice (and, in practice, only one of four possible spin components) whereas the sinks lie on all timeslices, it is cheaper to smear at the source point (Figure 3.1). However, source smearing needs to be

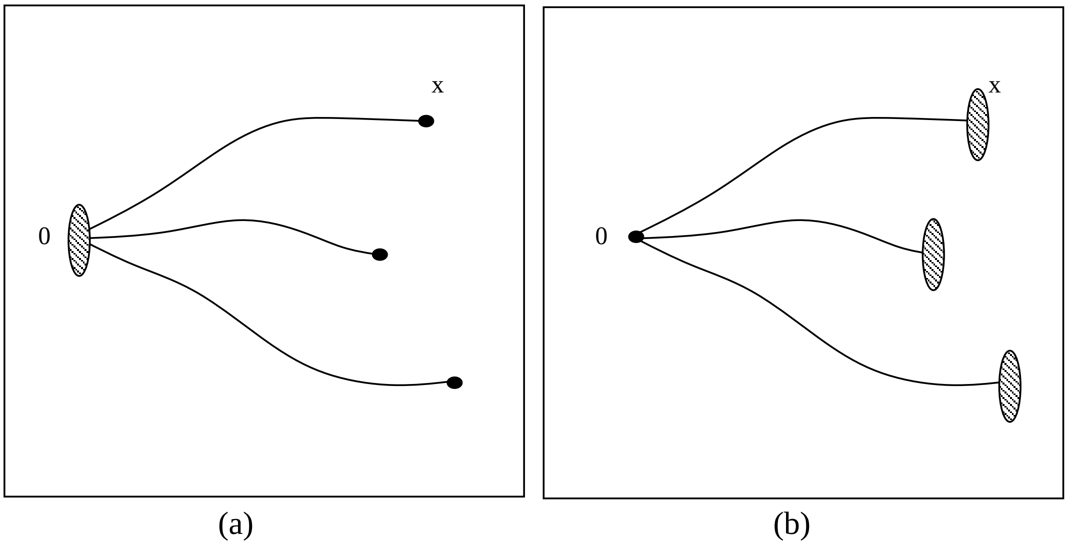

Figure 3.1: Schematic representation of (a) source and (b) sink smearing for three possible sink timeslices. The hatched area indicates a smeared operator.

done *before* the quark propagators comprising the hadron are calculated while sink smearing can be performed on an existing point-to-point propagator. In the limit of an infinite number of configurations these two approaches must have exactly the same effect, so the choice between source and sink smearing is largely a logistical one. However, since our smearing functions are formed from the links of the gauge fields, and gauge fields fluctuate between timeslices, applying smearing functions at all sinks tends to increase the statistical noise in the hadron signal. With foresight, therefore, source smearing is to be preferred.

As already touched upon, in practice it is not the hadron operator that is smeared but rather the quark fields comprising it. Since smearing is carried out at source and sink points, it is readily apparent that a hadron propagator with a smeared sink (say) is constructed from quark propagators with the same sink smearing. We define smeared quark-field operators as follows:

$$\psi^S(\vec{x},t) = S(\vec{x},\vec{y})\psi(\vec{y},t), \qquad \bar{\psi}^S(\vec{x},t) = \bar{\psi}(\vec{y},t)S^\dagger(\vec{y},\vec{x}) \tag{3.41}$$

for sink and source quark fields respectively. $S(\vec{x},\vec{y})$ is our spatial smearing function and there is an implied sum over $\vec{y}$. A sink-smeared quark propagator is then

$$\begin{aligned}\left\langle G^{SL}(x,0)\right\rangle &= \left\langle \psi^{S}(x)\bar{\psi}(0)\right\rangle \\ &= \left\langle S(\vec{x},\vec{y})\psi(y)\bar{\psi}(0)\right\rangle \\ &= \left\langle S(\vec{x},\vec{y})M^{-1}(y,0)\right\rangle \\ &= \left\langle \left(M(0,y)S^{-1}(\vec{y},\vec{x})\right)^{-1}\right\rangle . \end{aligned} \tag{3.42}$$

Calculation of $G^{SL}(x,0)$ then entails the solution of the matrix equation

$$\left[M(0,y)S^{-1}(\vec{y},\vec{x})\right] G^{SL}(x,0) = 1 \tag{3.43}$$

i.e.

$$M(0,y)G(y,0) = 1 \tag{3.44}$$

where $G(y,0)$ is the usual point-to-point propagator and

$$G^{SL}(x,0) = S(\vec{x},\vec{y})G(y,0). \tag{3.45}$$

This shows that, as noted above, a sink-smeared propagator can be obtained from the regular point-to-point propagator simply by multiplying in the smearing function.

The source-smeared propagator requires a little more computational forethought:

$$\begin{aligned}\left\langle G^{LS}(x,0)\right\rangle &= \left\langle \psi(x)\bar{\psi}^{S}(0)\right\rangle \\ &= \left\langle \psi(x)\bar{\psi}(y)S^{\dagger}(\vec{y},\vec{0})\right\rangle \\ &= \left\langle M^{-1}(x,y)S^{\dagger}(\vec{y},\vec{0})\right\rangle \\ &= \left\langle \left(\left(S^{\dagger}(\vec{0},\vec{y})\right)^{-1} M(y,x)\right)^{-1}\right\rangle . \end{aligned} \tag{3.46}$$

Hence, the propagator equation we must solve is

$$\left(S^{\dagger}(\vec{0},\vec{y})\right)^{-1} M(y,x)G^{LS}(x,0) = 1 \tag{3.47}$$

i.e.

$$M(y,x)G^{LS}(x,0) = S^{\dagger}(\vec{y},\vec{0}). \tag{3.48}$$

In this case, we must calculate our quark propagator $G \equiv M^{-1}$ using a smeared source as input to the matrix inverter.

For a quark propagator smeared at both sink and source we need to do both the above operations — invert the fermion matrix with a smeared source $S^\dagger$ and then multiply the result by the Hermitian conjugate S.

For any general smearing function we may define its characteristic size by the root-mean-square radius

$$R_{rms} = \sqrt{\frac{\sum_{\vec{x}} |\vec{x}|^2 |S(\vec{x},\vec{0})|^2}{\sum_{\vec{x}} |S(\vec{x},\vec{0})|^2}}. \tag{3.49}$$

This is a gauge-invariant quantity which can be used to quantify the "amount of smearing" of a given operator. It has been observed [44] that operators with larger smearing radii tend to yield better signals than "smaller" operators, with the suggestion that smearing radii $\sim$4 are desirable. I shall examine the behaviour of R_{rms} for gauge-covariant smearing functions in subsequent sections.

3.4 Wuppertal Smearing

The analysis of the previous section applies to any general smearing function. In this work I am interested particularly in gauge-covariant smearing functions. As already discussed, a sink- (source-) smeared hadron propagator is obtained from sink- (source-) smeared quarks; to simplify matters I shall present future analyses in terms of quark propagators only.

A gauge-covariant smeared quark field is defined by Equation (3.41) with the additional requirement that $S(\vec{x},\vec{y})\phi(\vec{y},t)$ transforms like $\phi(\vec{y},t)$ under $SU(3)$ gauge transformations. The choice proposed by the Wuppertal group [42] is to take S as the spatial propagator of a coloured, scalar particle

$$S(\vec{y},\vec{x}) = \left\langle \chi_i(\vec{y})\chi_i^\dagger(\vec{x}) \right\rangle, \tag{3.50}$$

where $i = 1\ldots3$ runs over $SU(3)$ colour. On the lattice, this is the inverse of the quadratic term in a three-dimensional scalar action,

$$\left\langle \chi_i(\vec{y})\chi_i^\dagger(\vec{x}) \right\rangle = \left\langle [M_{sc}(\vec{y},\vec{x})]^{-1} \right\rangle; \tag{3.51}$$

where

$$\begin{aligned} M_{sc}(\vec{y},\vec{x}) &= \delta(\vec{y},\vec{x}) - \kappa_{sc} \sum_{\mu=1}^{3} \left(\delta(\vec{y},\vec{x}-\hat{\vec{\mu}})U_\mu^\dagger(\vec{y}-\hat{\vec{\mu}}) + \delta(\vec{y},\vec{x}+\hat{\vec{\mu}})U_\mu(\vec{y}) \right) \\ &\equiv \delta(\vec{y},\vec{x}) - \kappa_{sc} D_{sc}^2(\vec{y},\vec{x}). \end{aligned} \tag{3.52}$$

Before analysing the lattice implementation of scalar-propagator smearing it will be instructive to look at the free-field case in the continuum.

3.4.1 Free-field Wuppertal smearing in the continuum

In the continuum, the free-field scalar propagator is simply the Fourier transform of the (inverse of the) three-dimensional Klein-Gordon operator (p^2+m^2), i.e.from a fixed origin $\vec{0}$,

$$
\begin{aligned}
\left\langle \chi(\vec{x})\chi^{\dagger}(\vec{0})\right\rangle &= \int \frac{d^3\vec{p}}{(2\pi)^3}\frac{\exp(-i\vec{p}.\vec{x})}{p^2+m_{sc}^2} \\
&= \frac{1}{(2\pi)^3}\int_0^{\infty} dp \int_0^{2\pi} d\phi \int_0^{\pi} d\theta \; p^2 \sin\theta \; \frac{e^{-ipr\cos\theta}}{p^2+m_{sc}^2} \\
&= \frac{i}{(2\pi)^2}\int_0^{\infty} dp \; \frac{p^2}{p^2+m_{sc}^2}\frac{1}{pr}\left(e^{-ipr}-e^{ipr}\right) \\
&= \frac{i}{(2\pi)^2\, r}\int_{-\infty}^{\infty} dp \; \frac{p}{(p+im_{sc})(p-im_{sc})}e^{-ipr} \\
&= \frac{i}{(2\pi)^2\, r}(-2\pi i)\ \mathrm{Res}(p=-im_{sc}) \\
&= \frac{1}{4\pi\, r}e^{-m_{sc}r} \qquad (3.53)
\end{aligned}
$$

where m_{sc} is the mass of the scalar particle, $r = |\vec{x}|$ and $p = |\vec{p}|$. This varies smoothly away from the origin and provides us with an object that possesses the same spherical symmetry as the s-wave wavefunction. Using this function, the expected value of the mean-squared radius becomes

$$
\begin{aligned}
\overline{R^2_{rms}} &= \frac{\int_0^{\infty}(4\pi r^2)\, r^2 \left(\frac{1}{(4\pi r)^2}e^{-2m_{sc}r}\right) dr}{\int_0^{\infty}(4\pi r^2)\left(\frac{1}{(4\pi r)^2}e^{-2m_{sc}r}\right) dr} \\
&= \frac{1}{(2m_{sc})^3}\Gamma(3)\Big/\left(\frac{1}{2m_{sc}}\right) \\
&= \frac{1}{2m_{sc}^2}. \qquad (3.54)
\end{aligned}
$$

As one expects intuitively, the radius behaves like a correlation length and varies as the inverse of the scalar mass. We can use this result to qualify the behaviour of the propagator on the lattice.

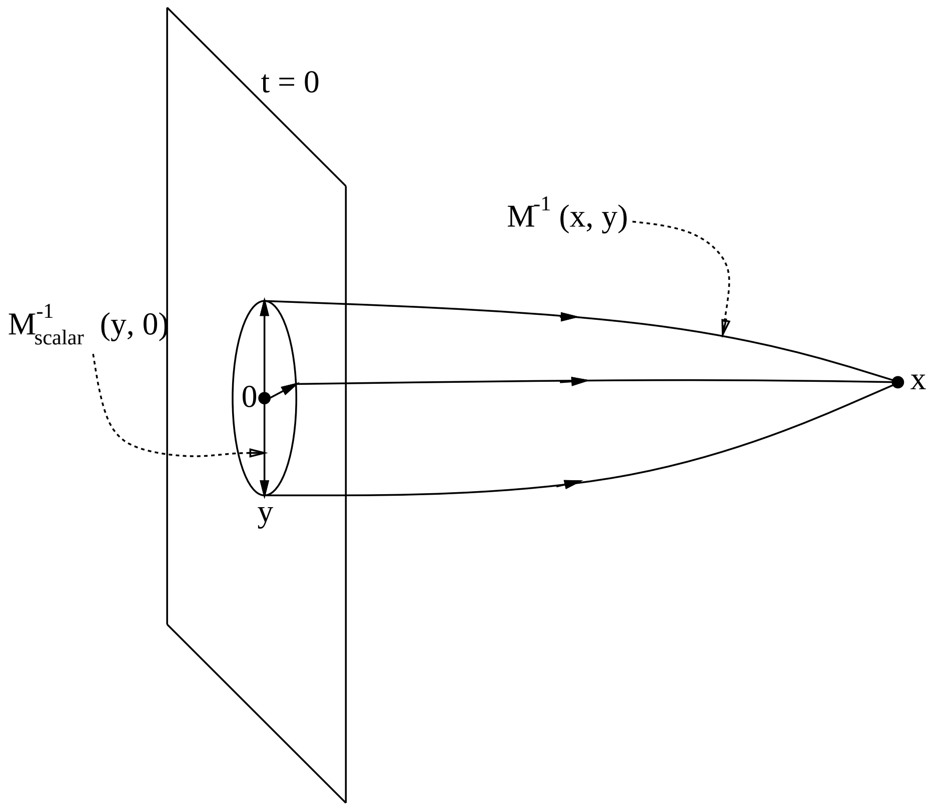

Figure 3.2: Propagator picture of Wuppertal-smeared source. The quark field is smeared about the origin with the scalar propagator then tied with fermion propagators to all sink-points x.

3.4.2 Wuppertal smearing on the lattice

In direct analogy with the fermion kernel in the full QCD action presented in Chapter 1 we write the scalar mass m_{sc} in terms of the "hopping parameter" κ_{sc}. Calculation of the scalar propagator is a similar problem to that of extracting the quark propagator, namely the solving of a matrix equation

$$\sum_{\vec{y}} M_{sc}(\vec{x}, \vec{y}) S(\vec{y}, \vec{0}) = \delta(\vec{x}, \vec{0}). \tag{3.55}$$

I use $\vec{0}$ to denote the origin about which our smearing function is centered. For a source-smeared quark field, the scenario is as pictured in Figure 3.2.

If M_{sc} is singular, Equation (3.55) has no solution and the matrix inversion will fail. Numerically, a given inversion algorithm may still fail if the matrix is close to being singular — it will certainly take longer to converge to a solution the closer the matrix is to singularity. For M_{sc}, singular behaviour is governed by the parameter κ_{sc}. For instance, in the free-field case

$$\begin{aligned}
\tilde{M}(\vec{p}) &= \sum_{\vec{x}} e^{i\vec{p}\cdot\vec{x}} M_{sc}(\vec{x},\vec{y}) \\
&= \sum_{\vec{x}} e^{i\vec{p}\cdot\vec{x}} \left[\delta(\vec{x},\vec{y}) - \kappa_{sc} \sum_{\mu=1}^{3} \left(\delta(\vec{x},\vec{y}-\vec{\mu}) + \delta(\vec{x},\vec{y}+\vec{\mu}) \right) \right] \\
&= \left[1 - \kappa_{sc} \sum_{\mu=1}^{3} \left(e^{ip_\mu} + e^{-ip_\mu} \right) \right] e^{i\vec{p}\cdot\vec{y}} \\
&= \left[1 - 2\kappa_{sc} \sum_{\mu=1}^{3} \cos p_\mu \right] e^{i\vec{p}\cdot\vec{y}},
\end{aligned} \tag{3.56}$$

which is diagonal in $\vec{p}$-space. Here, I define the spatial momentum components $p_\mu \equiv \vec{p}\cdot\vec{\mu}$, where $\vec{\mu}$ is the unit vector in the μ direction. For $\vec{p} \to 0$, $\tilde{M} \to 1 - 6\kappa_{sc}$ which vanishes for $\kappa_{sc} = \kappa_{sc}^{crit} = 1/6$. Thus, as κ_{sc} approaches this critical value, zero modes appear in the matrix and it becomes singular.

To use the scalar propagator to generate a smearing function in the non-free-field case, we must know the critical value of κ_{sc} beyond which our matrix inverter will fail. To do this, we examine the continuum limit $a \to 0$ of the scalar action $S_{sc} = \bar{\chi}\ M_{sc}\ \chi$. If we take the free-field case again, defining continuum scalar fields by

$$\varphi \equiv \sqrt{\kappa_{sc}}\, a^{-3/2}\, \chi,$$

and Taylor expanding the $\bar{\chi}\ D_{sc}^2\ \chi$ term in powers of a, we arrive at the relation

$$m_{sc}^2 = \frac{1}{\kappa_{sc}} - \frac{1}{1/6}. \tag{3.57}$$

Recall that, from Equation (3.56), $1/6$ is the free-field value of κ_{sc}^{crit}. In addition, Equation (3.54) tells us that $m_{sc}^2 \sim 1/R_{rms}^2$. So, by plotting $1/R_{rms}^2$ against $1/\kappa_{sc}$ we can get a qualitative handle on κ_{sc}^{crit} — Figure 3.3 [46]. This plot was obtained from a $16^3 \times 48$ lattice on a single gauge configuration at $\beta = 6.2$. The line is a linear fit to the five smallest values of $1/\kappa_{sc}$; if we extrapolate this line to $1/R_{rms}^2 = 0$ we obtain

$$\kappa_{sc}^{crit} = 0.185. \tag{3.58}$$

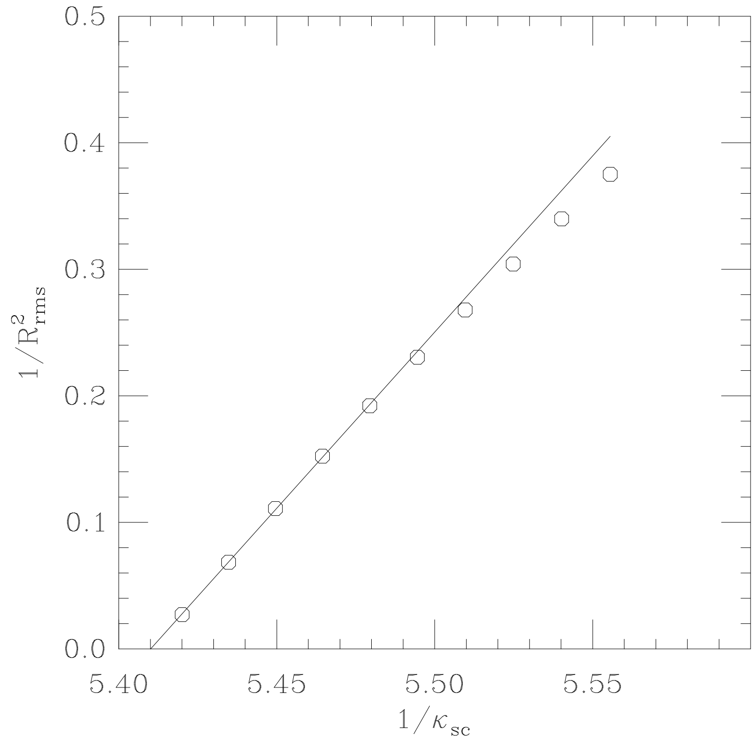

Figure 3.3: Plot of $1/R^2_{rms}$ versus $1/\kappa_{sc}$ for several Wuppertal smearing functions. The line is a fit to the first 5 points; the intercept at $1/R^2_{rms} = 0$ defines κ_{sc}^{crit}.

The maximum practicable r.m.s. radius attainable from Wuppertal smearing is $R_{rms}(\kappa_{sc} \sim 0.184) \approx 3.2$ (on this lattice size); beyond this the critical slowing down induced by $\kappa_{sc} \to \kappa_{sc}^{crit}$ makes the calculation of the scalar propagator prohibitively expensive — in the case of sink smearing, inverting M_{sc} at $\kappa_{sc} = 0.184$ on each timeslice is as demanding as calculating the actual quark propagator. Thus, for large radii Wuppertal smearing becomes impractical.

However, we need not be concerned with inverting M_{sc} *exactly* — the scalar particle is *not* a quantity of physical interest. Our only requirement is to generate some suitable “s-wave-like” function, not necessarily an exact scalar wavefunction. By judicious choice of algorithm it is possible to generate acceptable shapes from the scalar propagator without enormous overheads.

3.5 The Jacobi Smearing Algorithm

The most naïve way of inverting Equation (3.55) is to use the Jacobi algorithm (see, for example, reference [45]). This is the simplest numerical algorithm for inverting sparse matrices; for exact inversions there are many superior techniques — conjugate gradients, minimal residual etc. — but the Jacobi method possesses features which lend themselves readily to the inexpensive evaluation of our smearing function.

The Jacobi algorithm for solving our propagator equation

$$M_{sc}(\vec{x},\vec{y})S(\vec{y},\vec{0}) = \delta(\vec{x},\vec{0}) \tag{3.59}$$

is:

1. decompose M_{sc} into diagonal and off-diagonal parts (Equation (3.52)):
$$M_{sc}(\vec{x},\vec{y}) = \delta(\vec{x},\vec{y}) - \kappa_{sc} D^2_{sc}(\vec{x},\vec{y}); \tag{3.60}$$
2. choose the initial guess $S^{(0)}(\vec{y},\vec{0})$; usually this will be the point operator $\delta(\vec{y},\vec{0})$;
3. apply the following iterative scheme for the Nth approximation to the solution:

$$\delta(\vec{x},\vec{y})S^{(N)}(\vec{y},\vec{0}) = \delta(\vec{x},\vec{0}) + \kappa_{sc} D^2_{sc}(\vec{x},\vec{y})S^{(N-1)}(\vec{y},\vec{0}). \tag{3.61}$$

$$\Rightarrow \qquad S^{(N)}(\vec{x},\vec{0}) = \delta(\vec{x},\vec{0}) + \sum_{n=1}^{N} \left(\kappa_{sc} D^2_{sc}(\vec{x},\vec{y})\right)^n S^{(0)}(\vec{y},\vec{0}). \tag{3.62}$$

To solve exactly for $S = M_{sc}^{-1}$, Equation (3.62) would normally be iterated to convergence in the limit $N \to \infty$. However, a perfectly acceptable function shape can be obtained by truncating this series after a finite number of iterations, $N \sim \mathcal{O}(100)$. Each iteration causes the scalar particle to "hop" forwards and backwards in all directions, as shown in Figure 3.4. As is clear from the figure, this hopping process builds up a diamond (in two dimensions) or, in three dimensions, an octahedral shape composed of gauge links and factors of κ_{sc}. This is exactly what we want for our smearing function.

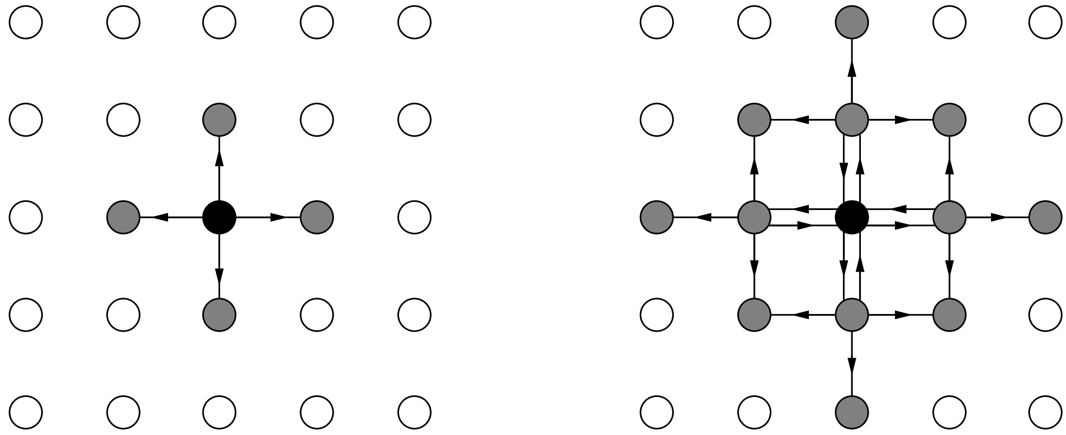

(a) (b)

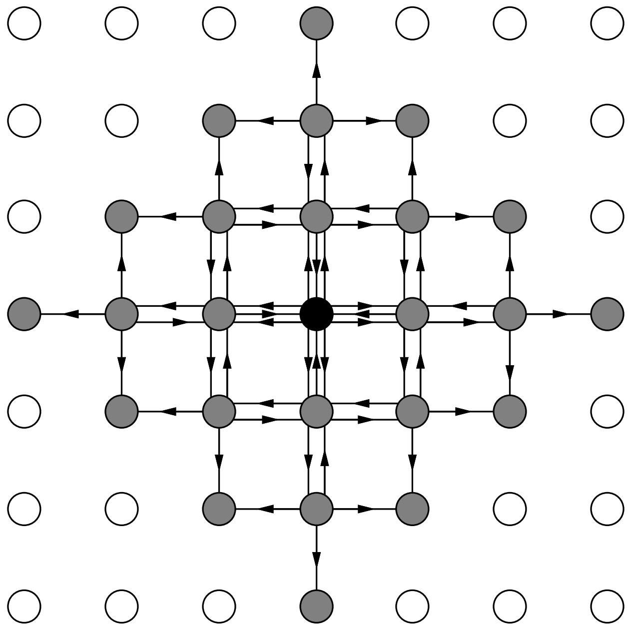

(c)

Figure 3.4: Diagrammatic illustration of the Jacobi smearing algorithm showing the shape generated with (a) 1, (b) 2 and (c) 3 iterations. Each link is weighted by the gauge-field and a factor of κ_{sc}.

So, to define our gauge-covariant smearing function we choose a value of κ_{sc} and a maximum number of iterations N and generate the function using Equation (3.62). The questions then arise: how do the shape and size of the function depend on κ_{sc} and N?

3.5.1 Dependence of $S(x,y)$ on κ_{sc} and N

I undertook a study to determine the dependence of R_{rms} on the two parameters κ_{sc} and N and hence the most economical way to generate suitable smearing functions. At first sight the problem is more complicated than the Wuppertal case — with κ_{sc} *and* N we have doubled our parameter space. However, it turns out that for a given R_{rms} only one parameter, N, is really relevant. Furthermore since we are no longer interested in inverting M_{sc} exactly, we are free to use values of $\kappa_{sc} > \kappa_{sc}^{crit}$; the fact that the Jacobi series, Equation (3.62), will not converge is of no consequence for finite N.

I performed the study on a $16^3 \times 48$ lattice at gauge-coupling $\beta = 6.2$, calculating smearing functions on different timeslices of a single gauge configuration. The programs used were written in FORTRAN by myself and David Henty on SUN workstations and, latterly, on the Edinburgh CM-200. The gauge configurations were generated on the Edinburgh i860 Grand Challenge machine, Maxwell.

The pseudo-code fragment in Table 3.1 indicates how the Jacobi smearing algorithm is implemented. In practice, since the scalar particle possess an $SU(3)$ colour index, creating a full smearing function involves smearing three delta-function sources, one for each component i. The residue in step 8, residue(i) for each colour component, indicates how close or otherwise we are from an exact solution to Equation (3.55).

Most of the work is done in steps 4–6 which performs the actual iteration of Equation (3.62). The amount of work required to calculate the smearing function thus depends most heavily on N. This gives us one criterion for the choice of our parameters: to generate a smearing function of a given R_{rms} as economically as possible we need to minimise the number of iterations.

Initially, I explored the region $\kappa_{sc} \leq \kappa_{sc}^{crit}$. In Figure 3.5 I show two plots of R_{rms}

```
BEGIN LOOP i = 1 ... 3;
    SET source(i,x,j) = DELTA FUNCTION AT ORIGIN;
    SET S^(0)(i,x,j) = source(i,x,j);
    BEGIN LOOP n = 1 ... N;
        SET S^(n)(i,x,j) = source(i,x,j) + κ_sc D²_sc S^(n-1)(i,x,j);
    END LOOP n;
    SET [S†S](i,x) = Σ_{j=1}^{3} S^(N)†(i,x,j) S^(N)(i,x,j);
    SET residue(i) = |source(i,x,j) − (1 − κ_sc D²_sc) S^(N)|²;
END LOOP i;
SET F(x) = Σ_{i=1}^{3} [S†S](i,x);
SET R_rms = sqrt( Σ_x x² F(x) / Σ_x F(x) ).
```

Table 3.1: Pseudo-code fragment detailing the implementation of the Jacobi smearing algorithm.

against N for a number of κ_{sc}'s in the region of κ_{sc}^{crit}. It is clear from this figure that

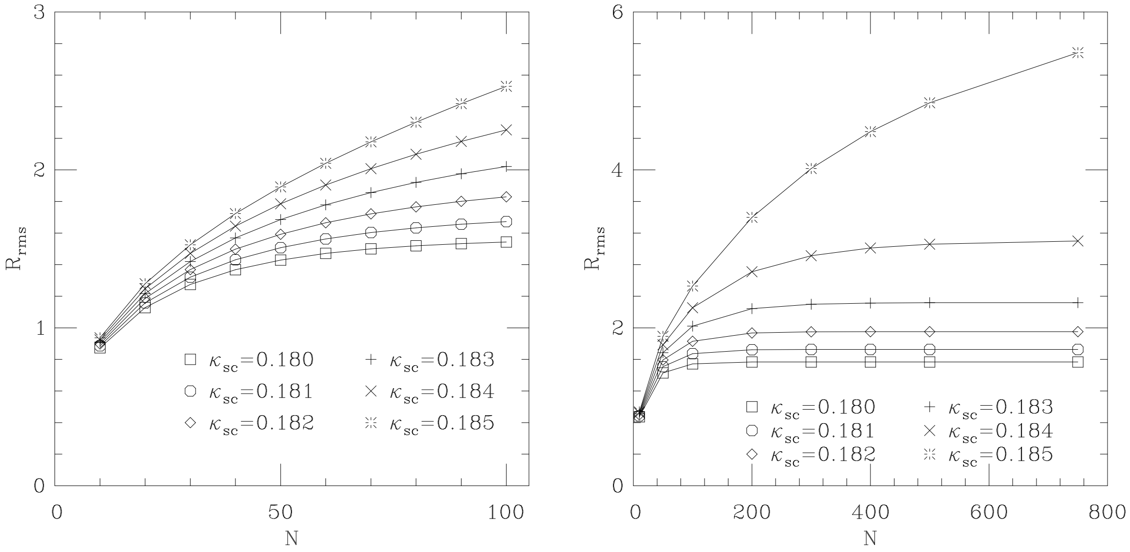

Figure 3.5: R.m.s. radius against number of iterations of the Jacobi series for the regime $\kappa_{sc} \leq \kappa_{sc}^{crit}$.

as $\kappa_{sc} \to \kappa_{sc}^{crit}$ the series is failing to converge. The curve for $\kappa_{sc} = \kappa_{sc}^{crit} = 0.185$ defines an envelope below which all the curves will converge onto some R_{rms} as $N \to \infty$. However we see that we need several hundred iterations — a significant amount of computer time — to achieve radii greater than 3, and only then for $\kappa_{sc} \simeq \kappa_{sc}^{crit}$. For an acceptable computational overhead, $N \sim 100$, the maximum radius is only ~ 2.5 at $\kappa_{sc} = \kappa_{sc}^{crit}$. For κ_{sc} less than the critical value the Jacobi algorithm yields poor results.

However, since we have no convergence criterion in the Jacobi algorithm we are free to investigate the region $\kappa_{sc} > \kappa_{sc}^{crit}$. In Figure 3.6 I present the complementary plot to Figure 3.5. From this we can clearly see that to obtain smearing functions with larger radii it is necessary to take $\kappa_{sc} > \kappa_{sc}^{crit}$. This figure also shows that for a fixed number of iterations there is little to be gained from increasing κ_{sc} beyond ~ 0.25. This provides a strong hint that N is the parameter which controls the size of the smearing function for κ_{sc} above the critical value.

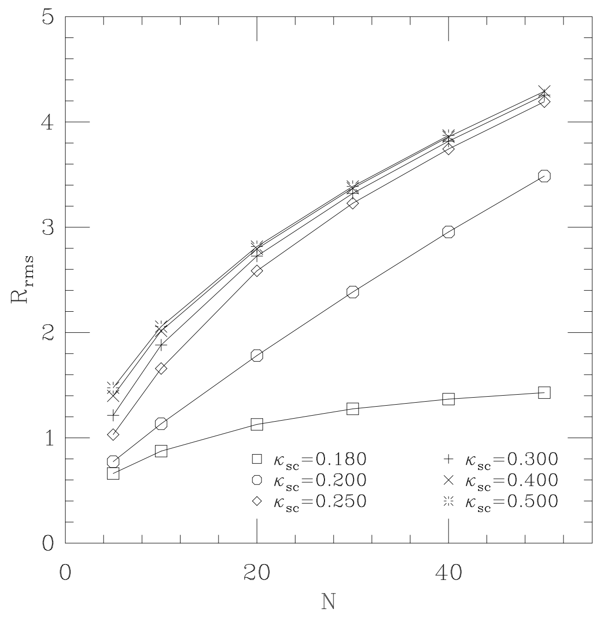

Figure 3.6: R.m.s. radius against number of iterations of the Jacobi series for the regime $\kappa_{sc} \gtrsim \kappa_{sc}^{crit}$.

This conclusion is born out by Figure 3.7 in which I show the variation of smearing radius with κ_{sc} for different values of N. Above 0.25, κ_{sc} becomes largely irrelevant and the size of the smearing function is controlled by the number of iterations of the Jacobi series.

Figure 3.7 has several "missing points" for larger values of N and κ_{sc}. There is a problem in this region caused by the rapid growth of the norm of the function $S(\vec{x}, \vec{0})$. When $N \times \kappa_{sc}$ becomes too large, the norm blows up beyond the limits

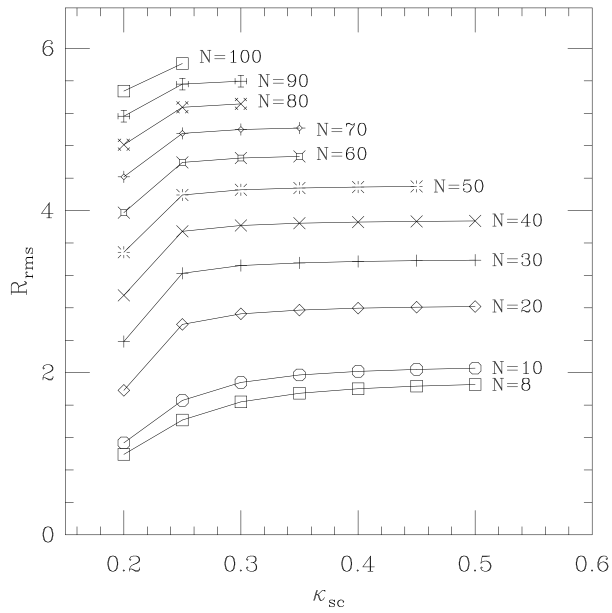

Figure 3.7: R.m.s. radius against κ_{sc} for various values of N.

of the computer and the algorithm breaks down. It has been observed [47] that the norm actually grows exponentially as

$$\left\| S(\vec{x}, \vec{0}) \right\| \sim e^{N\alpha(\kappa_{sc} - \kappa_{sc}^{crit})} \tag{3.63}$$

where $\alpha \approx 4.0$. The exponential behaviour is clearly shown in Figure 3.8. The parameter α is determined from fits to these curves; taking data for $N = 128$ and $N = 64$ as shown and performing a simple linear fit with (assumed) 10% errors on log $\|S\|$ we find

$$\begin{aligned} \alpha &= 3.9, \quad (N = 64) \\ \alpha &= 4.3, \quad (N = 128) \end{aligned} \tag{3.64}$$

This is only an approximate "back-of-the-envelope" calculation but it gives at least a semi-quantitative idea of how the norm behaves with N and κ_{sc}. This is important since it means that, after generation, the smearing function can always be normalised to a size $\mathcal{O}(1)$ before we use it to smear any quark propagators. This avoids any undesirable numerical problems from multiplying machine-large numbers by machine-small ones.

So far I have shown how the r.m.s. radius varies as a function of N and κ_{sc}.

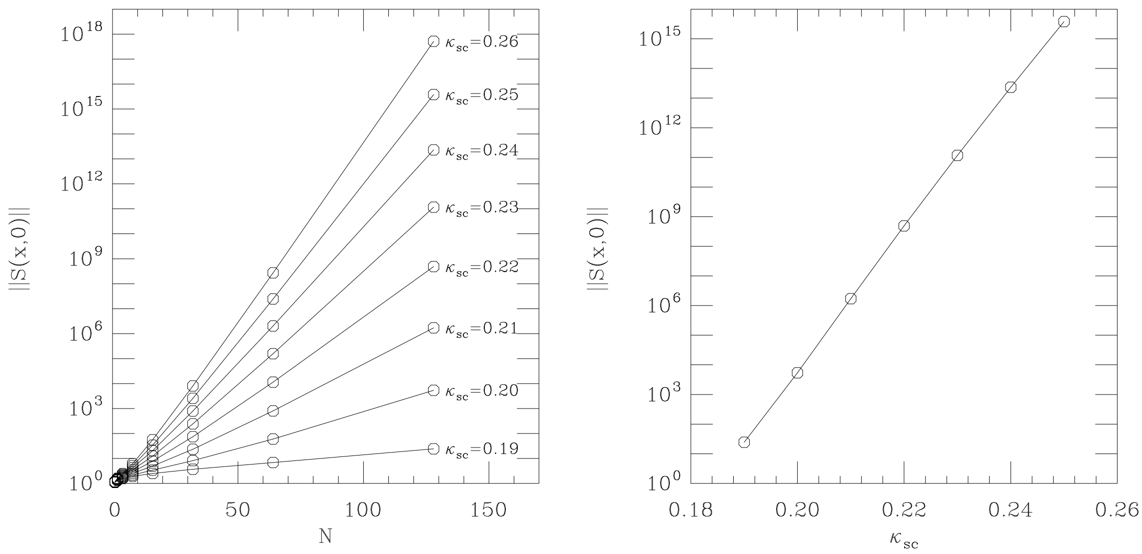

Figure 3.8: The norm of the Jacobi smearing function, $\log \|S\|$, as a function of N and as a function of κ_{sc} for $N = 128$.

In Figure 3.9 I present three-dimensional plots of the actual smearing functions themselves for parameter choices

(a) 50 Jacobi iterations at $\kappa_{sc} = 0.25$ ($R_{rms} = 4.2$),

(b) 90 Jacobi iterations at $\kappa_{sc} = 0.19$ ($R_{rms} = 3.9$) and

(c) converged Wuppertal at $\kappa_{sc} = 0.184$ ($R_{rms} = 3.1$).

The plots show

$$F(x, y) \equiv \frac{1}{Volume} \sum_z \sqrt{Tr\ S^\dagger(x, y, z; \vec{0}) S(x, y, z; \vec{0})}, \tag{3.65}$$

where x, y, z refer to the three Cartesian coordinate directions and we have normalised each function by its total volume

$$Volume \equiv \sum_{x,y,z} \sqrt{Tr\ S^\dagger(x, y, z; \vec{0}) S(x, y, z; \vec{0})}. \tag{3.66}$$

The similarity in the shapes indicates that using the truncated Jacobi series for $\kappa_{sc} > \kappa_{sc}^{crit}$ still yields a perfectly acceptable smearing function, even though the series will not converge in the limit $N \to \infty$. The differences are qualitative; using a larger value of κ_{sc} tends to give a "shorter, fatter" function shape.

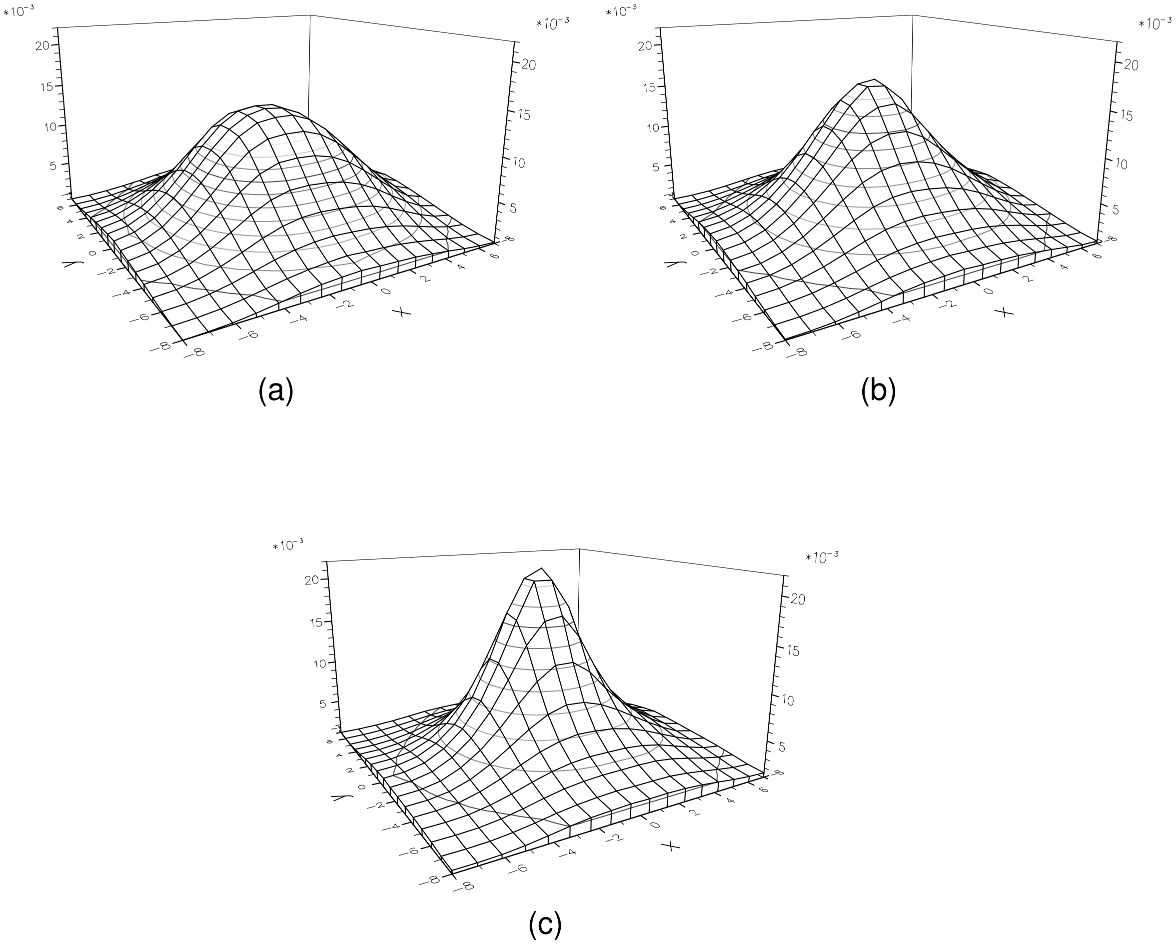

Figure 3.9: The shapes of the smearing functions $\sqrt{Tr\ S^{\dagger}S}$ in the x–y plane for (a) 50 Jacobi iterations, $\kappa_{sc} = 0.25$, (b) 90 Jacobi iterations, $\kappa_{sc} = 0.19$ and (c) converged Wuppertal, $\kappa_{sc} = 0.184$. The vertical scales are the same for each plot.

As a final point in this section I indicate, in Figure 3.10, the variations of the r.m.s. radius with timeslice t. Previous results presented here were based on calculations at a single timeslice on a single gauge configuration. Figure 3.10 gives some indication of how the size of the smearing function varies across a single gauge configuration, choosing different timeslices to smear on. We see

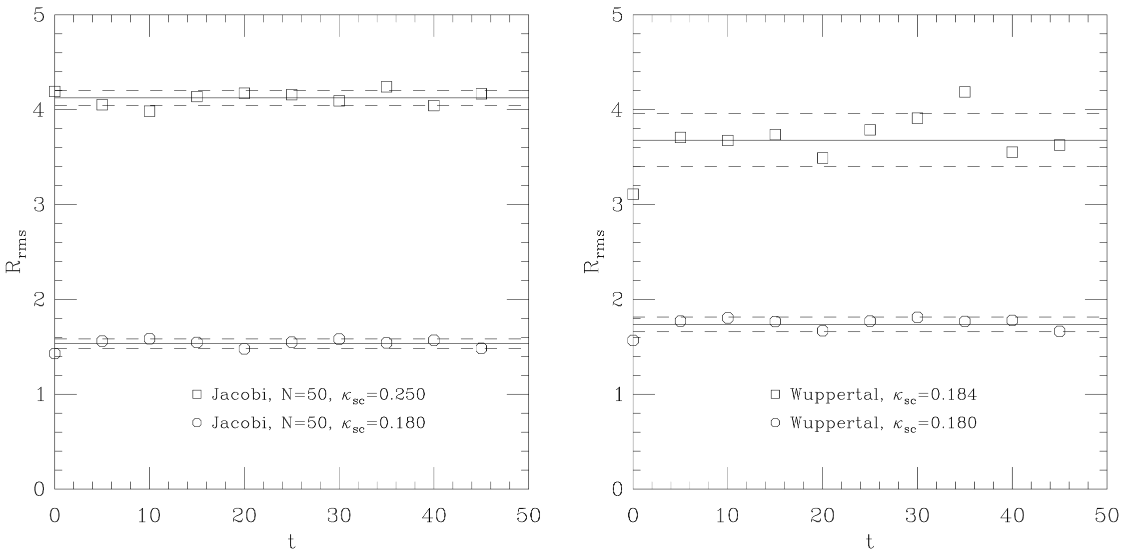

Figure 3.10: R.m.s. radius as a function of timeslice for Jacobi smearing functions (left) with $N = 50$ and $\kappa_{sc} = 0.25$ and 0.18 and for Wuppertal functions with $\kappa_{sc} = 0.180$ and 0.184. The solid lines correspond to the naive average radius; the dotted lines are 1–σ errors.

that the radii calculated from the Wuppertal functions fluctuate more than those from the Jacobi. Comparing the two lower lines, both of $\kappa_{sc} = 0.180$, we might conclude that the greater number of iterations involved in the Wuppertal case lead to slightly increased fluctuations in R_{rms}. Percentage-wise,

$$\begin{aligned} \frac{\sigma}{(\overline{R_{rms}})} &= 4.4\% \qquad \text{(Wuppertal)}, \\ \frac{\sigma}{(\overline{R_{rms}})} &= 3.3\% \qquad \text{(Jacobi, } N = 50\text{)}. \end{aligned} \tag{3.67}$$

However, for comparable radii of ~ 4 the difference in the relative fluctuations is much greater:

$$\begin{aligned} \frac{\sigma}{(\overline{R_{rms}})} &= 7.6\% \qquad \text{(Wuppertal, } \kappa_{sc} = 0.184\text{)}, \\ \frac{\sigma}{(\overline{R_{rms}})} &= 1.9\% \qquad \text{(Jacobi, } \kappa_{sc} = 0.25,\ N = 50\text{)}. \end{aligned} \tag{3.68}$$

A possible explanation is that since the Wuppertal function is an (almost) exact scalar propagator it will have a long tail. This will wrap around on the lattice, possibly many times, reinforcing the fluctuations from the gauge fields. In the Jacobi case, we have "cut off the tail" after 50 "hops" from the origin, thereby curtailing the effects of fluctuations in the gauge fields.

Although I have only measured the fluctuation of R_{rms} between timeslices on a single configuration, the result carries over naturally into a configuration-by-configuration fluctuation. This is yet another desirable feature of the Jacobi algorithm, particularly for sink smearing where any fluctuations in smearing function between timeslices will have an adverse effect on the hadron propagator signal.

3.6 Effects of Smearing

As a coda to the discussion of Jacobi smearing techniques I shall present here results of actual hadron propagator calculations using Jacobi smeared sources and sinks. They are based on the analysis of 30 configurations at $\beta = 6.2$ on a $24^3 \times 48$ lattice, using the Wilson action at a single κ value of 0.152 (details can be found in reference [48]). These results are an extension of the 18 configuration data first presented in reference [44]. In Figure 3.11 I show the effective mass plots for various light hadrons, $m_{eff}(t) \equiv \log\left(\frac{C_H(t)}{C_H(t+1)}\right)$, where $C_H(t)$ is the hadron correlation function as defined in Equation (3.39).

The notation is such that "LS" means "local (point) sink, smeared source". The smearing function used for these calculations was generated using the Jacobi method with $N = 50$ iterations at $\kappa_{sc} = 0.25$ — an R_{rms} of $\sim$4.2. It is clear that the use of smearing has killed off the effects of many higher excited states near the origin — witness the much steeper gradient between timeslices 1 and 8 for the LL case. There is a small gain in the onset of plateaux in each of the four signals, notably for the baryons in the SL and SS cases. However, the gain is only of the order of 1 or 2 timeslices; it may mean we need to increase the smearing radius beyond 4 to see more gain.

Additionally, we see that the LL vector signal actually shows little sign of a

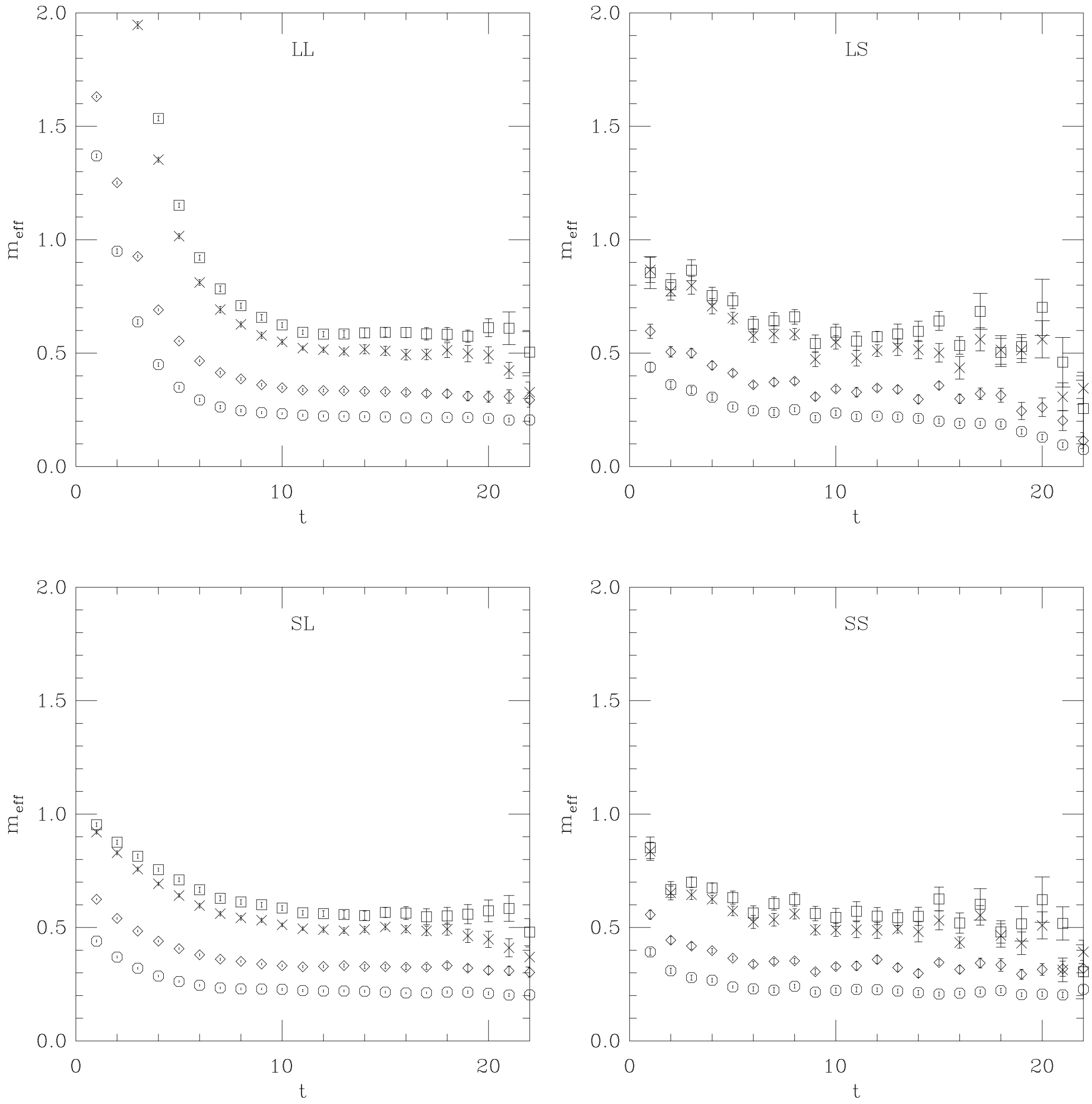

Figure 3.11: Effective masses of the pseudoscalar (○) and vector (◇) mesons and the nucleon (×) and delta (□) baryons calculated using LL, LS, SL and SS propagators.

plateau. There is a steady monotonic decrease which is notably absent in the SL plot. This suggests that excited state contamination persists for a long time in the LL data, but can be eradicated much sooner by using smeared operators. This feature of the vector signal also appears in the analysis using the clover action — see §(4.2) for a discussion.

Another feature of note is the difference in noise between, in particular, the LS and SL data. This lends support to the earlier remark that smearing at the sinks on all timeslices is likely to increase the noise in the propagator signal, although sink and source smearing should be identical in the infinite-configuration limit.

3.7 Summary

The investigations of the preceding sections lead me to summarise the main points of gauge-covariant Jacobi smearing as follows:

- as a gauge-covariant method, Jacobi smearing avoids problems that might arise from gauge-fixing and maintains gauge-invariance throughout all steps of spectroscopic calculations — invaluable for program development;
- compared with Wuppertal smearing it is fast and thereby economical;
- smearing functions with large radii are easy to generate with $\kappa_{sc} \sim 0.25$;
- the size of the smearing function can essentially be defined in terms of a single parameter, the number of iterations N;
- the behaviour of the divergent Jacobi series is quantifiable and can be controlled if necessary;
- the size of the Jacobi function is less affected by timeslice-to-timeslice fluctuations in the gauge fields than is the Wuppertal function;
- Jacobi smearing shows some improvement for the extraction of hadron masses, particularly for baryons.

As a final remark on the last point: although the use of smearing does remove contributions from many of the higher excited states near $t = 0$, the lower-mass states persist. For light hadrons this is not too worrisome since the lighter states are separated by comparatively large mass gaps — the excited states are markedly heavier than the ground state. However, for hadrons comprising one or more heavy quarks the excited states are much closer together and contaminant states persist longer. For these heavy hadrons, smearing becomes almost essential to extract any ground-state signal at all. The results I shall present in Chapter 5 derive in part from heavy-quark propagators smeared using the Jacobi algorithm.

Chapter 4

Results for Light-Hadron Spectroscopy

In this chapter I shall present the results of extensive calculation and analysis of the lattice hadron spectrum in the light (u and d) and strange (s) quark sectors. These calculations were performed as part of UKQCD, using the Maxwell spectrum codes of Chapter 2 and fitting/analysis codes written by myself, Jim Simone and others.

In §(4.1) I describe the fitting procedure used in the analysis of the hadron data. In §(4.2) I attempt to quantify some of the systematic errors involved in the determination of hadron masses, and in §(4.3) I present the raw lattice data for a range of hadron masses and meson decay constants. §(4.4) looks at the dependence of primarily mesonic quantities on two quark masses and §(4.5) covers the extrapolation of results to the chiral u and d quark limit. In §(4.6) I discuss the calculation and use of the strange quark mass and in §(4.7) I present the final results, in physical units, for the light–strange sectors. I also discuss here the uncertainties associated with the renormalisation of the meson decay constants. Finally, by way of a slight digression, I discuss, in §(4.8), some interesting results concerning the ratio $R \equiv f_K/\sqrt{f_\pi f_{\pi'}}$ and its relation to chiral perturbation theory.

4.1 Statistics and Fitting Procedure

The results of this chapter are based on the analysis of 60 gauge configurations generated according to the prescription of §(1.4.1), with quark propagators calculated as described in §(1.4.2). The gauge configurations, quark propagators and hadron correlators were all generated on Maxwell.

In the light sector, we calculated quark propagators at three values of the hopping parameter κ, 0.14144, 0.14226 and 0.14262, corresponding to pseudoscalar meson masses of 790–440 MeV. These are very close to the lightest pseudoscalars that can be directly simulated with current technology — the "world lightest" at the present time is around 390 MeV (see, for example, reference [17]).

Meson correlators were built from quark propagators with all possible combinations of the three κ values, yielding three degenerate and three non-degenerate sets of correlators. For the baryons, we used only the degenerate combinations, giving us baryon correlators at three quark masses. Despite the much-vaunted smearing techniques presented in Chapter 3, the logistics of the UKQCD programme meant that only quark propagators with local sources/sinks were available for these calculations. With such small quark masses the effects of smearing amount to a gain of a few timeslices in the onset of plateaux in the effective masses [44]; consequently we do not anticipate great losses from the use of local operators. The interpolating operators used for the various meson and baryon channels are described in §(2.3).

To extract the hadron masses from the correlators we fit the zero-momentum, timesliced correlators to exponentially decaying functions of time. Since the lattice is periodic in all spacetime directions, our interpolating operators create states that propagate both backwards and forwards in time. The simulation should be symmetric under (lattice) time reversal; to reinforce this we average the forward and backwards moving states about the midpoint, $L_t/2$. For baryon states, we average the upper two spinor components of the forward-moving state with the lower two components of the backwards state. A consequence of this is that we must use different fit-functions for mesons and baryons.

4.1.1 Fit functions for hadron correlators

mesons:

$$\lim_{t,L_t\to\infty} C_M(t) = A_M \left(e^{-m_M t} + e^{-m_M(L_t-t)}\right) \quad (t < L_t) \tag{4.69}$$

(cf. Equation (2.35));

baryons:

$$\lim_{t,L_t\to\infty} C_B(t) = A_B\, e^{-m_B t} \qquad (t \leq L_t/2). \tag{4.70}$$

As well as hadron masses, we are able to extract the decay constants for the pseudoscalar and vector mesons, f_P and f_V:

$\boldsymbol{f_P}$**:**

$$\lim_{t,L_t\to\infty} \frac{\sum_{\vec{x}}\langle A_4(\vec{x},t)P^\dagger(0)\rangle}{\sum_{\vec{x}}\langle P(\vec{x},t)P^\dagger(0)\rangle} = \frac{f_P m_P}{Z_A\langle 0|P|P\rangle}\tanh m_P(L_t/2-t), \tag{4.71}$$

where $\langle 0|P|P\rangle$ and m_P are determined from the fit to the pseudoscalar mass;

$\boldsymbol{f_V}$**:**

$$\lim_{t,L_t\to\infty} \sum_{i=1}^{3}\sum_{\vec{x}}\langle V_i(\vec{x},t)V_i^\dagger(0)\rangle = \frac{3m_V^3}{2Z_V^2 f_V^2} e^{-m_V L_t/2}\cosh m_V(L_t/2-t), \tag{4.72}$$

where m_V is similarly extracted from the vector mass fit.

In Equations (4.71) and (4.72), the factors Z_A and Z_V are renormalisation constants, required to ensure that the pseudoscalar and vector currents obey the correct algebra in the continuum limit [49]. A degree of uncertainty in the determination of these factors gives rise to corresponding uncertainties in the values of f_P and f_V determined on the lattice — see §(4.7) for a fuller discussion.

4.1.2 Correlated-χ^2 fitting

To fit the timesliced data to the forms (4.69)–(4.72) we make use of a *least-*χ^2 procedure. We define a *goodness-of-fit* function, $\chi^2(\vec{a})$, as a function of our required fit parameters $\vec{a}$, and then minimise this by use of some suitable algorithm. The minimum value of $\chi^2(\vec{a})$ then defines the best-fit parameters $\vec{a}_{best}$.

The χ^2 function we use takes into account the fact that masses on different timeslices are correlated, possibly quite strongly. For the fit parameters $\vec{a} = (m, A)$ we define

$$\chi^2(\vec{a}) \equiv \sum_{t_i}\sum_{t_j} \delta C_H(t_i;\vec{a})\ \mathrm{Corr}^{-1}(t_i,t_j)\ \delta C_H(t_j;\vec{a}) \tag{4.73}$$

where we have defined

$$\delta C_H(t;\vec{a}) \equiv \frac{1}{\sigma_H(t_i)}\left[C_H(t_i) - C_{fit}(t_i;\vec{a})\right]. \tag{4.74}$$

Here $C_H(t)$ is our data point, the value of the hadron correlator at timeslice t. $C_{fit}(t;\vec{a})$ is the model value from Equation (4.69) or (4.70) and $\sigma_H(t)$ is the standard deviation of the configuration average of the correlator C_H, again at timeslice t.

$\mathrm{Corr}(t_i,t_j)$ is the *data correlation matrix* which measures the correlations between timeslices t_i and t_j. $\mathrm{Corr}(t_i,t_j)$ is defined in terms of the more usual *data covariance matrix*, $\mathrm{Cov}(t_i,t_j)$, which is the generalisation of the variance for a correlated data set. Corr is defined as

$$\mathrm{Corr}(t_i,t_j) \equiv \frac{\mathrm{Cov}(t_i,t_j)}{\sigma_H(t_i)\sigma_H(t_j)}. \tag{4.75}$$

where the data covariance matrix is

$$\mathrm{Cov}(t_i,t_j) \equiv \frac{1}{N_{cfg}(N_{cfg}-1)}\sum_{n=1}^{N_{cfg}}\left[C_H^{(n)}(t_i) - \langle C_H(t_i)\rangle\right]\left[C_H^{(n)}(t_j) - \left\langle C_H(t_j)\right\rangle\right]. \tag{4.76}$$

N_{cfg} is the number of configurations in the data set. $C_H^{(n)}(t)$ is the value of the correlator C_H at timeslice t on configuration n; $\langle C_H(t)\rangle$ is its average over all N_{cfg} configurations.

We use Corr rather than Cov in the definition of $\chi^2(\vec{a})$ since it yields a numerically better behaved matrix. By construction, Corr has 1's on the leading diagonal and numbers between 0 and 1 elsewhere; inverting such a matrix is numerically more stable than inverting Cov in which the elements can vary dramatically in size.

Throughout this chapter and the next I shall quote values of χ^2 as χ^2 per degree of freedom ($\chi^2/d.o.f.$), where the number of degrees of freedom is

$$(\text{Number of data points}) - (\text{Number of fit parameters}).$$

We consider a fit to be "good" when the $\chi^2/d.o.f.$ is $\mathcal{O}(1)$. A value much greater than 1 indicates either that the fit model does not match the data well with those parameters or that we have underestimated the errors on our data; a value much less than 1 indicates that we may be overestimating our errors or underestimating the correlations between timeslices.

4.1.3 Statistical errors

Except where explicitly stated otherwise, all quoted errors are purely statistical, deriving from the finite number of gauge configurations, N_{cfg}, used in the evaluation of the path integral. In addition, these errors are calculated almost exclusively according to the following *bootstrap* procedure:

1. create 1000 synthetic *bootstrap samples* such that each sample is determined by choosing randomly, with replacement, 60 configurations from our dataset;
2. for each bootstrap sample, perform all the mass fits and extrapolations as for the basic data;
3. obtain the errors on a given quantity from the 68% confidence limits of the corresponding bootstrap distribution.

For a good discussion of the bootstrap and other non-parametric statistical methods see, for example, reference [50].

The one exception to this prescription is the calculation of errorbars on effective mass plots; these are calculated using a single-elimination jackknife method.

4.1.4 Determination of t-fit ranges

To determine the time range over which to fit the hadron correlators, we adopted the following procedure:

1. using the effective mass plot, fix t_{max} to be as large as possible, consistent with the "perceived plateau";
2. choose t_{min} to be 3 or 4 timeslices less than t_{max};
3. fit the correlator over the range (t_{min}, t_{max}) and note the value of χ^2 per degree of freedom;
4. reduce t_{min} by 1;
5. return to step 3 and repeat until the value of χ^2 per degree of freedom shows a significant increase. By "significant" I mean a change in $\chi^2/d.o.f.$ of $\sim$1 for $t_{min} \rightarrow t_{min} - 1$.

Channel	κ values	t_{min}	t_{max}
P	all 6 combinations	14	22
V	5 lightest combinations	13	23
	(0.14144, 0.14144)	15	23
S	5 heaviest combinations	12	15
	(0.14262, 0.14262)	no signal	
A	all 6 combinations	11	14
T	all 6 combinations	9	12
N	all 3 combinations	16	22
$\Delta(\frac{3}{2})$	all 3 combinations	16	21
$\Delta(\frac{1}{2})$	all 3 combinations	10	13
$\tilde{N}$	all 3 combinations	13	16
$\tilde{\Delta}(\frac{3}{2})$	all 3 combinations	10	13
$\tilde{\Delta}(\frac{1}{2})$	2 heaviest combinations	10	13
	(0.14262, 0.14262)	no signal	

Table 4.1: Best fit ranges for different meson and baryon channels and different combinations of κ values. Baryon operators with a tilde ($\tilde{}$) indicate the parity-partner state.

Using this procedure we fit as many timeslices as possible as far out as possible, in the hope of reducing contamination from excited states. The reasoning here follows that of reference [20]. The fitting ranges so decided are shown in Table 4.1. In Figures 4.1 to 4.3 I present the effective mass plots for the pseudoscalar, vector, nucleon and $\Delta(\frac{3}{2})$ channels at the three degenerate (κ_1, κ_2) values, (0.14144, 0.14144), (0.14226, 0.14226) and (0.14262, 0.14262).

The signals for these four channels are relatively clean and I have confidence, modulo the caveats of §(4.2), that the chosen fit ranges correspond to the ground-state signal. Unfortunately, this is not the case for the $S(0^{++})$, $A(1^{+-})$, $T(1^{++})$, $\Delta(\frac{1}{2})$ and baryon parity-partner channels. The signals here are poor, the effective mass plots being very noisy. There is, however, some evidence of plateau behaviour for some of these operators and I show, in Figures 4.4 and 4.5, the effective masses for the heaviest (0.14144, 0.14144) combination. I have only limited confidence that the fit-ranges quoted in Table 4.1 correspond to a ground-state signal for

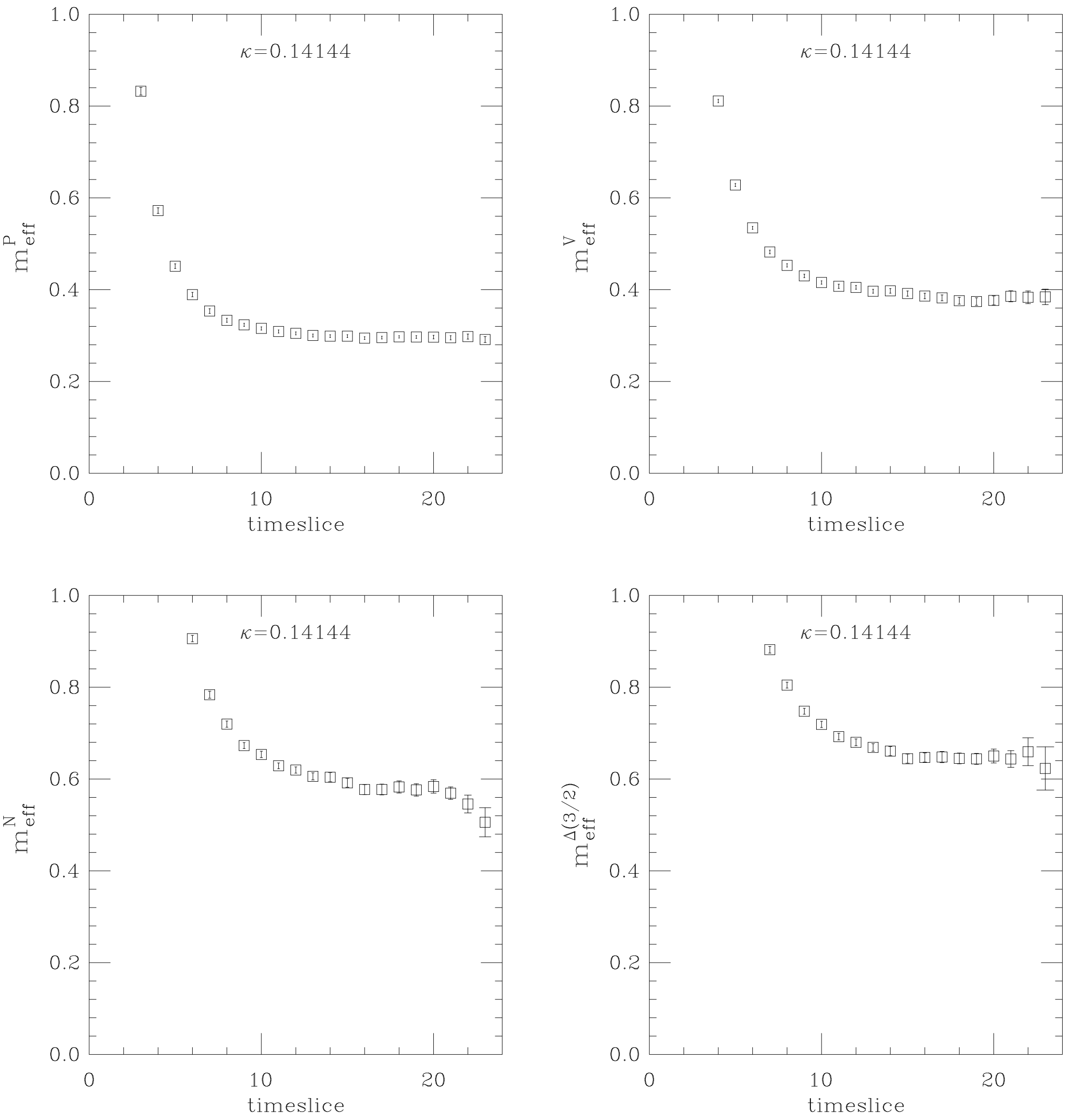

Figure 4.1: Effective masses of the pseudoscalar and vector mesons and the nucleon and $\Delta(\frac{3}{2})$ baryons calculated with degenerate quark propagators at $\kappa = 0.14144$.

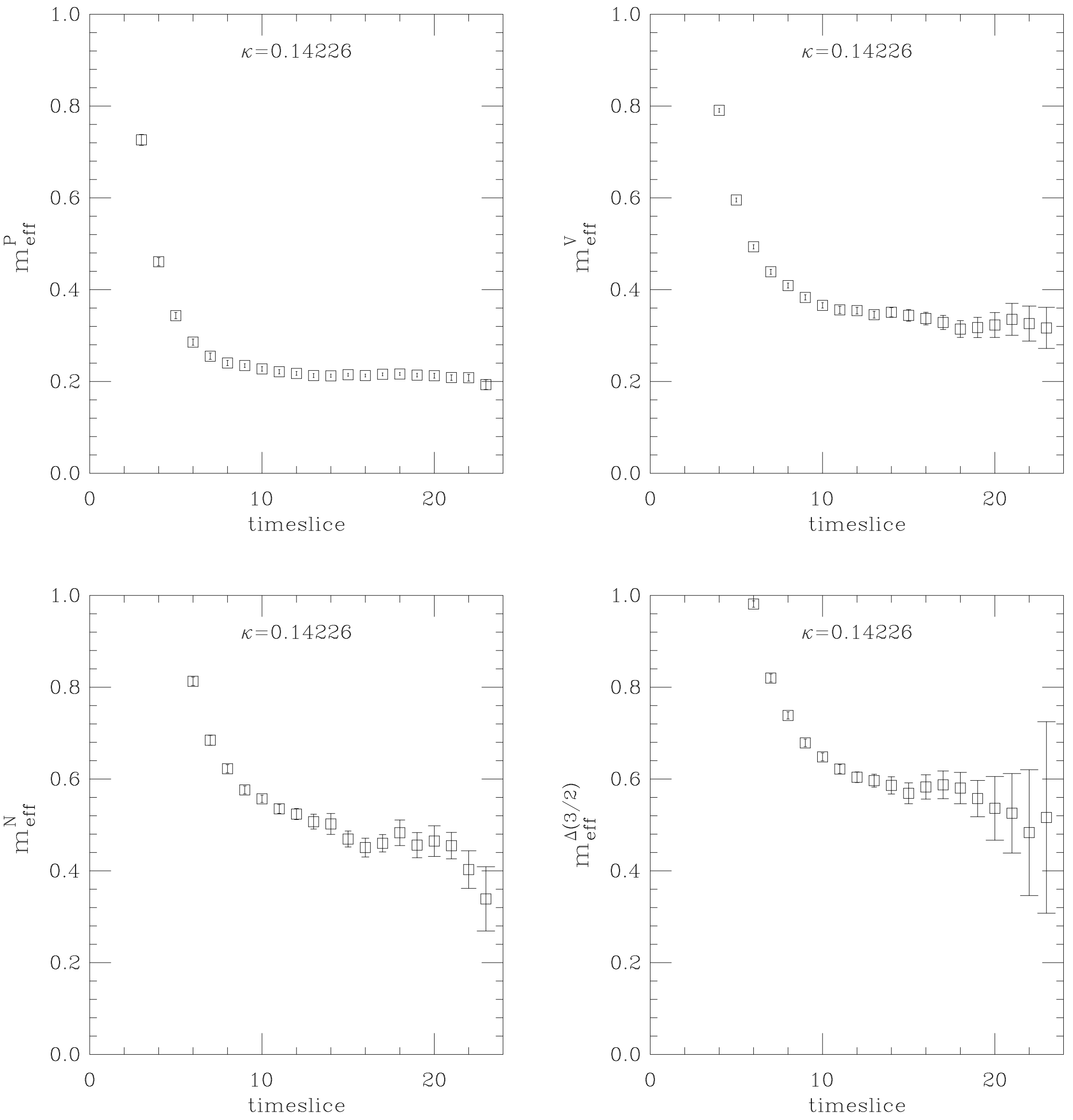

Figure 4.2: Effective masses of the pseudoscalar and vector mesons and the nucleon and $\Delta(\frac{3}{2})$ baryons calculated with degenerate quark propagators at $\kappa = 0.14226$.

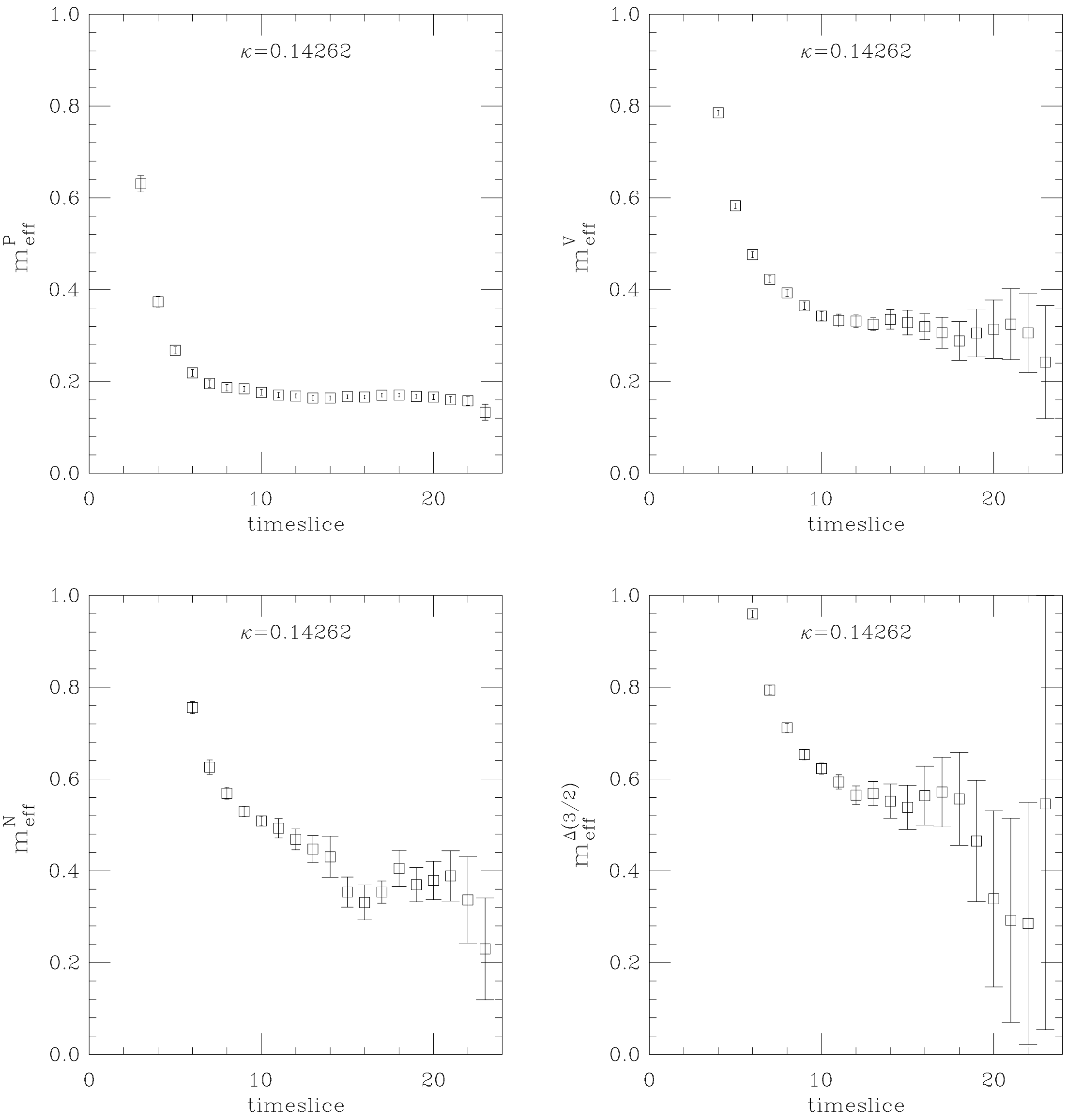

Figure 4.3: Effective masses of the pseudoscalar and vector mesons and the nucleon and $\Delta(\frac{3}{2})$ baryons calculated with degenerate quark propagators at $\kappa = 0.14262$.

these channels.

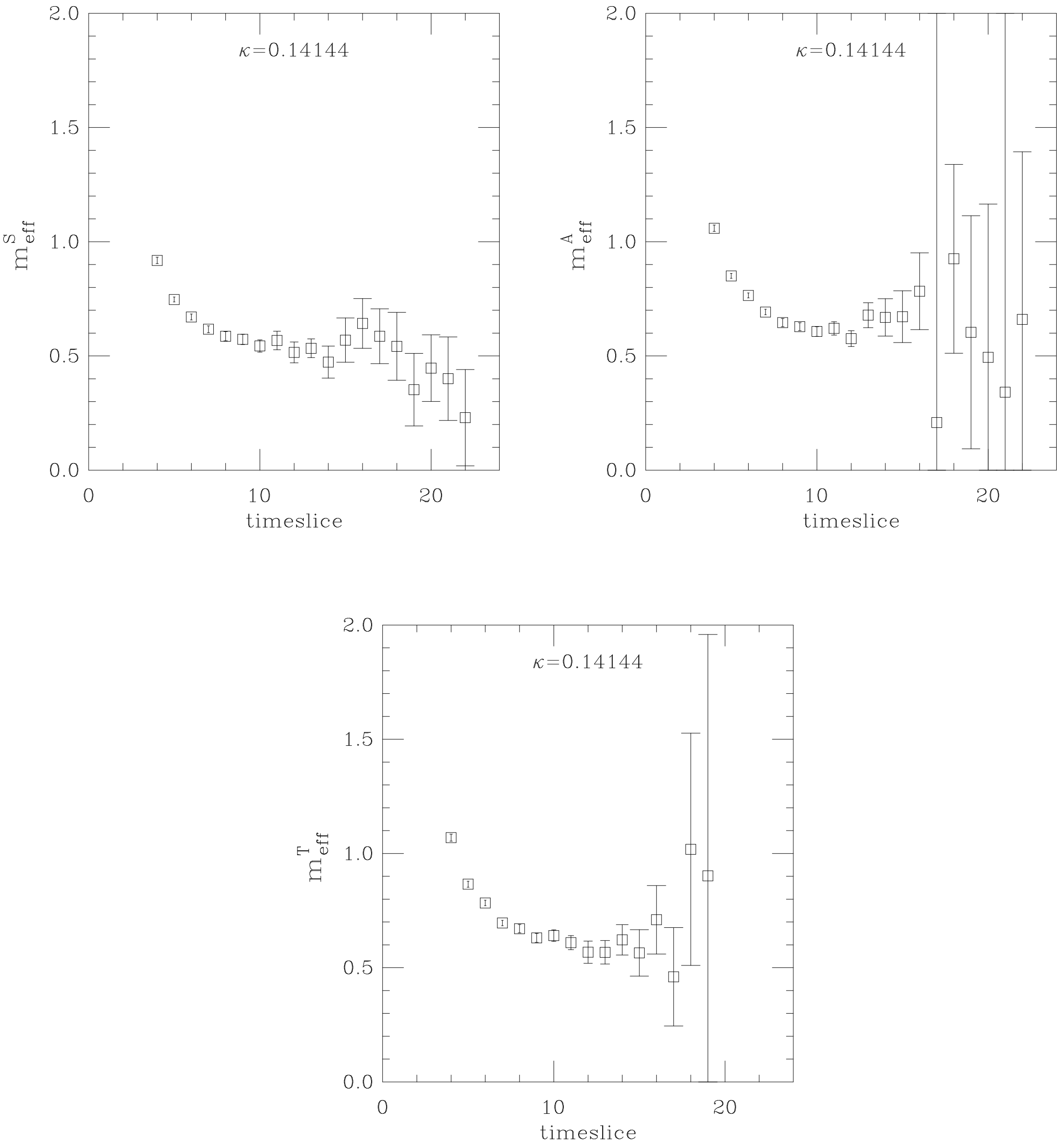

Figure 4.4: Effective masses of the $S(0^{++})$, $A(1^{+-})$ and $T(1^{++})$ mesons calculated with degenerate quark propagators at $\kappa = 0.14144$.

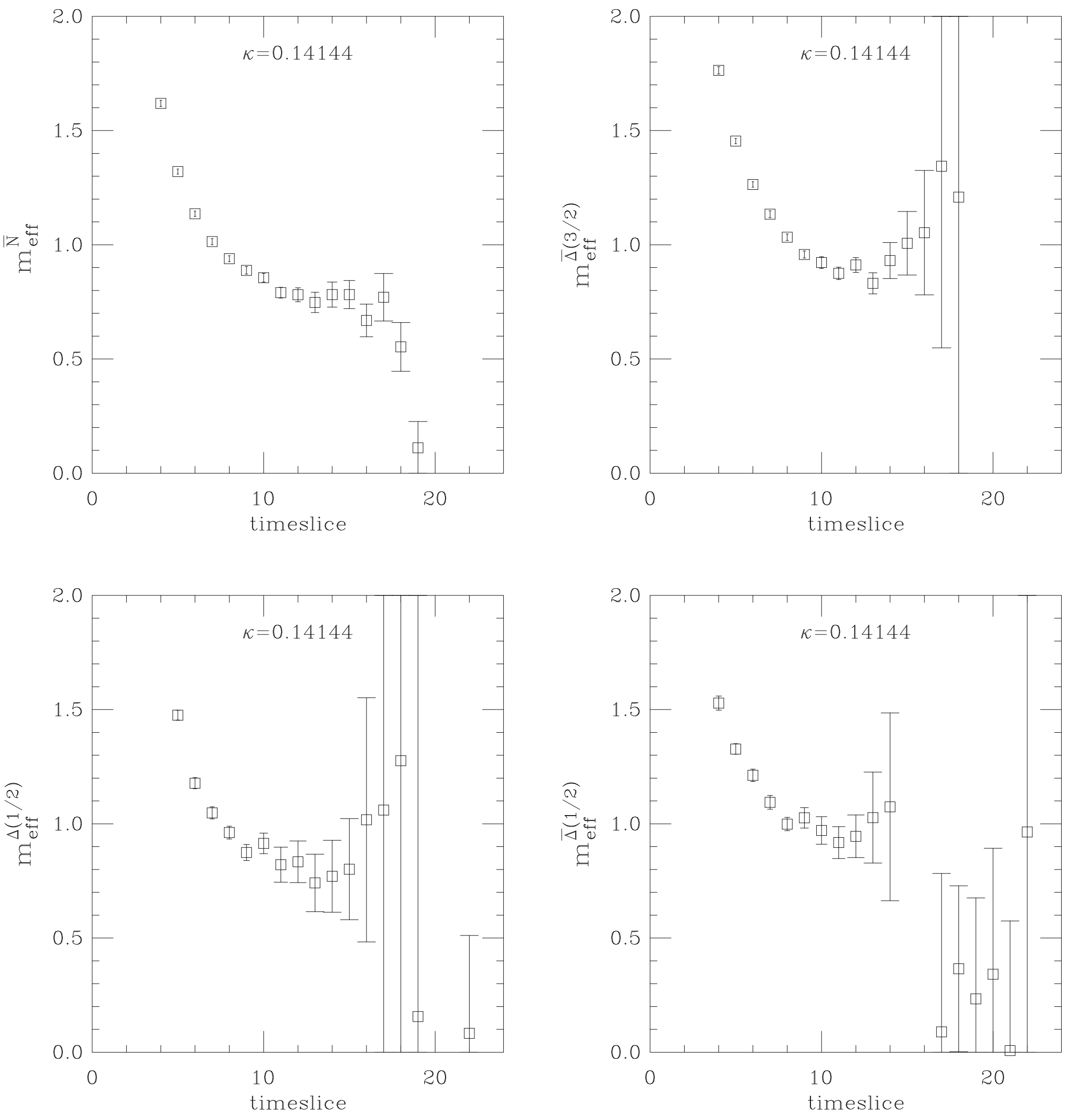

Figure 4.5: Effective masses of the $\tilde{N}$, $\tilde{\Delta}(\frac{3}{2})$, $\Delta(\frac{1}{2})$ and $\tilde{\Delta}(\frac{1}{2})$ baryons calculated with degenerate quark propagators at $\kappa = 0.14144$.

4.2 Examination of Systematic Errors

In this section I shall attempt to quantify the systematic errors arising from the possible incorrect identification of plateaux in the effective mass functions. Figure 4.6 shows the fit stability plot and the plot of $\chi^2/d.o.f.$ vs. t_{min} used in the determination of the fit ranges for the pseudoscalar and vector mesons, as per §(4.1.4). This figure shows the effect of decreasing t_{min} from 20 to 11 on both the value of the fit mass and the corresponding $\chi^2/d.o.f.$ t_{max} was fixed at 22 for the pseudoscalar and 23 for the vector, these values decided from the effective mass plots of Figures 4.1 to 4.3.

The pseudoscalar mass for all three degenerate κ combinations is very stable, barring the two glitches in the lightest κ for $t_{min} = 12$ and $t_{min} = 16$. The data at these timeslices show no irregularities and we ascribe the wayward masses to failures in the fitting algorithm. The value of $t_{min} = 14$ in Table 4.1 was chosen from the χ^2 plot; 13 lies on the edge of the "allowable χ^2" region, and so 14 was chosen, as it were, for safety.

There is a problem in the stability of the vector. From the χ^2 plot, any t_{min} from 13 onwards is acceptable, but the fit mass, especially for the heaviest κ value, shows a steady fall from $t_{min} = 14$ to $t_{min} = 18$. In addition, there is a stable region for t_{min} between 11 and 14 which suggests that the plateaux may lie there. However, looking at the effective mass plots we are drawn to conclude that, in the terminology of reference [20], there is a *pre-plateau* at timeslices 10–12 and the ground state signal lies further out.

For the lighter two κ's, the falloff is masked by larger error bars and the fit range 13–23 yields masses which are stable within these errors. The problem is most pronounced for the heaviest κ value since the errors here are much smaller. In Table 4.2 I attempt to quantify this behaviour, noting the highest and lowest masses obtained from the six fits corresponding to the ranges 13–23 to 18–23, compared to the masses in the mid-range of 15–23. The asymmetry in the resulting "systematic error" is an indication of the monotonic decrease in the fit masses. I note that the range of the systematic error for the heaviest-mass correlator is only $1\frac{1}{2}$ times the statistical error range, and conclude that the fit range 15–23 is a good compromise for this κ value.

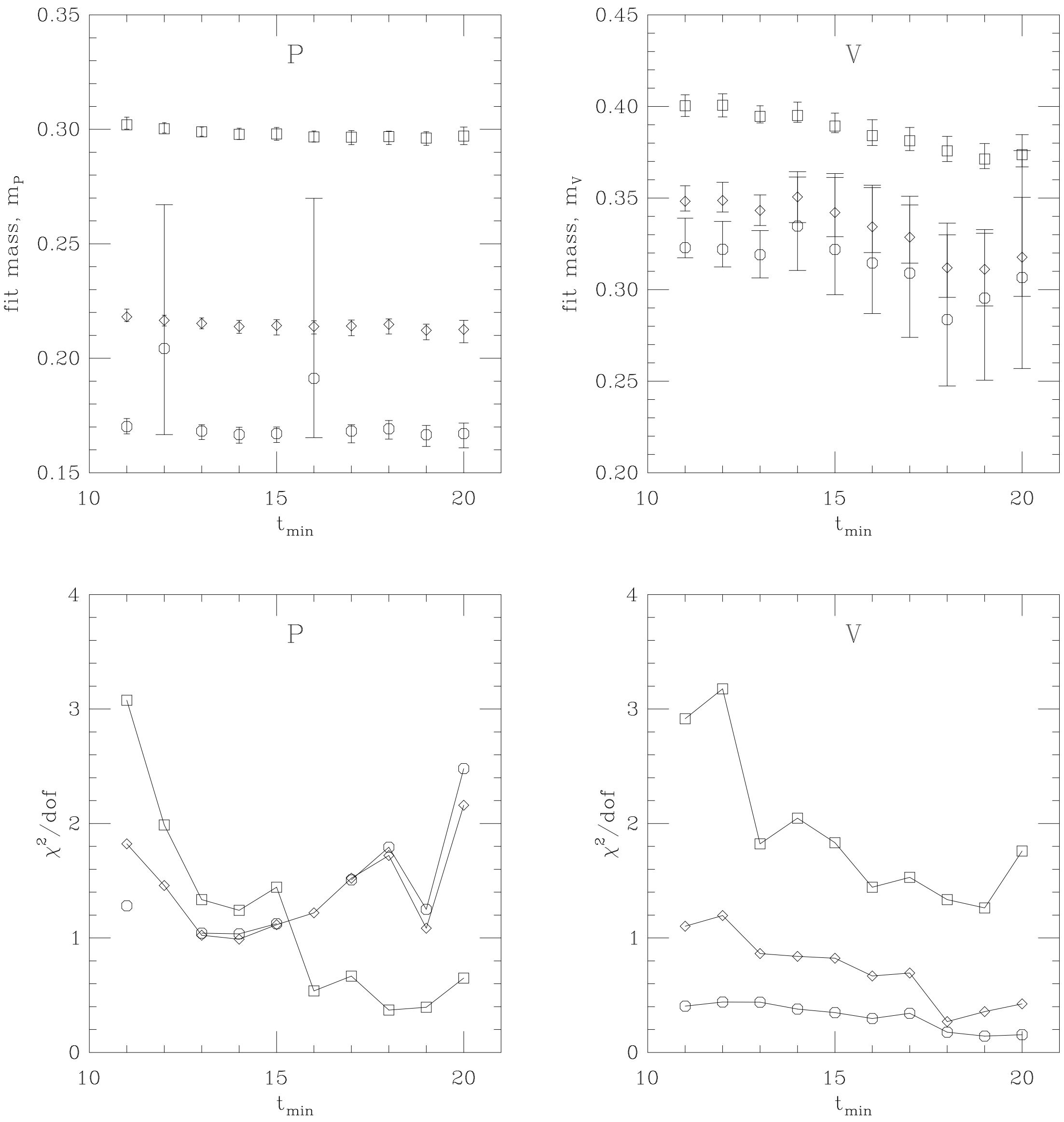

Figure 4.6: Stability of mass fit with changing t_{min} and corresponding plots of $\chi^2/d.o.f.$ for the pseudoscalar and vector mesons. t_{max} is fixed at 22 for the P and 23 for the V. The different symbols represent different (degenerate) κ values: 0.14144 (□), 0.14226 (◇) and 0.14262 (○).

κ	m_V^{high}	m_V^{low}	m_V	error	
				statistical	systematic
0.14144	0.395	0.376	0.389	$+0.007-0.006$	$+0.006-0.013$
0.14226	0.351	0.312	0.343	$+0.009-0.007$	$+0.008-0.031$
0.14262	0.335	0.284	0.319	$+0.014-0.013$	$+0.016-0.035$

Table 4.2: Highest and lowest fit masses for the vector meson with degenerate quarks, based on an analysis of the fit regions 13–23 to 18–23. We take the difference between the highest (lowest) mass and the best-fit mass as a measure of the systematic error.

κ	m_N^{high}	m_N^{low}	m_N	error	
				statistical	systematic
0.14144	0.573	0.568	0.573	$+0.015-0.007$	$+0.000-0.005$
0.14226	0.475	0.452	0.462	$+0.020-0.014$	$+0.013-0.010$
0.14262	0.392	0.372	0.372	$+0.024-0.016$	$+0.020-0.000$

Table 4.3: Highest and lowest fit masses for the nucleon, based on an analysis of the fit regions 16–22 to 19–22 for the heaviest and 14–22 to 19–22 for the others. We take the difference between the highest (lowest) mass and the best-fit mass as a measure of the systematic error.

Figure 4.7 shows the equivalent data for the "clean" baryons, the nucleon and $\Delta(\frac{3}{2})$. For the nucleon, the plots indicate stable plateaux for the lightest two κ's beginning at a t_{min} of 14. However, the large asymmetry between the upper and lower error bars at $t_{min} = 14$ and 15 is a possible indication that the bootstrap sampling is still sensitive to excited states at this timeslice, and I adopt the fit range 16–22 for all κ values. Table 4.3 quantifies the possible systematic errors due to variation of the fit range for the nucleon. Here, the systematic error is, in every case, smaller than the corresponding statistical error, promoting confidence in the chosen fit range.

The graphs for the $\Delta(\frac{3}{2})$ point unequivocally to $t_{min} = 15$ as the beginning of the stable region, though for the lightest κ the mass fit is rather low at this point. 16–21 proves to be the optimal range, yielding results that are stable, within

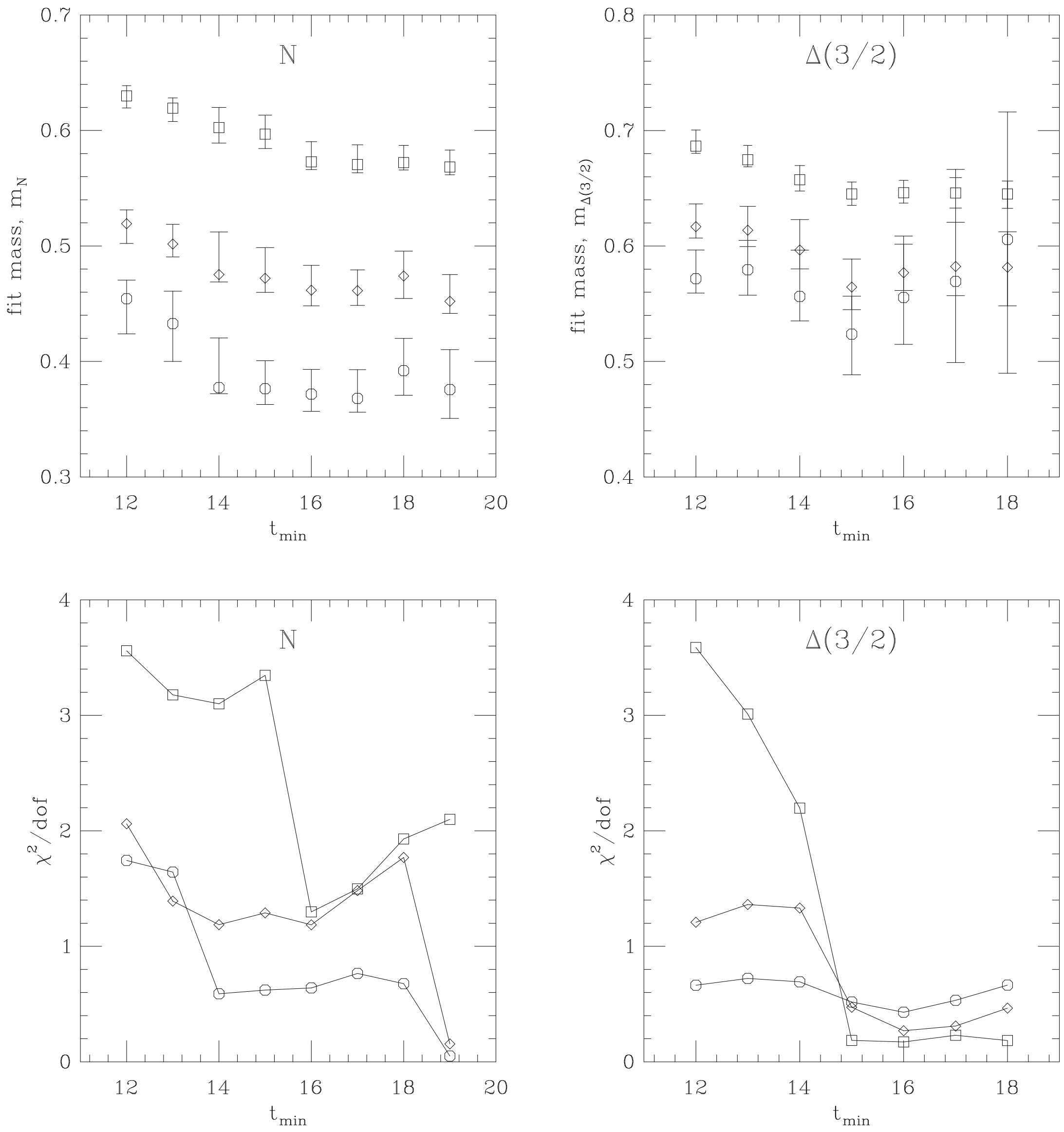

Figure 4.7: Stability of mass fit with changing t_{min} and corresponding plots of $\chi^2/d.o.f.$ for the nucleon and $\Delta(\frac{3}{2})$ baryons. t_{max} is fixed at 22 for the nucleon and 21 for the $\Delta(\frac{3}{2})$. The different symbols represent different κ values: 0.14144 ($\square$), 0.14226 ($\diamond$) and 0.14262 ($\circ$).

errors, to a change of ± 1 or 2 timeslices in t_{min}.

Generally, errors deriving from uncertainties in choosing the fitting region for the ground state are hard to quantify. Most often these effects are masked by the statistical errors and the problem is avoided. In our case, this effect does make an appearance in the heaviest vector channel where we find it difficult to define an unambiguous plateau. The size of the resulting uncertainty is comparable with the statistical error, and one possible way of accounting for it would be to double the errorbars on the heaviest point. It provides a lesson, certainly, in the necessity of not underestimating one's errors.

4.3 Spectrum Data in Lattice Units

In Tables 4.4 and 4.5 I present the masses of various meson channels, plus decay constants for the pseudoscalar and vector mesons, along with the calculated value of the hyperfine splitting $m_V^2 - m_P^2$. Notice that the lattice values of the meson decay constants include factors of the renormalisation constants Z_A and Z_V; these must be factored out before we can compare lattice results with experiment.

The $\chi^2/d.o.f.$ for the mesons are all satisfactory, ranging from 0.1–2.3. The largest value here comes from the lamentably poor scalar channel; excluding this, our $\chi^2/d.o.f.$ range over 0.1–1.9. The very low values for the $A(1^{+-})$ and $T(1^{++})$ are symptomatic of the large errors appearing in the effective mass plots of Figure 4.4, *not* evidence of exceptionally good fits.

Table 4.6 contains the fit-masses for the baryon channels. The values of $\chi^2/d.o.f.$ range over 0.2–2.8, with the larger values again the product of one channel, the $\tilde{\Delta}(\frac{3}{2})$; excluding this, we have a $\chi^2/d.o.f.$ range of 0.2–1.3. In Figure 4.8 I show the lattice data for the three degenerate κ combinations on an Edinburgh plot. The solid line is a phenomenological curve derived from the quark model using a simple spin-spin interaction [51]. The lack of coincidence between the curve and the data is somewhat disappointing; for reasons we must look again at the effective mass plots of Figures 4.1 to 4.3.

It is noticeable, particularly at the lightest κ value, 0.14262, that there is a “dip” in the effective mass at timeslices 15, 16 and 17. The sudden drop between

	degenerate		
κ_1	0.14144	0.14226	0.14262
κ_2	0.14144	0.14226	0.14262
m_P	$0.298\,^{+2}_{-2}$	$0.214\,^{+2}_{-3}$	$0.167\,^{+3}_{-4}$
$\chi^2/d.o.f.$	8.7/7	6.9/7	7.2/7
m_V	$0.389\,^{+7}_{-6}$	$0.343\,^{+9}_{-7}$	$0.319\,^{+14}_{-13}$
$\chi^2/d.o.f.$	13/7	7.8/9	4.0/9
$m_V^2 - m_P^2$	$0.063\,^{+5}_{-4}$	$0.072\,^{+6}_{-5}$	$0.074\,^{+9}_{-8}$
m_S	$0.51\,^{+2}_{-2}$	$0.48\,^{+8}_{-6}$	no signal
$\chi^2/d.o.f.$	4.7/2	4.6/2	-
m_A	$0.61\,^{+2}_{-1}$	$0.57\,^{+3}_{-2}$	$0.56\,^{+4}_{-3}$
$\chi^2/d.o.f.$	0.2/2	0.9/2	0.6/2
m_T	$0.58\,^{+3}_{-3}$	$0.47\,^{+5}_{-4}$	$0.36\,^{+9}_{-7}$
$\chi^2/d.o.f.$	0.6/2	2.2/2	0.8/2
f_P/Z_A	$0.0624\,^{+7}_{-13}$	$0.0512\,^{+6}_{-15}$	$0.0452\,^{+8}_{-21}$
$\chi^2/d.o.f.$	8.3/8	9.2/8	12/8
$1/(f_V Z_V)$	$0.314\,^{+8}_{-7}$	$0.345\,^{+8}_{-9}$	$0.356\,^{+9}_{-17}$
$\chi^2/d.o.f.$	13/7	7.8/9	4.0/9

Table 4.4: Masses and decay constants, in lattice units, of mesons composed of degenerate quarks.

	non-degenerate		
κ_1	0.14144	0.14262	0.14226
κ_2	0.14226	0.14144	0.14262
m_P	$0.259\ ^{+2}_{-2}$	$0.241\ ^{+2}_{-3}$	$0.192\ ^{+3}_{-3}$
$\chi^2/d.o.f.$	6.3/7	5.3/7	6.9/7
m_V	$0.370\ ^{+6}_{-5}$	$0.360\ ^{+8}_{-6}$	$0.331\ ^{+11}_{-10}$
$\chi^2/d.o.f.$	12/9	9.1/9	5.4/9
$m_V^2 - m_P^2$	$0.070\ ^{+5}_{-3}$	$0.071\ ^{+6}_{-4}$	$0.073\ ^{+7}_{-6}$
m_S	$0.49\ ^{+4}_{-3}$	$0.51\ ^{+7}_{-4}$	$0.52\ ^{+27}_{-10}$
$\chi^2/d.o.f.$	4.2/2	4.8/2	5.7/2
m_A	$0.59\ ^{+2}_{-2}$	$0.59\ ^{+3}_{-2}$	$0.56\ ^{+4}_{-2}$
$\chi^2/d.o.f.$	0.5/2	0.8/2	0.8/2
m_T	$0.54\ ^{+4}_{-4}$	$0.52\ ^{+5}_{-4}$	$0.43\ ^{+6}_{-5}$
$\chi^2/d.o.f.$	1.8/2	2.0/2	1.4/2
f_P/Z_A	$0.0567\ ^{+7}_{-13}$	$0.0539\ ^{+6}_{-15}$	$0.0482\ ^{+7}_{-17}$
$\chi^2/d.o.f.$	11/8	9.2/8	8.1/8
$1/(f_V Z_V)$	$0.332\ ^{+6}_{-7}$	$0.336\ ^{+8}_{-9}$	$0.350\ ^{+9}_{-12}$
$\chi^2/d.o.f.$	12/9	9.1/9	5.4/9

Table 4.5: Masses and decay constants, in lattice units, of mesons composed of non-degenerate quarks.

	degenerate		
κ_1	0.14144	0.14226	0.14262
κ_2	0.14144	0.14226	0.14262
m_N	$0.57\,^{+2}_{-1}$	$0.46\,^{+2}_{-1}$	$0.37\,^{+2}_{-2}$
$\chi^2/d.o.f.$	6.5/5	5.9/5	3.2/5
$m_{\Delta(\frac{3}{2})}$	$0.65\,^{+1}_{-1}$	$0.58\,^{+3}_{-2}$	$0.56\,^{+7}_{-5}$
$\chi^2/d.o.f.$	0.7/4	1.1/4	1.7/4
$m_{\Delta(\frac{1}{2})}$	$0.94\,^{+4}_{-5}$	$0.90\,^{+9}_{-9}$	$0.90\,^{+16}_{-21}$
$\chi^2/d.o.f.$	2.2/2	0.4/2	1.3/2
$m_{\tilde{N}}$	$0.76\,^{+4}_{-3}$	$0.59\,^{+10}_{-6}$	$0.40\,^{+12}_{-6}$
$\chi^2/d.o.f.$	1.2/2	0.4/2	0.3/2
$m_{\tilde{\Delta}(\frac{3}{2})}$	$0.91\,^{+3}_{-2}$	$0.86\,^{+5}_{-3}$	$0.86\,^{+7}_{-6}$
$\chi^2/d.o.f.$	5.4/2	4.1/2	5.6/2
$m_{\tilde{\Delta}(\frac{1}{2})}$	$0.95\,^{+6}_{-4}$	$0.87\,^{+8}_{-9}$	no signal
$\chi^2/d.o.f.$	0.5/2	2.7/2	-

Table 4.6: Masses and decay constants, in lattice units, of baryons composed of degenerate quarks.

timeslices 14 and 15 and the sharp rise between 17 and 18 hint that this may be a purely statistical fluctuation, the result of some long-lived feature in the gauge fields. That it occurs at the beginning of our chosen fit range is unfortunate; as a result the lighter two nucleon masses may be *too* light. If we move the fit range out past the dip and fit the nucleon masses over 18–22 ($\chi^2/d.o.f.\sim 2$) we get upwards shifts of 1σ for $\kappa = 0.14262$, $\frac{1}{2}\sigma$ for $\kappa = 0.14226$ and 0 for $\kappa = 0.14144$. The effect on the Edinburgh plot is to move the middle point to within 1σ of the quark model curve and the lightest point to within $1\frac{1}{2}\sigma$.

This problem with the lightest nucleon mass also affects the chiral extrapolation — see §(4.5).

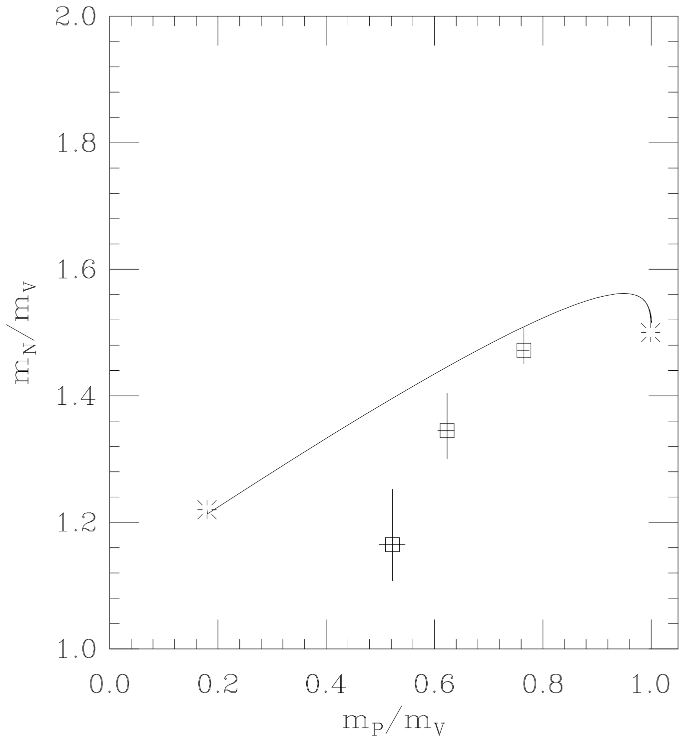

Figure 4.8: Edinburgh plot for degenerate data. The curve is a phenomenological quark model prediction [51].

4.4 Quark Mass Dependence

Our use of non-degenerate quark propagators in the calculation of meson correlators means that our meson masses depend on not one but two quark masses, as defined by Equation (1.10). In most previous calculations (see, for example, references [18, 26, 52, 53]) it has been assumed that the pseudoscalar meson mass obeys the PCAC relation (cf. Equation (2.37))

$$m_P^2(\kappa_1, \kappa_2) = b_P \left(\frac{1}{2\kappa_1} + \frac{1}{2\kappa_2} - \frac{1}{2\kappa_{crit}} \right), \tag{4.77}$$

and that the vector meson mass obeys

$$m_V(\kappa_1, \kappa_2) = a_V + b_V \left(\frac{1}{2\kappa_1} + \frac{1}{2\kappa_2} - \frac{1}{2\kappa_{crit}} \right), \tag{4.78}$$

i.e., that the mass of a meson made from quarks of different masses m_1 and m_2 is exactly the same as one composed of identical quarks of mass $\frac{1}{2}(m_1 + m_2)$. One of the aims of this section is the testing of this assumption.

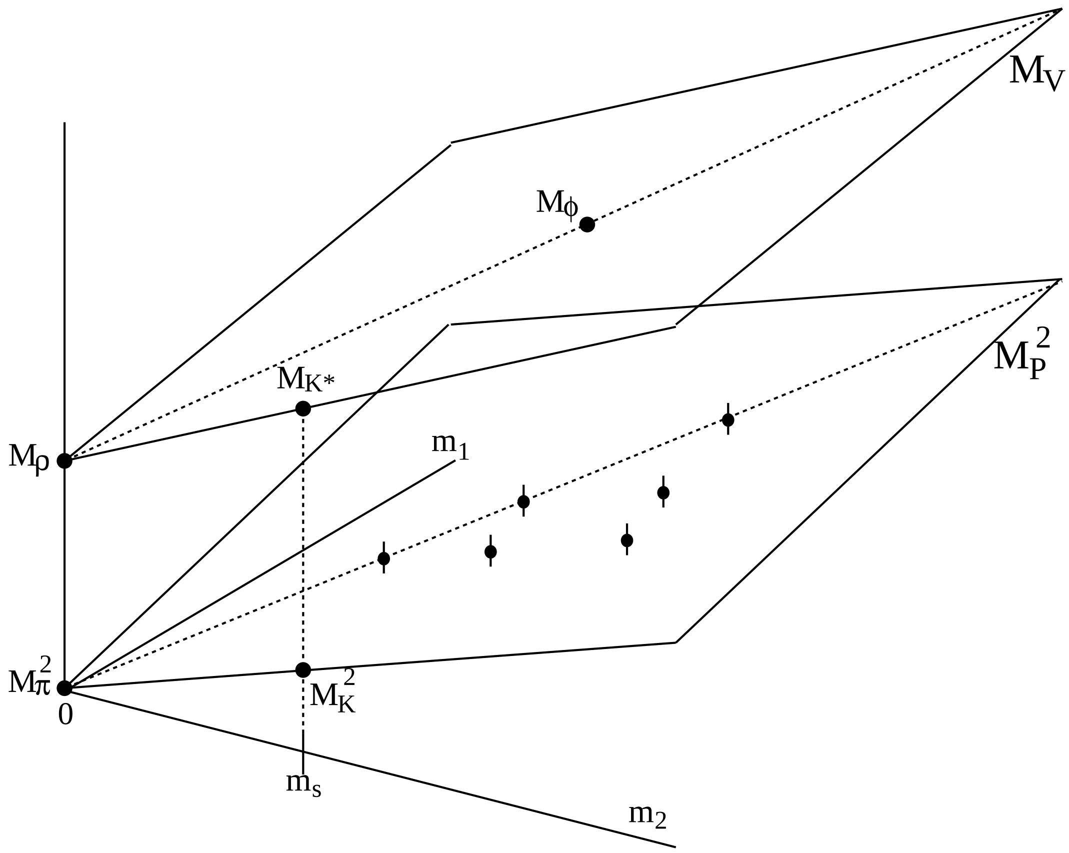

Figure 4.9: Schematic of the fit planes defined by Equation (4.79).

For all the calculated meson masses and decay constants I fit the values for all six κ combinations to the functional form

$$a_1 + \frac{a_2}{2}(m_2 + m_1) + \frac{a_3}{2}|m_2 - m_1|. \tag{4.79}$$

Allowing a_3 to vary as a free parameter in the fit enables us to test the assumption in Equations (4.77) and (4.78) that there is no dependence on the difference of the quark masses. Equation (4.79) defines a plane through the six data points, as shown in Figure 4.9. This figure is the two-quark mass generalisation of the usual chiral extrapolation plot. The diagonals at $m_1 = m_2$ correspond to the normal line of extrapolation to zero quark mass.

In Table 4.7 I present the values of the fit parameters $a_1 \dots a_3$ for various meson masses, decay constants and ratios. In the table, (A) refers to a fit with a_3, the coefficient of $|m_2 - m_1|$, unconstrained and (B) to a fit with a_3 fixed to zero. The $\chi^2/d.o.f.$ are all reasonable, though generally slightly larger for fit (B). For fit (A),

	fit (A) parameters			
	a_1	a_2	a_3	$\chi^2/d.o.f.$
m_P^2	0.0	$2.12\,^{+4}_{-3}$	$-0.01\,^{+1}_{-1}$	4.3/3
m_V	$0.29\,^{+2}_{-1}$	$2.3\,^{+4}_{-3}$	$0.1\,^{+1}_{-1}$	1.9/3
f_P/Z_A	$0.041\,^{+1}_{-2}$	$0.53\,^{+3}_{-2}$	$-0.01\,^{+1}_{-1}$	4.8/3
$1/(f_V Z_V)$	$0.38\,^{+1}_{-2}$	$-1.4\,^{+4}_{-2}$	$0.0\,^{+1}_{-1}$	1.2/3
$f_P/(m_V Z_A)$	$0.142\,^{+6}_{-9}$	$0.5\,^{+2}_{-2}$	$-0.10\,^{+6}_{-7}$	3.1/3
m_S	$0.38\,^{+4}_{-9}$	$3.2\,^{+20}_{-8}$	$0.6\,^{+7}_{-6}$	1.7/2
m_A	$0.53\,^{+4}_{-3}$	$2.0\,^{+5}_{-7}$	$0.0\,^{+1}_{-1}$	3.5/3
m_T	$0.34\,^{+5}_{-6}$	$5.7\,^{+12}_{-11}$	$1.0\,^{+4}_{-4}$	2.5/3

	fit (B) parameters			
	a_1	a_2	a_3	χ^2/dof
m_P^2	0.0	$2.12\,^{+4}_{-3}$	0.0	9.5/4
m_V	$0.29\,^{+1}_{-1}$	$2.5\,^{+3}_{-3}$	0.0	2.5/4
f_P/Z_A	$0.040\,^{+1}_{-2}$	$0.53\,^{+3}_{-2}$	0.0	7.1/4
$1/(f_V Z_V)$	$0.38\,^{+1}_{-2}$	$-1.4\,^{+3}_{-2}$	0.0	1.3/4
$f_P/(m_V Z_A)$	$0.142\,^{+6}_{-9}$	$0.4\,^{+2}_{-2}$	0.0	5.6/4
m_S	$0.40\,^{+6}_{-8}$	$2.6\,^{+16}_{-10}$	0.0	2.3/3
m_A	$0.53\,^{+4}_{-3}$	$2.0\,^{+4}_{-6}$	0.0	3.7/4
m_T	$0.35\,^{+5}_{-6}$	$4.8\,^{+9}_{-10}$	0.0	6.9/4

Table 4.7: Fit parameters for masses, decay constants and ratios, using the fit form described in Equation (4.79), (A) with a_3 unconstrained, and (B) with $a_3 = 0$.

	fit (B) parameters		$\chi^2/d.o.f.$
	a_1	a_2	
m_N	$0.31\,^{+3}_{-2}$	$6.2\,^{+6}_{-6}$	5.1/1
$m_{\Delta(\frac{3}{2})}$	$0.50\,^{+4}_{-3}$	$3.7\,^{+7}_{-9}$	0.1/1
$m_{\Delta(\frac{1}{2})}$	$0.84\,^{+13}_{-13}$	$2.3\,^{+23}_{-23}$	0.03/1
$m_{\tilde{N}}$	$0.32\,^{+17}_{-7}$	$10\,^{+2}_{-4}$	1.6/1
$m_{\tilde{\Delta}(\frac{3}{2})}$	$0.78\,^{+6}_{-6}$	$3.2\,^{+10}_{-10}$	0.5/1
$m_{\tilde{\Delta}(\frac{1}{2})}$	$0.77\,^{+12}_{-13}$	$4.5\,^{+23}_{-23}$	0/0

Table 4.8: Fit (B) parameters for the baryons.

in all cases the coefficient a_3 is zero to within, at most, $2\frac{1}{2}$ standard deviations; comparing the two fits we see that the values of a_1 and a_2 are perfectly consistent within errors. Thus, we have numerical evidence that these physical quantities depend only on the sum of the quark masses; we see no statistically significant dependence on $|m_2 - m_1|$. Given this, and the fact that there is no theoretical basis for $a_3 \neq 0$, I shall quote results from hereon based solely on fit (B).

For the baryon data we have no non-degenerate points; thus we are only able to perform fit (B), corresponding to the usual linear behaviour for the baryon masses:

$$m_B(\kappa) = a_1 + a_2 \left(\frac{1}{2\kappa} - \frac{1}{2\kappa_{crit}} \right). \tag{4.80}$$

Table 4.8 lists the fit parameters for the various baryon channels. Note that for the $\tilde{\Delta}(\frac{1}{2})$ we only have mass estimates for the heavier two κ values, and hence our linear fit is to two points only.

4.5 Chiral Extrapolations

Following on from the previous section, I look at the chiral behaviour of the various hadron channels as $m \to 0$. The first task is to extract κ_{crit}, the value of κ at which the quark mass vanishes. To do this I fit the six estimates of the pseudoscalar meson mass from the six κ combinations to the form in Equation (4.79) with $a_1 = a_3 = 0$. The fit uses a correlated χ^2 function similar to the one defined in Equation (4.73), with a correlation matrix reconstructed from the bootstrap distributions of the six m_P fits.

Performing this correlated extrapolation in both κ's to $m_P^2(\kappa_{crit}, \kappa_{crit}) = 0$ gives

$$\kappa_{crit} = 0.14315 \,{}^{+2}_{-2}. \tag{4.81}$$

Figure 4.10 shows the corresponding plot of m_P^2 vs. $1/2\kappa_{eff}$ where I define

$$\frac{1}{\kappa_{eff}} \equiv \frac{1}{2}\left(\frac{1}{\kappa_1} + \frac{1}{\kappa_2}\right), \tag{4.82}$$

in keeping with $a_3 = 0$. The fact that the degenerate and non-degenerate points lie very close to the fit line is again evidence that m_P^2 depends only on $m_1 + m_2$.

Figure 4.10 also shows the extrapolation of the vector mass m_V; again, good agreement between the degenerate and non-degenerate data lends graphical support to our choice $a_3 = 0$. In addition, the clear linear behaviour in the extrapolation of the pseudovector mass, m_A, is very encouraging, although the errors are large.

The mass estimates for the scalar meson (lower-right, Figure 4.10) show very little functional dependence on the quark mass, a sign of the poor signals for this channel (witness the absence of the lightest degenerate point). To emphasise this, The dotted line shows an *uncorrelated* fit to the five points. However, the *correlated* extrapolation (solid line) shows a distinct slope and we may be able to lend some credence to the chiral result, although the errors in the fit parameters (Table 4.7) are appropriately large.

Although not presented here, the plot for the $T(1^{++})$ channel shows a distinct negative curvature towards the three lightest quark masses, though the fit is still linear within errors. The likely conclusion is that we really do not have a signal for this channel.

As hinted in §(4.3), the chiral extrapolation of the nucleon mass data, Figure 4.11, highlights the problem of the lightest κ point. Here we only have the three degenerate κ combinations, and the mass at (0.14262, 0.14262) lends a distinct curvature to the plot. Such a negative curvature has been observed before (see, for example, references [54, 55]), and recent results in chiral perturbation theory [56] hint that the nucleon mass may go like $\sqrt{m}$. Indeed, if we fit the *square* of the nucleon mass to a linear form we get a better fit, indicated by an improved

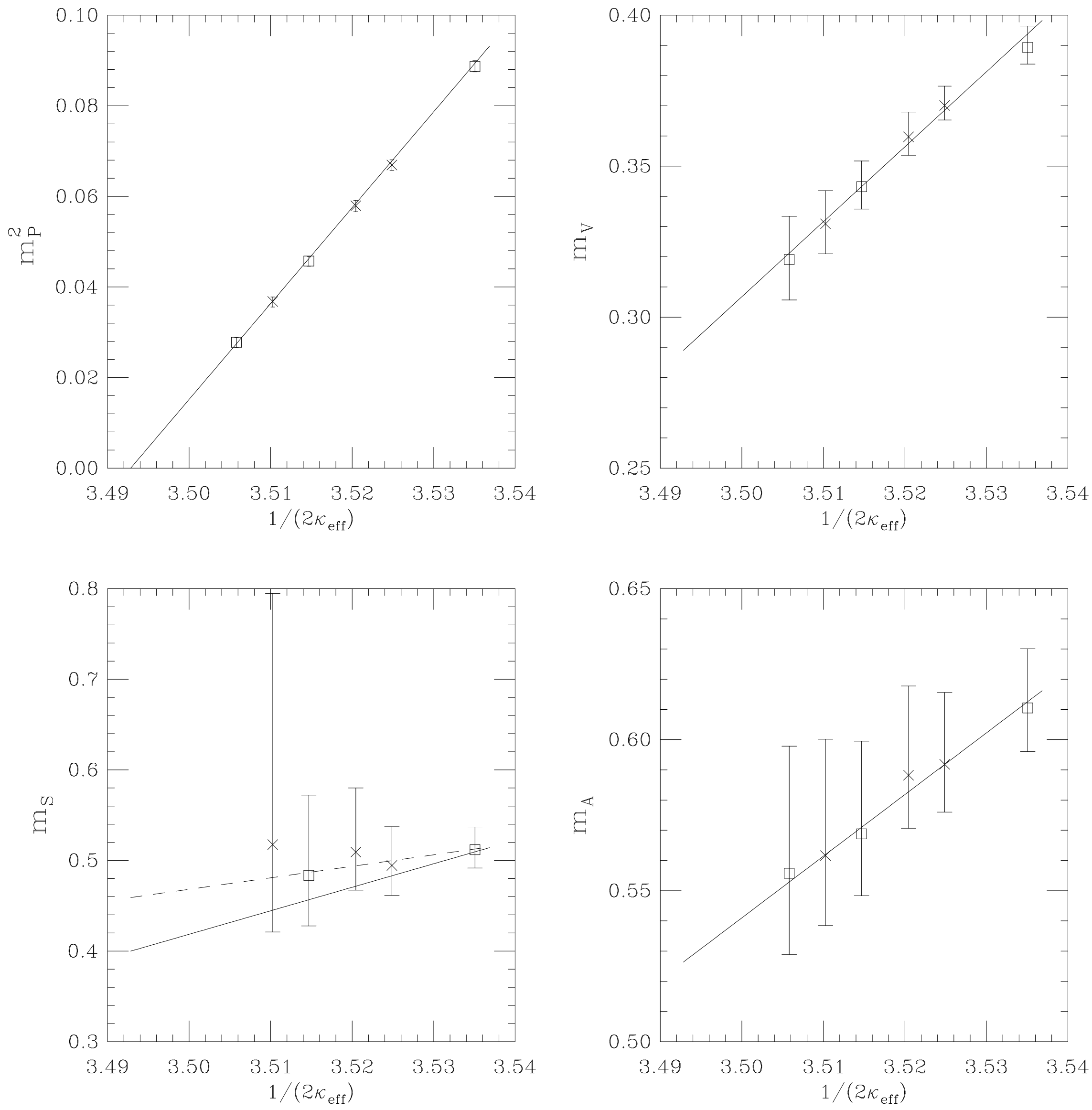

Figure 4.10: Chiral extrapolations for (clockwise, from top left) the pseudoscalar, vector, pseudovector and scalar mesons. Degenerate κ combinations are marked ($\Box$); non-degenerate ($\times$).

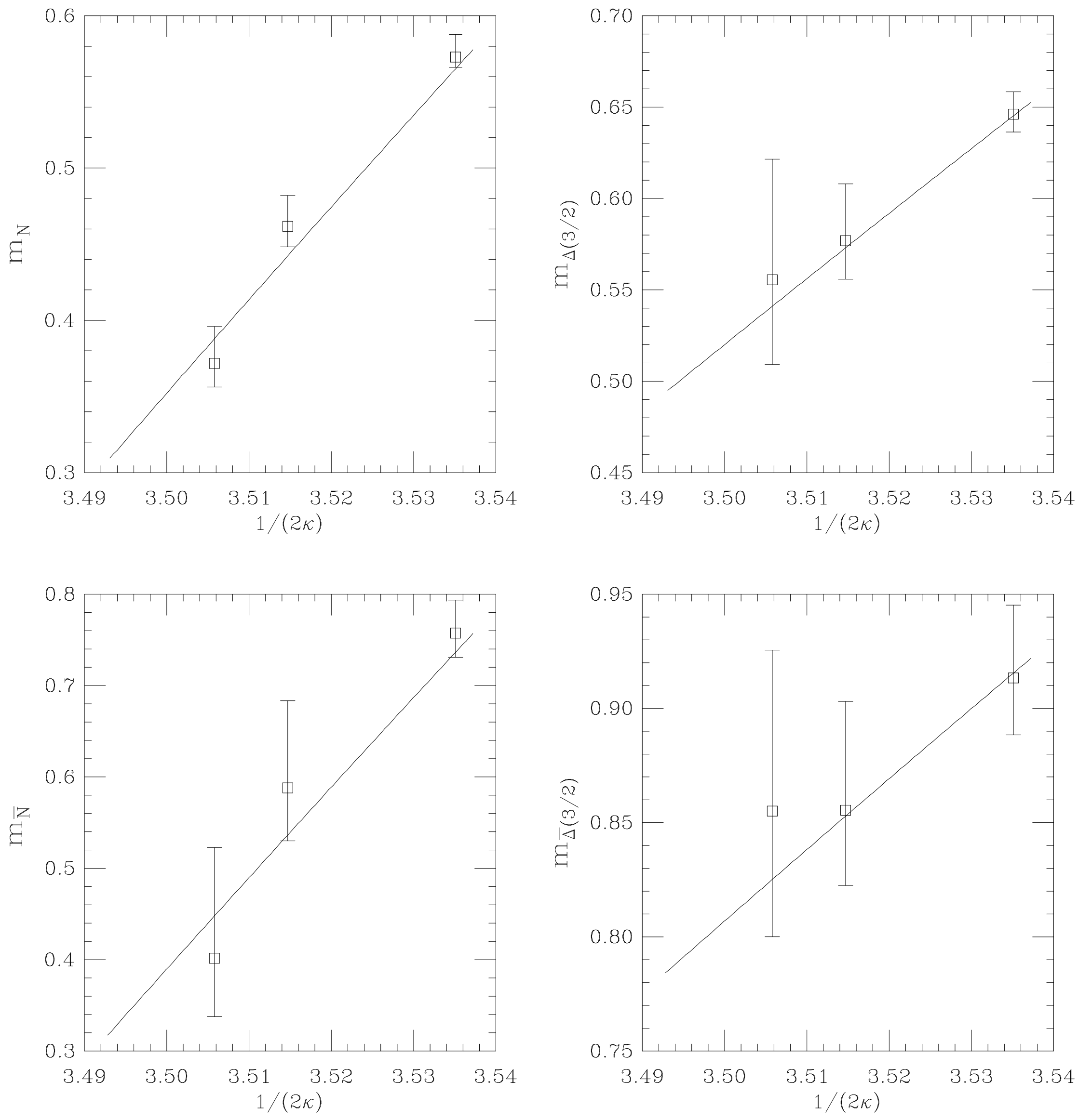

Figure 4.11: Chiral extrapolations for the nucleon and $\Delta(\frac{3}{2})$ baryons (top) and their opposite parity partners (bottom).

physical quantity	lattice value	a^{-1} (GeV)
m_ρ	$0.29\,^{+1}_{-1}$	$2.7\,^{+1}_{-1}$
m_{b_1}	$0.53\,^{+4}_{-3}$	$2.3\,^{+2}_{-2}$
m_{a_0}	$0.40\,^{+6}_{-8}$	$2.5\,^{+6}_{-3}$
m_N	$0.31\,^{+3}_{-2}$	$3.0\,^{+2}_{-3}$
m_Δ	$0.50\,^{+4}_{-3}$	$2.5\,^{+2}_{-2}$
$\sqrt{K}$	0.161(3)	2.73(5)

Table 4.9: Chirally-extrapolated lattice masses and corresponding scales compared with the scale from the string tension [26].

$\chi^2/d.o.f.$ of 2.7/1. However, as discussed in §(4.3), there is a suspicion that the nucleon mass at $\kappa = 0.14262$ is the victim of a statistical fluctuation of $\mathcal{O}(5\%)$. Consequently, I feel unable to conclude that the observed nonlinear behaviour in the extrapolation of the nucleon is a feature of interesting chiral behaviour and quote results only from the linear fit. There remains, however, a significant degree on uncertainty in this procedure.

It is, however, interesting to note that a similar feature exists in the nucleon-parity-partner channel, the $\tilde{N}$. The larger errors in this channel mean that the linear fit is much more believable ($\chi^2/d.o.f. = 1.6/1$), but since the $\tilde{N}$ is extracted from the same interpolating operator as the nucleon it provides a possible corollary to the idea of a statistical fluctuation.

I note that the extrapolations of the $\Delta(\frac{3}{2})$ and its opposite-parity state, the $\tilde{\Delta}(\frac{3}{2})$, suffer no such sickness, although the errors are larger. There is a good linear fit for the $\Delta(\frac{1}{2})$, again with large errors; for its parity partner, the $\tilde{\Delta}(\frac{1}{2})$, we have only two points and so can lend no credence to the exact linear fit.

In Table 4.9 I present the inverse lattice spacing, a^{-1}, calculated from the chiral extrapolations of various masses. Throughout this work I use m_ρ to set the "official" scale for the $\beta = 6.2$ lattice. Note that the close agreement between the scales from m_ρ and the string tension suggests that later results presented in physical units should not be too dependent on the chiral extrapolation.

4.6 Strange Quark Mass

So far we have used the chirally extrapolated pseudoscalar and vector masses to set κ_{crit} and the lattice scale, a^{-1}. κ_{crit} is the value of the hopping parameter corresponding to zero u and d quark masses on the lattice; to calculate the masses of hadrons containing strange quarks we need to find κ_s.

This we get from the fit to the ratio $m_P^2(\kappa_1, \kappa_2)/m_\rho^2$ for all six (κ_1, κ_2) combinations by extrapolating κ_1 to κ_{crit} and using κ_2 to match the ratio to the experimental value $m_K^2/m_\rho^2 = 0.413$. This gives

$$\kappa_2 = \kappa_s = 0.1419\,^{+1}_{-1}. \tag{4.83}$$

A noteworthy point is that m_s lies between two of our quark masses; results using the strange quark mass are thus obtained by *interpolation*, an intrinsically more robust procedure than extrapolation. Indeed, had we initially guessed correctly in the choice of simulation κ's we could have simulated hadrons containing strange quarks directly on the lattice.

This value of κ_s corresponds to a lattice-regularised strange quark mass in physical units of

$$m_s(a^{-1}) = \frac{1}{2a}\left(\frac{1}{\kappa_s} - \frac{1}{\kappa_{crit}}\right) = 82\,^{+8}_{-8}\ \text{MeV}.$$

From this we can determine the renormalised m_s in the $\overline{MS}$ scheme at a reference scale 2 GeV:

$$m_s^{\overline{MS}}(2\ \text{GeV}) = 109\,^{+11}_{-11}\ \text{MeV}.$$

This agrees well with previous lattice evaluations of m_s: reference [57] quotes $m_s^{\overline{MS}}(2\ \text{GeV}) = 100 \pm 6$ MeV from a simulation using the Wilson action; reference [58] quotes 89 ± 9 MeV using the clover action at $\beta = 6.0$. Reference [24] quotes two values for m_s from simulations with both the Wilson and clover actions; for the clover action at $\beta = 6.0$ they obtain $m_s^{\overline{MS}}(2\ \text{GeV}) = 103 \pm 3$ MeV.

At the 1 GeV scale, the current-quark value for m_s is 199 ± 33 MeV [59]; reference [24] evolves this number to the 2 GeV scale to obtain 150 ± 30 MeV, noting that lattice estimates tend to lie at the lower end of expectations.

Hadron spectrum in lattice units			
m_{η_s}	$0.251\,^{+13}_{-11}$	$1/(f_\rho Z_V)$	$0.380\,^{+\ 9}_{-16}$
m_{K^*}	$0.326\,^{+13}_{-12}$	$1/(f_{K^*} Z_V)$	$0.359\,^{+\ 6}_{-11}$
m_ϕ	$0.364\,^{+12}_{-11}$	$1/(f_\phi Z_V)$	$0.337\,^{+4}_{-7}$
$m^2_{K^*} - m^2_K$	$0.075\,^{+6}_{-5}$	f_ϕ/f_ρ	$1.13\,^{+2}_{-3}$
m_{a_0}	$0.40\,^{+6}_{-8}$	f_{K^*}/f_ρ	$1.06\,^{+1}_{-2}$
m_{a_1}	$0.35\,^{+5}_{-6}$	m_N	$0.31\,^{+3}_{-2}$
m_{b_1}	$0.53\,^{+4}_{-3}$	m_Ξ	$0.43\,^{+3}_{-1}$
f_π/Z_A	$0.040\,^{+1}_{-2}$	m_Σ	$0.37\,^{+3}_{-2}$
f_K/Z_A	$0.048\,^{+1}_{-2}$	$m_{\Delta(\frac{3}{2})}$	$0.50\,^{+4}_{-3}$
f_K/f_π	$1.20\,^{+3}_{-2}$	m_Ω	$0.61\,^{+2}_{-2}$
$f_\pi/(m_\rho Z_A)$	$0.142\,^{+6}_{-9}$	$m_{\Delta(\frac{1}{2})}$	$0.84\,^{+13}_{-13}$
$f_K/(m_\rho Z_A)$	$0.165\,^{+7}_{-8}$	$m_{\tilde{N}}$	$0.32\,^{+17}_{-\ 7}$
$f_K/(m_{K^*} Z_A)$	$0.148\,^{+4}_{-6}$	$m_{\tilde{\Delta}(\frac{3}{2})}$	$0.78\,^{+6}_{-6}$

Table 4.10: Extrapolated/interpolated values of hadron masses and decay constants in lattice units, calculated using the fit (B) parameters in Tables 4.7 and 4.8.

4.7 Results in Physical Units — the Light and Strange Regimes

In this section I shall use the "physical" κ values, κ_{crit} and κ_s, and the lattice scale derived from the ρ-meson mass to determine the light hadron mass spectrum and meson decay constants in physical units. First of all I present, in Table 4.10, these quantities in lattice units, calculated using the fit (B) parameters of Tables 4.7 and 4.8.

In this table I have obtained m_{K^*}, $m^2_{K^*} - m^2_K$, f_K, f_{K^*} and related ratios by extrapolating κ_1 of Equation (4.79) to κ_{crit} and interpolating in κ_2 to κ_s; m_{η_s}, m_ϕ and f_ϕ were obtained by interpolation to (κ_s, κ_s). For the baryons, the mass of the Ω^- (quark content sss) is obtained from the flavour-symmetric, $J^P = \frac{3}{2}^+$ $\Delta(\frac{3}{2})$ channel by interpolation in the single κ value to κ_s.

m_Ξ is determined from the $I(J^P) = \frac{1}{2}(\frac{1}{2}^+)$ nucleon channel by interpolating κ to $\frac{1}{3}(2\frac{1}{\kappa_s} + \frac{1}{\kappa_{crit}})$; m_Σ is similarly determined by interpolation of the nucleon to $\frac{1}{3}(\frac{1}{\kappa_s} + 2\frac{1}{\kappa_{crit}})$. These last two interpolations extend the idea that, in the quenched approximation, the hadron mass depends only on the sum of the valence quark masses.

Note that in Table 4.10, the meson decay constants need to be multiplied by appropriate renormalisation constants before we can compare them with experiment. At $\beta = 6.2$, the only estimates available for Z_A and Z_V are perturbative ones [60], determined using the effective coupling, as discussed in references [26, 61]:

$$Z_A \simeq 0.97, \qquad Z_V \simeq 0.83. \tag{4.84}$$

With these values for the renormalisation constants, and $a^{-1}(m_\rho)$ from Table 4.9, the final results for the light hadron spectrum are presented in Table 4.11. Note that the η_s meson is not a physical particle: it is the hypothetical pure $s\bar{s}$ pseudoscalar. The mass of 0.686 GeV is a theoretical prediction [52], hence the quotes.

The third column in this table indicates the deviation of the lattice result from the equivalent experimental number, in terms of the corresponding upper or lower errorbar. From this we see that, for the hadron masses, we have agreement to within, at worst, 2.6σ. In the strange sector the lattice estimates tend to be low; in the case of the hyperfine splitting $m_{K*}^2 - m_K^2$ this may be a function of quenching, which could lead to lower mass estimates for vector mesons, relative to the pseudoscalars. However, a deviation of 2σ is insufficient to stand as clear evidence for an identified effect of quenching.

Experimentally, this hyperfine splitting is only weakly dependent on the light quark mass ($m_\rho^2 - m_\pi^2 = 0.57$ GeV^2, $m_{K*}^2 - m_K^2 = 0.55$GeV^2) [25]. Plotting our combined data for $m_V^2 - m_P^2$ in Figure 4.12 we can see that they show, indeed, little dependence on the quark mass (parameterised by the square of the pseudoscalar mass in this figure). The physical points marked on the graph are for the ρ-π and K^*-K systems. Except for the heaviest point, the lattice data lie on a line with a slope consistent with an imagined line through the experimental data. It is clear that the low extrapolated value of $m_{K*}^2 - m_K^2$ is born of data which lie consistently below the experimental points.

The results for the meson decay constants are disappointing, with the pseudo-

	lattice estimates	experiment	deviation
m_{η_s}	$0.67\,^{+1}_{-1}$ GeV	"0.686 GeV"	-1.6σ
m_{K^*}	$0.87\,^{+1}_{-1}$ GeV	0.892 GeV	-2.2σ
m_{ϕ}	$0.97\,^{+2}_{-1}$ GeV	1.020 GeV	-2.5σ
$m^2_{K^*} - m^2_K$	$0.53\,^{+1}_{-1}$ $(\mathrm{GeV})^2$	0.55 $(\mathrm{GeV})^2$	-2.0σ
m_{a_0}	$1.06\,^{+16}_{-21}$ GeV	0.980 GeV	$+0.4\sigma$
m_{a_1}	$0.93\,^{+14}_{-18}$ GeV	1.260 GeV	-2.4σ
m_{b_1}	$1.40\,^{+14}_{-10}$ GeV	1.235 GeV	$+1.7\sigma$
f_π	$0.102\,^{+6}_{-7}$ GeV	0.132 GeV	-5.0σ
f_K	$0.123\,^{+5}_{-6}$ GeV	0.160 GeV	-7.4σ
$1/f_\rho$	$0.316\,^{+7}_{-13}$	0.28	$+2.8\sigma$
$1/f_{K^*}$	$0.298\,^{+5}_{-9}$		
$1/f_\phi$	$0.280\,^{+3}_{-6}$	0.23	$+8.3\sigma$
f_π/m_ρ	$0.138\,^{+6}_{-9}$	0.172	-5.7σ
f_K/m_ρ	$0.160\,^{+7}_{-8}$	0.208	-6.9σ
f_K/m_{K^*}	$0.144\,^{+4}_{-6}$	0.179	-8.8σ
m_N	$0.82\,^{+9}_{-6}$ GeV	0.938 GeV	-1.3σ
m_Ξ	$1.16\,^{+6}_{-3}$ GeV	1.315 GeV	-2.6σ
m_Σ	$0.99\,^{+7}_{-5}$ GeV	1.190 GeV	-2.9σ
$m_{\Delta(\frac{3}{2})}$	$1.32\,^{+13}_{-10}$ GeV	1.232 GeV	$+0.9\sigma$
m_Ω	$1.61\,^{+7}_{-5}$ GeV	1.672 GeV	-0.9σ
$m_{\Delta(\frac{1}{2})}$	$2.23\,^{+38}_{-40}$ GeV	1.910 GeV	$+0.8\sigma$
$m_{\tilde{N}}$	$0.84\,^{+46}_{-19}$ GeV	1.535 GeV	-1.5σ
$m_{\tilde{\Delta}(\frac{3}{2})}$	$2.09\,^{+21}_{-20}$ GeV	1.700 GeV	$+2.0\sigma$

Table 4.11: Values of hadron masses and decay constants in physical units, using the scale from m_ρ.

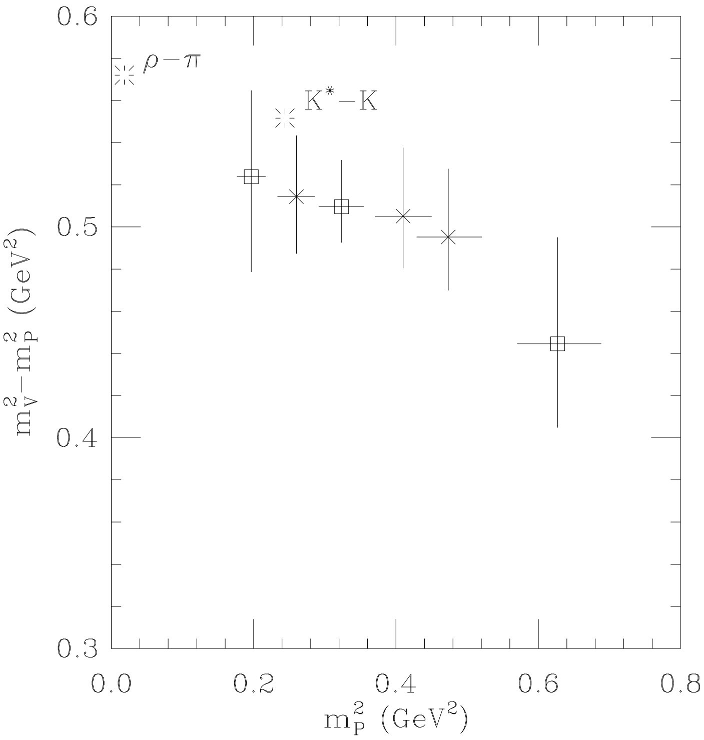

Figure 4.12: Vector-pseudoscalar meson mass splitting for all six κ combinations; $\square$ denote degenerate data, $\times$ non-degenerate. Included are the experimental values for $m_\rho^2 - m_\pi^2$ and $m_{K^*}^2 - m_K^2$ ($\ast$).

scalar numbers too large and the vector numbers too small, each by up to 8σ. For the pseudoscalar, this shortfall has been noted in recent simulations using the standard Wilson action [62]. In this reference it is argued that this is to be expected as a product of quenching, since one of the effects of quenching is to reduce the size of the meson wavefunction at the origin at hence the decay constants. The discrepancy may also be due in part to the perturbative value of the renormalisation constant Z_A. Recent non-perturbative studies at $\beta = 6.0$ using a single quark mass yield a higher value: $Z_A \sim 1.09(3)$ [63]. It is thus possible that a full, non-perturbative evaluation of Z_A at $\beta = 6.2$ will raise the values of the decay constants to be more in line with experiment.

Any uncertainty in Z_A is removed if we look at ratios of decay constants, in particular our lattice estimate (Table 4.10) $f_K/f_\pi = 1.20\,^{+3}_{-2}$. This is in excellent agreement with the experimental value 1.22 and suggests that, despite working

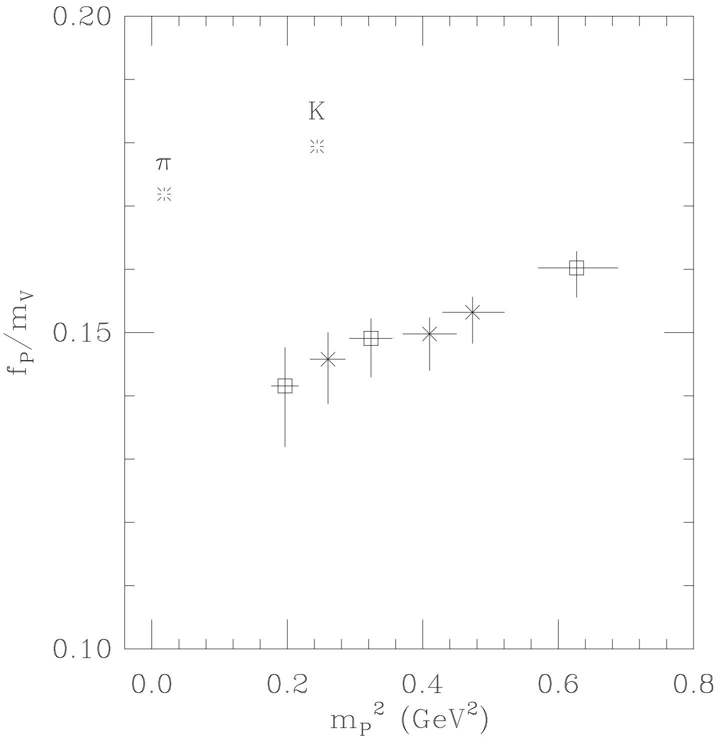

Figure 4.13: f_P/m_V against m_P in physical units. Degenerate quark data are marked □, non-degenerate ×. Experimental points for the kaon and pion are also marked (∗).

in the quenched approximation, we have obtained the correct dependence on m_s. Again, a decision on quenching awaits further work, particularly a non-perturbative determination of the coefficient Z_A.

As a corollary to the previous paragraph, in Figure 4.13 I plot the ratio f_P/m_V against the pseudoscalar mass squared. It is clear from this figure that the slope of the data matches closely that of the experimental points, and that an increase in Z_A of $\mathcal{O}(25\%)$ would yield excellent agreement between the two.

The story is somewhat more mysterious for the vector meson decay constants. The values given in Table 4.11 lie above their experimental counterparts, by $\sim 3\sigma$ for the ρ-meson and 8σ for the ϕ. However, we again see agreement between the slopes of our data and experiment (Figure 4.14). The discrepancy in $1/f_V$ has the opposite sign to that expected from the preceding quenching/wavefunction

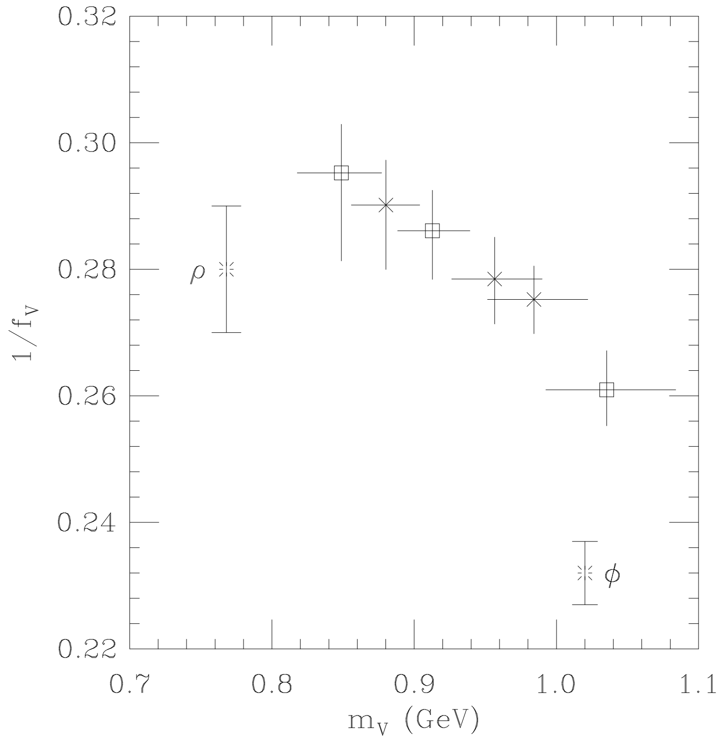

Figure 4.14: $1/f_V$ against m_V in physical units. Degenerate quark data are marked □, non-degenerate ×. Experimental points for the ρ and ϕ mesons are also marked (∗).

arguments; nor is it likely that its source lies in the use of the perturbative Z_V, since this is known to be close to its non-perturbative value [63]. Possible causes for this oddity in the behaviour of $1/f_V$ include finite-volume or finite lattice spacing errors.

The results for the baryons are encouraging, although the numbers for the nucleon, Ξ and Σ belie the possible problems in the chiral extrapolation. However, in Table 4.12 I list the ratios of some of the baryon masses, together with their experimental values. In this table, I have effectively fixed the scale using the nucleon mass, thus removing some of the effects of the chiral extrapolation. The discrepancies are smaller than those of Table 4.11 and provide good evidence of consistency in the baryon sector, and provide further support for the accuracy of our determination of κ_s.

	lattice estimates	experiment	deviation
m_Σ/m_N	$1.20\,^{+4}_{-4}$	1.27	-1.8σ
m_Ξ/m_N	$1.40\,^{+7}_{-7}$	1.40	$+0.0\sigma$
$m_{\Delta(\frac{3}{2})}/m_N$	$1.60\,^{+18}_{-17}$	1.31	$+1.7\sigma$
m_Ω/m_N	$1.96\,^{+15}_{-17}$	1.78	$+1.1\sigma$

Table 4.12: Baryon mass ratios.

The $\Delta(\frac{1}{2})$ and the two parity-partner states (I do not quote an estimate for the $\tilde{\Delta}(\frac{1}{2})$) have errors approaching 50%; it is likely that we are not seeing any real signal for these channels, although the central values are "in the ballpark".

In general, despite working in the quenched approximation, this simulation has yielded a hadron spectrum in good agreement with experiment. We have certainly shown that the rule

$$(\text{hadron mass}) \propto \sum(\text{quark masses})$$

holds for quark masses up to and slightly beyond that of the strange quark. Problems remain in the normalisation of the decay constants, though again we are seeing the correct dependence on quark mass.

In the next chapter I aim to extend the idea of fitting 2-κ planes through the data to the fitting of a more general surface to a combination of the light-light data presented so far and sets of heavy-light data calculated using smeared operators.

4.8 A Digression — the R Parameter in Chiral Perturbation Theory

As a slight digression from the main spectroscopic thrust of this and the next chapter, I present here a brief foray into the realms of quenched chiral perturbation theory and a calculation of some relevant parameters.

Chiral perturbation theory (ChPT) [64] has proved a useful tool in analysing the chiral behaviour of quantities involving the pseudo-Goldstone bosons of QCD, particularly in identifying and calculating chiral logarithms. Chiral logarithms provide information as to the size of next-to-leading-order corrections to the chiral behaviour of quantities like m_π^2, f_π, etc. On the lattice, chiral logarithms can be used to test whether the simulation is correctly describing contributions from pion loops and the pion cloud around a hadron. In addition, chiral logarithms are associated with volume-dependent corrections [66, 65], something of great import for lattice calculations.

To date, most lattice simulations of QCD, including the ones in this work, have been performed in the quenched approximation in which the fermion determinant in the path integral is set to one, thus eliminating fermion loops from the background gauge fields. As a consequence there has been a growing interest in recent years in developing chiral perturbation theory for the quenched approximation (QChPT).

At present there are two approaches: the quark flow method used by Sharpe [67, 68, 69] and the Lagrangian method of Bernard and Golterman [70, 71]. Heuristically, the quark flow approach begins with the usual chiral Lagrangian of pseudo-Goldstone bosons and "quenches" it by looking at the $N_{colours} \to \infty$ limit — this has the effect of removing the fermion loops [64, 72]. One then writes down all the meson diagrams corresponding to the process of interest, associates with them one or more QCD quark-flow diagrams and sums these to obtain the chiral behaviour [69]. In practice this is difficult to do in any but the simplest cases.

The Lagrangian approach begins with the QCD Lagrangian and adds, for each fermionic quark, a scalar boson ghost quark. The ghost determinant then, by construction, exactly cancels the fermion determinant yielding a quenched theory. One then constructs the corresponding low-energy effective (chiral) theory from this new Lagrangian and does ChPT as usual. This has the advantage of being a more systematic approach than the quark-flow diagram method, enabling one to calculate more complex quantities.

One notable difference between QChPT and ChPT is that the mass of the singlet pseudoscalar, the η', plays an important rôle in the quenched theory (for reasons, see references [69, 70]). This leads to new terms in the chiral expressions for m_π, m_K, f_π etc. As a consequence, many quantities have completely different chiral expressions in the quenched theory.

It is thus an interesting exercise to compare results from QChPT and ChPT, both with each other and with lattice data. However, this can only be done with parameters independent of the bare couplings of the respective theories since these tend to be arbitrary and, in general, different. One such parameter is the ratio

$$R \equiv \frac{f_K}{\sqrt{f_\pi f_{\pi'}}}. \tag{4.85}$$

(The notation is that of reference [71].) $f_{\pi'}$ here is the decay constant associated with an $s\bar{s}$ pseudoscalar — the hypothetical $\eta_s(686)$.

In full-QCD ChPT, R has the form

$$R_{full} = 1 - \frac{1}{64\pi^2 f^2}\left[m_\pi^2 \log\left(\frac{m_K^2}{m_\pi^2}\right) + m_{\pi'}^2 \log\left(\frac{m_K^2}{m_{\pi'}^2}\right)\right], \tag{4.86}$$

and in the quenched theory

$$\begin{aligned} R_{qu} &= 1 + \frac{\mu^2/3}{16\pi^2 f^2}\left[\frac{m_{\pi'}^2 + m_\pi^2}{2(m_{\pi'}^2 - m_\pi^2)}\log\left(\frac{m_{\pi'}^2}{m_\pi^2}\right) - 1\right] \\ &\equiv 1 + \frac{\delta}{2}\left[\frac{m_{\pi'}^2 + m_\pi^2}{2(m_{\pi'}^2 - m_\pi^2)}\log\left(\frac{m_{\pi'}^2}{m_\pi^2}\right) - 1\right]. \end{aligned} \tag{4.87}$$

If we evaluate these two expressions using "real world" data, i.e. using the values $m_\pi = 140$ MeV, $m_K = 494$ MeV, $m_{\pi'} = m_{\eta_s} = 686$ MeV, $f = f_\pi = 132$ MeV and $\mu^2/3 = (500 \text{ MeV})^2$ (this last from the full QCD η' mass [71]) we get

$$R_{full} = 1.024, \qquad R_{qu} = 1.066.$$

The difference is quite marked ($\mathcal{O}(4\%)$).

In comparing with the lattice data we have a problem — what value should we use for m_π^2? On the lattice this is taken to be zero, thus defining the chiral limit. This obviously will not do since the quenched approximation (certainly) blows up as $m_\pi^2 \to 0$. I choose two solutions: the first is to take our actual simulation data for m_π^2 at $\kappa = 0.14262$, corresponding to a quark mass of $\sim$0.013 or $\sim$34 MeV. The second is to extrapolate to an effective κ value corresponding to an arbitrary, "down-ish", quark mass of $\frac{10\ MeV}{2700\ MeV} \sim 0.004$. For the other quantities I use the values of Table 4.11, along with the same $\mu^2/3 = (500 \text{ MeV})^2$.

The resulting values:

$$R_{full}(m = 0.004) = 1.026, \qquad R_{qu}(m = 0.004) = 1.048,$$

$$R_{full}(m = 0.013) = 1.031, \qquad R_{qu}(m = 0.013) = 1.008.$$

The R_{full}'s show a small increase with quark mass, whereas the the quenched number falls significantly with increasing m. The quenched number from our extrapolated results for the decay constants f_K and f_π, along with the interpolated value $f_{\eta_s}/Z_A = 0.056\,^{+2}_{-2}$ is

$$R_{qu}(f_K, f_\pi, f_{\eta_s}) = 1.015\,^{+4}_{-3}. \tag{4.88}$$

What conclusions should we draw? Ideally, we would wish the ratio of lattice decay constants to lie closer to the QChPT number, since it is hoped that QChPT describes the lattice theory as $m \to 0$. This is true if we compare Equation (4.88) with the value of R_{qu} at $m = 0.013(\kappa = 0.14262)$. However, this quark mass is not particularly light — it is only $\sim$40% of the mass of the lattice strange quark (§(4.6)). At the smaller quark mass of 0.004 the quenched result is larger than the full ChPT result by $\sim$2%. In addition, the factor of $\mu^2/3 = (500 \text{ MeV})^2$ is a full-QCD result and may not be appropriate for our quenched lattice data. There is also the problem that the value of f_π used is that of Table 4.11 (102 MeV) which is likely to be too small.

One thing we can do, then, is use our lattice data to determine the coefficient δ in Equation (4.87). Since we have degenerate and non-degenerate values for the pseudoscalar decay constant f_P we can fit

$$R = \frac{f_P(\kappa_1, \kappa_2)}{\sqrt{f_P(\kappa_1, \kappa_1) f_P(\kappa_2, \kappa_2)}},$$

against the variable

$$x \equiv \frac{m_P^2(\kappa_1) + m_P^2(\kappa_2)}{2\left(m_P^2(\kappa_2) - m_P^2(\kappa_1)\right)} \log\left(\frac{m_P^2(\kappa_2)}{m_P^2(\kappa_1)}\right) - 1, \quad \kappa_2 < \kappa_1,$$

as

$$R = a + \frac{\delta}{2} x. \tag{4.89}$$

By fixing $a = 1$ we can determine δ; by letting a vary in the fit we can check that our data agree with $a = 1$.

In Figure 4.15 I present the results of these fits, taking correlations between points into account. Fixing $a = 1$ we obtain for the coefficient in the QChPT expression

$$\frac{\delta}{2} = 0.10\,^{+10}_{-\ 6}. \tag{4.90}$$

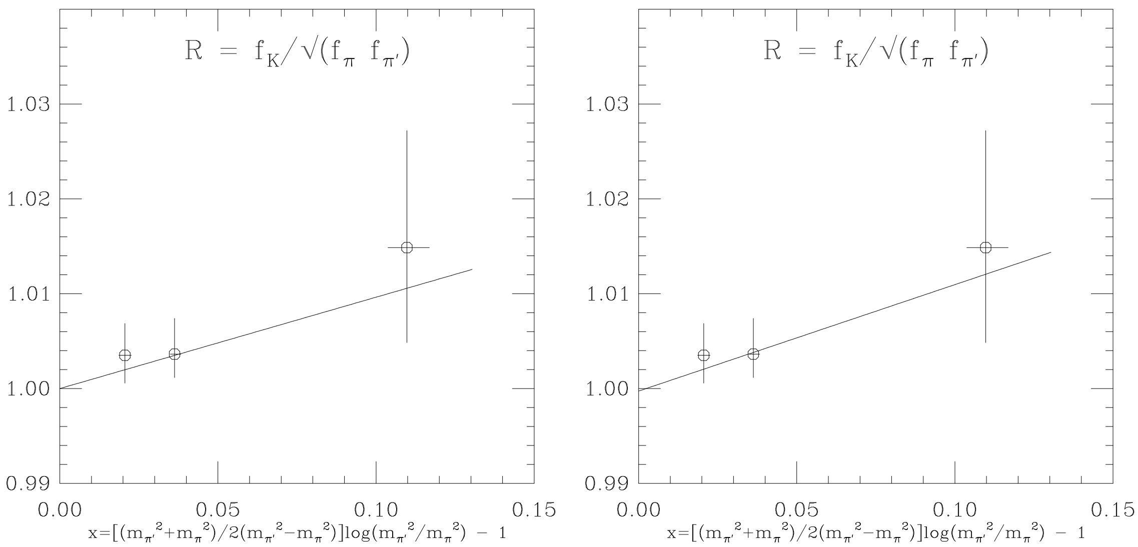

Figure 4.15: Linear fit of the QChPT expression Equation (4.89) to UKQCD data, with (left) a fixed at unity and (right) a allowed to vary freely.

Despite the disappointingly large errors, this agrees well with the continuum-value coefficient $(\mu^2/3)/16\pi^2 f^2 = 0.09$ and with the value 0.1 quoted in reference [69]; it is, at least, encouragingly different from zero by $\sim 2\sigma$. Allowing a in Equation (4.89) to vary freely yields

$$a = 0.9997\,{}^{+8}_{-7}, \quad \frac{\delta}{2} = 0.11\,{}^{+11}_{-\ 7},$$

completely consistent with $a = 1$ and Equation (4.90).

If we now use this value of $\delta/2$ to re-evaluate R_{qu} for the lattice data at the two quark masses 0.004 and 0.013 we find

$$R_{qu}(m = 0.004) = 1.030, \qquad R_{qu}(m = 0.013) = 1.008.$$

Again, it is difficult to conclude anything concrete, except to note that R in Equation (4.88) seems to suggest we evaluate m_π^2 at a quark mass somewhere between 0.004 and 0.013. Indeed, if we fix $R = 0.015$ in Equation (4.87) we can solve for m_π^2, yielding $m_\pi^2 = 0.015$. Using the fit parameters of Table 4.7 suggests a quark mass of $\sim$0.007 or $\sim$20 MeV.

One thing we can do is use our calculated value of δ to check the proposed chiral behaviour for the pion mass [69]:

$$m_\pi^2 = (a_\pi m)^{1/(1+\delta)} (\Lambda^2)^{\delta/(1+\delta)}. \qquad (4.91)$$

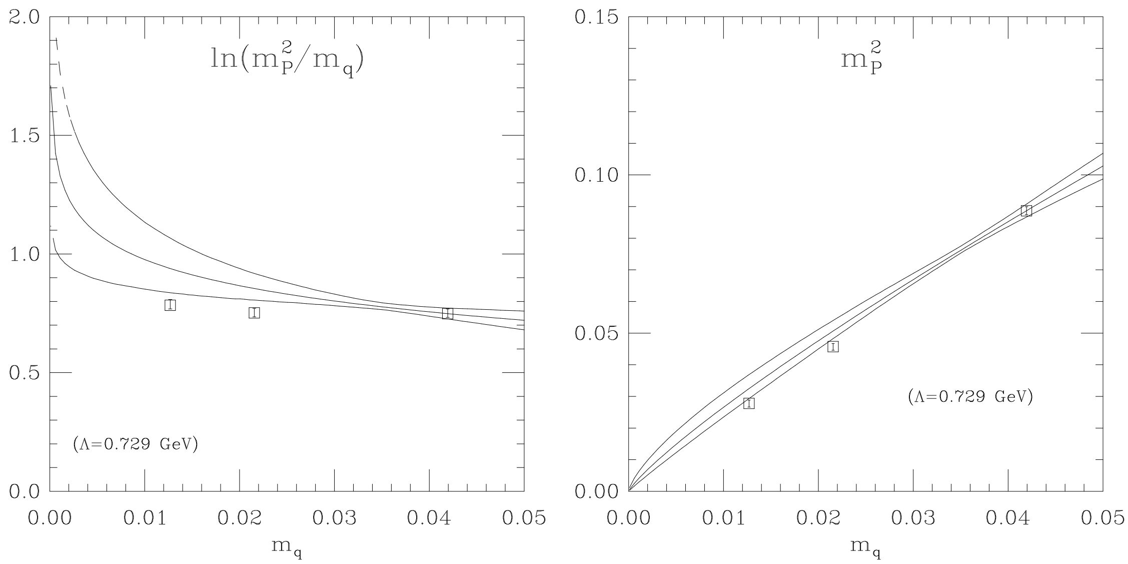

Figure 4.16: Degenerate pseudoscalar meson data, plotted against quark mass m. The curves are QChPT predictions based on Equation (4.91).

Here, a_π is the coefficient of the quark mass in the usual linear extrapolation ($a_\pi \equiv a_2$ in the notation of Table 4.7). Λ is some suitable scale parameter, usually taken to be approximately m_ρ. In Figure 4.16 I plot m_π^2 and the ratio $\log(m_\pi^2/m)$ against quark mass m for the (degenerate) data of §(4.3). Superimposed are the corresponding curves derived from Equation (4.91), using $\delta/2 = 0.10\,^{+10}_{-\ 6}$ and $\Lambda = 729$ MeV. This latter is chosen so that the curve passes exactly through the heaviest data point. The dotted lines correspond to bootstrapped 68% confidence limits, including the bootstrap error in δ. As has been noted before [73], the curves from these terms alone tend to miss the lattice data; adding arbitrary linear and quadratic terms can force the curves to pass through the data, although the interesting feature, the divergence of $\log(m_\pi^2/m)$ as $m \to 0$, remains.

In this short and somewhat inconclusive section I have tried, in the context of the UKQCD light-hadron spectrum, to present some interesting results from quenched chiral perturbation theory and examine how these predictions make contact with the lattice theory, and *vice versa*. The determination of δ directly from quenched lattice data and the agreement with the continuum value is encouraging and suggests that quenched chiral perturbation theory may soon be a useful and oft-used tool in the analysis of lattice data.

Chapter 5

Combining Light- and Heavy-Quark Spectroscopy

In this chapter I extend the spectroscopic results of Chapter 4 to include non-degenerate mesons calculated with one heavy quark and one light quark. I concentrate on the two "good" meson channels, the pseudoscalar and the vector. In §(5.1) I present the data for the heavy-light P and V mesons for all combinations of the three light κ's with four new heavy κ's. In §(5.2) I extend the idea of fitting κ_1-κ_2 planes through the light-light data to the fitting of a more general surface through both light-light and heavy-light datasets, and in §(5.4) I present the results of these "surface extrapolations" for vector and pseudoscalar mesons at the u, d, s and c quark masses.

5.1 Data in the Heavy-Light Regime

In this section I present the lattice data for pseudoscalar and vector mesons calculated using one heavy and one light quark propagator. I use the same three light-quark propagators — κ values 0.14144, 0.14226 and 0.14262 — as in Chapter 4, this time combined with four heavy-quark propagators with κ's 0.121, 0.125, 0.129 and 0.133. Each light κ is combined with all four heavy κ's to produce twelve non-degenerate heavy-light mesons.

The heavy-quark propagators are calculated using Jacobi-smeared sources, and with both smeared and local sinks. For reasons discussed at the end of Chapter 3, smearing is essential for the extraction of ground-state signals from mesons containing heavy quarks. Heavy-light mesons with both LS (source-smeared) and SS

non-degenerate, heavy-light, SS data.					
κ_l	κ_h	0.121	0.125	0.129	0.133
0.14144	m_P	0.924^{+4}_{-2}	0.823^{+3}_{-2}	0.716^{+3}_{-2}	0.600^{+3}_{-2}
	$\chi^2/d.o.f.$	5.7/9	5.5/9	5.4/9	5.6/9
	m_V	0.945^{+4}_{-2}	0.847^{+4}_{-2}	0.745^{+4}_{-2}	0.638^{+4}_{-2}
	$\chi^2/d.o.f.$	5.9/9	5.6/9	5.5/9	5.3/9
0.14226	m_P	0.901^{+4}_{-2}	0.800^{+4}_{-2}	0.692^{+4}_{-2}	0.575^{+4}_{-2}
	$\chi^2/d.o.f.$	5.3/9	4.9/9	4.8/9	5.2/9
	m_V	0.922^{+5}_{-3}	0.824^{+5}_{-3}	0.722^{+5}_{-3}	0.614^{+5}_{-3}
	$\chi^2/d.o.f.$	4.9/9	4.6/9	4.6/9	4.6/9
0.14262	m_P	0.891^{+5}_{-3}	0.790^{+5}_{-3}	0.682^{+5}_{-3}	0.565^{+5}_{-3}
	$\chi^2/d.o.f.$	5.2/9	4.7/9	4.4/9	4.9/9
	m_V	0.911^{+6}_{-5}	0.814^{+6}_{-5}	0.712^{+6}_{-5}	0.604^{+6}_{-5}
	$\chi^2/d.o.f.$	4.2/9	3.9/9	3.8/9	3.6/9

Table 5.1: Pseudoscalar and vector meson masses using non-degenerate data at 3 light and 4 heavy κ values, with heavy quark propagators smeared at both sink and source.

(source-and-sink-smeared) operators were calculated as part of UKQCD's heavy-quark programme; for the zero-momentum P and V channels, we find that the SS correlators yield the better signals, in terms of lower fit-$\chi^2/d.o.f.$. However, on this last point see the discussion in §(5.2).

The fitting procedure used for the heavy-light propagators is the same as that described in §(4.1). For the SS correlators the optimal fitting regions in terms of stability and $\chi^2/d.o.f.$ are, for the pseudoscalar, $t_{min} = 11$ to $t_{max} = 23$ and for the vector, $t_{min} = 13$ to $t_{max} = 23$; for LS correlators, I find the optimal range to be $t_{min} = 16$ to $t_{max} = 23$.

The lattice data for m_P and m_V are shown in Tables 5.1 and 5.2.

Notice that there is very little difference between the SS and LS mass estimates, although the errors from the SS data tend to be $\mathcal{O}(10\%)$ smaller than those from the LS. Additionally, the $\chi^2/d.o.f.$ are considerably smaller for the SS set — the

non-degenerate, heavy-light, LS data.					
κ_l	κ_h	0.121	0.125	0.129	0.133
0.14144	m_P	$0.927\,^{+3}_{-2}$	$0.825\,^{+2}_{-2}$	$0.717\,^{+2}_{-2}$	$0.600\,^{+2}_{-2}$
	$\chi^2/d.o.f.$	11/6	11/6	12/6	11/6
	m_V	$0.948\,^{+4}_{-3}$	$0.849\,^{+4}_{-3}$	$0.746\,^{+4}_{-3}$	$0.637\,^{+3}_{-3}$
	$\chi^2/d.o.f.$	11/6	9.2/6	7.5/6	5.9/6
0.14226	m_P	$0.903\,^{+4}_{-3}$	$0.801\,^{+4}_{-3}$	$0.692\,^{+3}_{-3}$	$0.574\,^{+3}_{-3}$
	$\chi^2/d.o.f.$	11/6	12/6	13/6	14/6
	m_V	$0.925\,^{+5}_{-5}$	$0.826\,^{+5}_{-5}$	$0.722\,^{+5}_{-4}$	$0.613\,^{+5}_{-4}$
	$\chi^2/d.o.f.$	8.8/6	8.0/6	6.8/6	5.0/6
0.14262	m_P	$0.893\,^{+6}_{-4}$	$0.791\,^{+5}_{-4}$	$0.682\,^{+4}_{-4}$	$0.563\,^{+4}_{-4}$
	$\chi^2/d.o.f.$	12/6	14/6	17/6	18/6
	m_V	$0.911\,^{+7}_{-6}$	$0.814\,^{+7}_{-6}$	$0.711\,^{+7}_{-6}$	$0.602\,^{+7}_{-5}$
	$\chi^2/d.o.f.$	8.1/6	7.9/6	7.1/6	5.0/6

Table 5.2: Pseudoscalar and vector meson masses using non-degenerate data at 3 light and 4 heavy κ values, with heavy quark propagators smeared at the source only.

highest is 5.9/9 compared to a high of 18/6 for the LS.

For the heavier κ combinations, we see a tendency for the LS estimates to be $\sim 1\sigma$ higher than the SS, suggesting that some excited-state contaminations remain in the LS signals. A possible explanation is that, as one increases the hadron mass, one also increases the proximity of the higher-mass excitations, leading to more prolonged contamination for the heavier hadrons. However, since the discrepancy is at the 1σ level, there is little real cause for concern. For the lighter κ values the tendency is reversed, although the increased errorbars reduce the significance of the effect to $\sim \frac{1}{2}\sigma$.

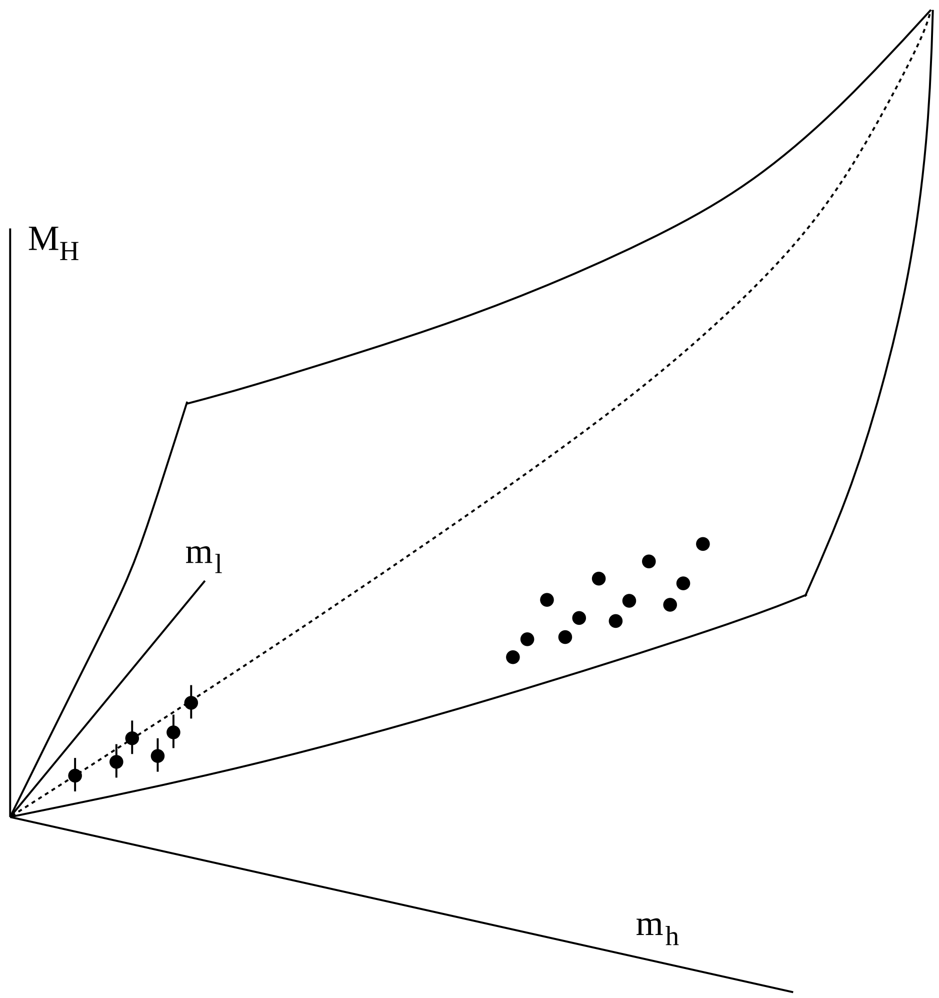

Figure 5.1: Schematic of the general surface passing through light-light and heavy-light data points defined by Equation (5.92).

5.2 Combined Extrapolations

The idea behind the rest of this chapter is the extension of Equation (4.79), which defines the extrapolation-planes of Figure 4.9, to include terms quadratic in the quark masses and so define a more general surface through the mass data — Figure 5.1. This figure shows a surface extrapolation to both the heavy-light data of the previous section and the degenerate and non-degenerate light-light data of Chapter 4, for some arbitrary hadron mass M_H.

The goal of this section is to quantify this proposed behaviour by fitting a function of the two quark masses through the combined light-light (l-l) and heavy-light

(h-l) data. From this I aim to predict hadron masses from one single function from the u-quark to the c-quark regimes.

By analogy with Equation (4.79), I use the following expression to define the fitting surface:

$$a_1 + \frac{a_2}{2}(m_1 + m_2) + \frac{a_3}{2}|m_1 - m_2| + \frac{a_4}{2}\left(m_1^2 + m_2^2\right) + a_5 m_1 m_2. \tag{5.92}$$

This equation differs from Equation (4.79) in two ways, one obvious and one not so. The obvious difference is the inclusion of the quadratic terms with coefficients a_4 and a_5; this is the simplest extension of our original planar fits. Note that the coefficients $a_1 \ldots a_3$ play the same rôles as before.

The hidden difference lies in the definitions of the quark masses $m_{1,2}$. Properly, the quark mass should be defined as the pole in the quark propagator; the definition $m = 1/2\kappa - 1/2\kappa_{crit}$ (Equation (1.10)) is an approximation to this, true only for small m. For heavy quarks we must use the full pole-mass expression, which we obtain from the Wilson fermion matrix, Equation (1.11),

$$M_{WF}(p) = m_{old} + \sum_{\mu}\left(i\gamma_\mu \sin p_\mu + r(1 - \cos p_\mu)\right), \tag{5.93}$$

where $m_{old} = 1/2\kappa - 1/2\kappa_{crit}$. If we set the three-momentum $\vec{p} = (0,0,0)$, take $r = 1$ as usual and look at the pole $M_W(E) = 0$ we have

$$1 + m_{old} = \cos(iE) - i\gamma_4 \sin(iE). \tag{5.94}$$

As $E \to \infty$, the positive and negative energy parts decouple; if we look at the lower two components with $E = -m$ then

$$\begin{aligned} 1 + m_{old} &= \cos(-im) + i\sin(-im) \\ &= e^m \\ \Rightarrow \qquad m &= \log(1 + m_{old}) \end{aligned} \tag{5.95}$$

i.e.

$$m = \log\left\{1 + \frac{1}{2}\left(\frac{1}{\kappa} - \frac{1}{\kappa_{crit}}\right)\right\}, \tag{5.96}$$

which defines our new quark mass m. This is the form we shall use for m_1 and m_2 in Equation (5.92).

5.2.1 SS versus LS data

In §(5.1) I noted that the propagator fits to the SS h-l data gave considerably smaller $\chi^2/d.o.f.$ than those to the LS. However, in Equation (5.97) I give the correlated $\chi^2/d.o.f.$ from the extrapolation fits of the surface Equation (5.92) to the P and V masses for both types of smeared h-l data, each combined with the LL l-l data. The correlated fit is identical to that discussed in §(4.5), save for the use of Equation (5.92).

$$\begin{array}{lll} h\text{-}l(\mathrm{SS}): & m_P^2 : \chi^2/d.o.f. = 60/13, & m_V : \chi^2/d.o.f. = 31/13 \\ h\text{-}l(\mathrm{LS}): & m_P^2 : \chi^2/d.o.f. = 28/13, & m_V : \chi^2/d.o.f. = 9/13 \end{array} \tag{5.97}$$

From this it is clear that using the LS data yields a more convincing fit than does the SS. The highest $\chi^2/d.o.f.$ for the LS propagator fits was 3 for the lightest pseudoscalar; the $\chi^2/d.o.f.$ for the SS extrapolation of m_P^2 is over 4.6. Given that the differences in the propagator fit masses for the two types of smearing is less than 1σ and that the extrapolation $\chi^2/d.o.f.$ are at least twice as good for the LS data, I have chosen to quote extrapolation results using only LS data for the h-l correlators. My suspicion is that the difficulty is caused by the smaller errors in the SS masses; it may be that these errors are underestimated. Consequently I prefer to use the LS data with their slightly larger errors.

5.2.2 Quark mass dependence

Following the approach of §(4.4), I perform two different fits for each of the P and V channels. In the first I allow the coefficient a_3 to vary; in the second I constrain it to be zero. For the h-l data, it is less obvious that the fit should not depend on the quark mass difference, so the test here is perhaps more interesting than that for the l-l data alone. The fit parameters for fits (A) (a_3 free) and (B) (a_3 zero) are given in Table 5.3.

Looking at Table 5.3 we see the same story as for the light-quark data — the coefficient of the mass-difference term is consistent with zero. The agreement is actually better here for the combined l-l/h-l data, with a_3 within $\frac{1}{3}\sigma$ of zero for m_P^2 and within $\frac{1}{2}\sigma$ for m_V. As with the l-l data, I choose to adopt fit (B) with $a_3 = 0$ for all future results.

	fit (A)		fit (B)	
	m_P^2	m_V	m_P^2	m_V
a_1	0.0	$0.283\,^{+7}_{-4}$	0.0	$0.283\,^{+5}_{-4}$
a_2	$1.98\,^{+4}_{-4}$	$2.62\,^{+9}_{-11}$	$1.98\,^{+4}_{-4}$	$2.67\,^{+3}_{-5}$
a_3	$0.002\,^{+5}_{-6}$	$0.05\,^{+9}_{-11}$	0.0	0.0
a_4	$2.31\,^{+2}_{-3}$	$-0.34\,^{+3}_{-5}$	$2.31\,^{+2}_{-2}$	$-0.33\,^{+3}_{-4}$
a_5	$2.2\,^{+3}_{-2}$	$-0.3\,^{+7}_{-2}$	$2.2\,^{+3}_{-2}$	$-0.4\,^{+2}_{-2}$
$\chi^2/d.o.f.$	28/13	9.0/13	28/14	9.3/14

Table 5.3: Fit parameters for light-light/heavy-light pseudoscalar and meson masses, using the fit form in Equation (5.92), (A) with a_3 unconstrained and (B) with $a_3 = 0$.

5.2.3 κ_{crit}, κ_s and $a^{-1}(m_\rho)$

Having combined the *l-l* and *h-l* data into a single fit, I determine the parameters κ_{crit}, κ_s and the lattice scale a^{-1} from the ρ mass. Following the same methods as §(4.5), I obtain for the two κ values

$$\kappa_{crit} = 0.14316\,^{+2}_{-2}, \qquad \kappa_s = 0.14183\,^{+4}_{-5}. \tag{5.98}$$

These numbers are in excellent agreement with the *l-l* only values of $0.14315\,^{+2}_{-2}$ and $0.1419\,^{+1}_{-1}$ respectively. This lends support to the whole idea of combining the *l-l* and *h-l* datasets in this way.

Graphical support can be found in Figure 5.2, in which I plot the combined *l-l* and *h-l* data for m_P^2 against average quark mass, using the fit (B) parameters of Table 5.3. The average quark mass m is defined as

$$m = \frac{m_1 + m_2}{2};$$

note that, because of the new pole-mass definitions of m_1 and m_2, this is *not* the same as taking an average effective κ value as we did with the *l-l* data alone.

The agreement between the 18 data points and the model curve is remarkably good; the $\chi^2/d.o.f.$ of 28/14 is attributable to the small errors on the pseudoscalar

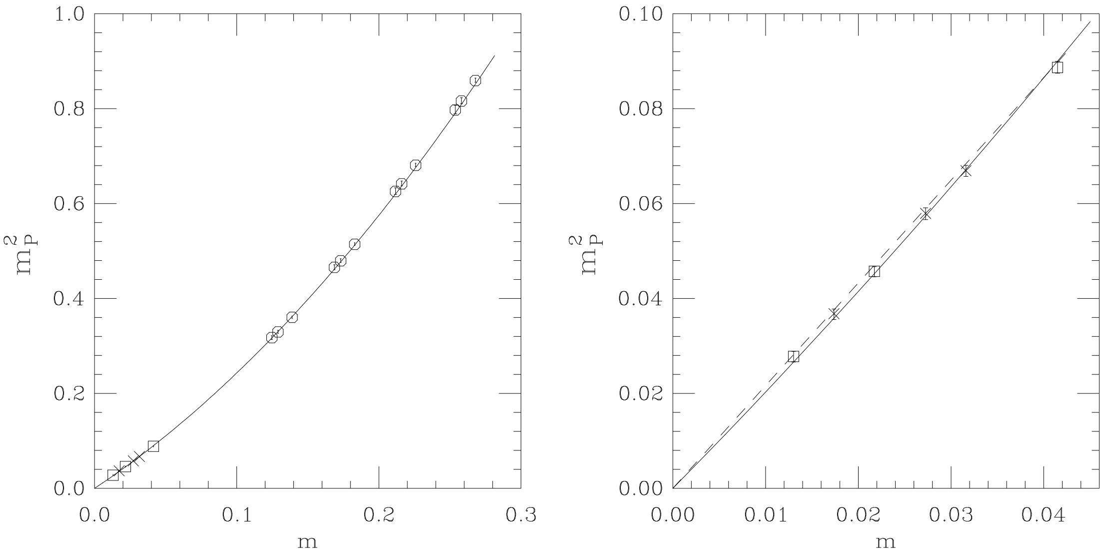

Figure 5.2: *l-l*/*h-l* extrapolation for m_P^2. *h-l* points are marked ○, degenerate *l-l* are marked □ and non-degenerate *l-l* are marked ×. The right-hand plot is an expansion of the *l-l* region of the full plot, with the linear fit to the *l-l* data from §(4.5) superimposed (dotted line).

masses at both heavy and light quark mass. The right-hand plot of Figure 5.2 shows the *l-l* data on an expanded scale. I have superimposed (dotted line) the purely linear fit of Figure 4.10 for comparison. From this we can see that the new fit still preserves a good degree of linearity at light quark masses, indicating its compatibility with the PCAC relation Equation (2.37).

Using the extrapolated mass of the vector meson, $m_V(m_1 = m_2 = 0) = 0.283\,^{+5}_{-4}$, I define the lattice scale by fixing, as before, to the physical ρ mass. This yields

$$a^{-1}(m_\rho) = 2.72\,^{+4}_{-5}\ \mathrm{GeV}. \tag{5.99}$$

This is consistent with the previous scale from the *l-l* ρ-mass of $2.7\,^{+1}_{-1}$ GeV and is in remarkable agreement with the string tension scale of 2.73 ± 5 GeV from Table 4.9.

The accompanying plots are shown in Figure 5.3. Again, the agreement between fit and data is good. The right-hand plot shows the *l-l* points on a scale comparable with Figure 4.10, together with the linear fit to the *l-l* data only (dotted line). As with the pseudoscalar data, linearity is preserved at light quark masses, although the lower position of the heaviest light point perhaps suggests that a

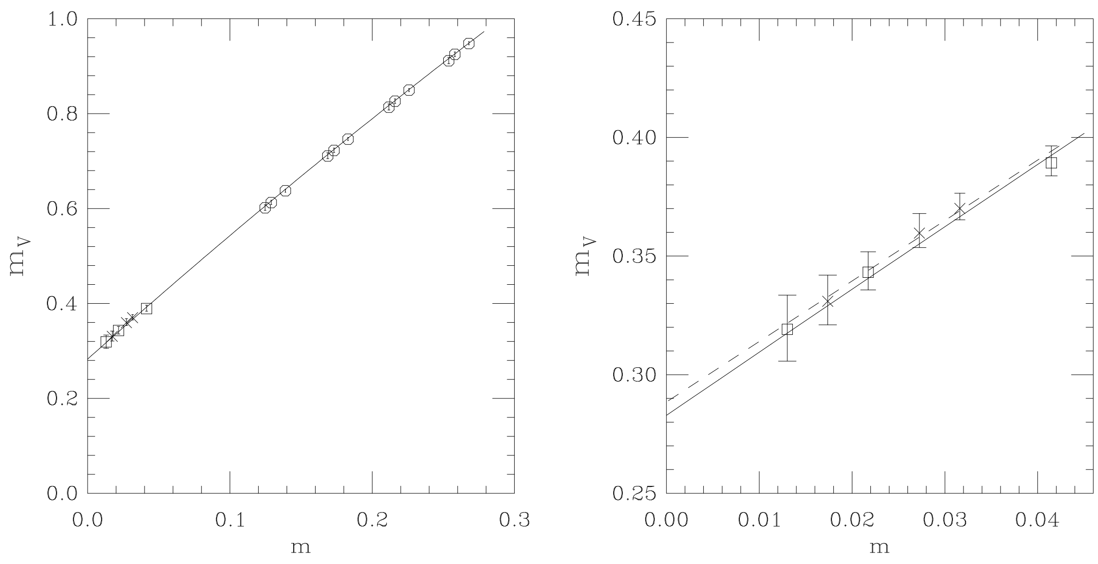

Figure 5.3: *l-l/h-l* extrapolation for m_V. *h-l* points are marked ○, degenerate *l-l* are marked □ and non-degenerate *l-l* are marked ×. As in Figure 5.2, I have superimposed the linear fit from §(4.5) on the expanded *l-l* region in the right-hand plot.

slight curve would better fit the *l-l* data.

5.2.4 How far can we go?

The curves of Figures 5.2 and 5.3 provide strong evidence that we can unite the quark-mass dependences of hadron masses in two quite disparate regimes — light and heavy-light. Is it possible to extend these curves even further to include hadrons composed of *two* heavy quarks, a regime properly discussed in the non-relativistic language of potential models [74]? Purely for interest, I examined the UKQCD heavy-heavy (*h-h*) meson data [48, 75] in this context. I reproduce the data in Table 5.4.

In Figure 5.4 I extend the plots of Figures 5.2 and 5.3, using the fit parameters of Table 5.3, and superimpose the *h-h* data of Table 5.4.

The agreement is surprisingly good, at least to the eye. The extrapolation of the fit curve to large m matches the behaviour of the heavy data quite well, to the point of suggesting it could be possible to fit a single function to all 22 points. If

degenerate, heavy-heavy, LS data				
κ	0.121	0.125	0.129	0.133
m_P	$1.454\,^{+1}_{-1}$	$1.266\,^{+1}_{-1}$	$1.067\,^{+1}_{-1}$	$0.845\,^{+2}_{-1}$
$\chi^2/d.o.f.$	6.2/7	6.2/7	8.5/7	13/7
m_V	$1.464\,^{+1}_{-1}$	$1.279\,^{+1}_{-1}$	$1.084\,^{+2}_{-1}$	$0.877\,^{+2}_{-1}$
$\chi^2/d.o.f.$	4.9/7	3.0/7	1.6/7	1.2/7

Table 5.4: Masses of pseudoscalar and vector mesons composed of degenerate heavy quarks, in lattice units. The fit-range for both channels was $t_{min} = 15$ to $t_{max} = 23$; the correlators were calculated with LS smearing.

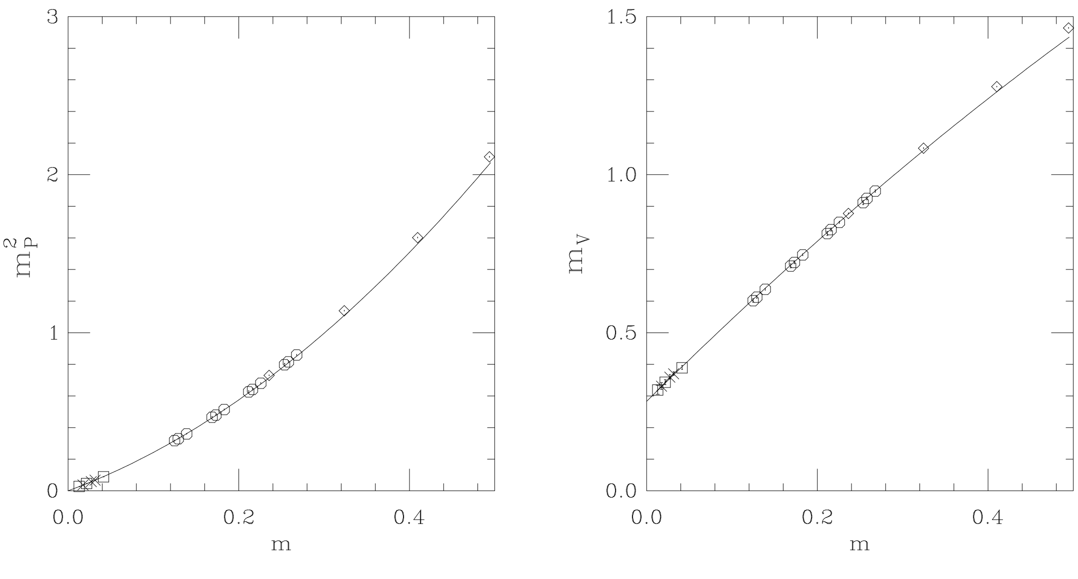

Figure 5.4: The curves of Figure 5.2 and Figure 5.3, extended to include the h-h data of Table 5.4 ($\diamond$).

we do this, we obtain

$$\begin{aligned} m_P^2(\text{all data}):& \quad \chi^2/d.o.f. = 204/18, \\ m_V(\text{all data}):& \quad \chi^2/d.o.f. = 62/18. \end{aligned} \tag{5.100}$$

The fit is almost acceptable for the vector channel, but somewhat wayward for the pseudoscalar. The problem, again, lies at the door of the small errors on the pseudoscalar mass estimates, which are at the 0.1% level for the h-h data.

Thus, although the h-h data seem to fit into the surface extrapolation quite well, the low goodness-of-fit probabilities indicated by the $\chi^2/d.o.f.$ persuade me not to include the h-h points in the final fits quoted in the next section. I would remark, however, that the principle involved appears sound and that the quadratic model function seems to work well. The addition of further terms, perhaps to cubic, might be required to encompass the h-h data with a low $\chi^2/d.o.f.$.

5.3 Charm Quark Mass

In §(4.6) I described how we calculate the κ value corresponding to the lattice strange quark by fixing m_P to the kaon mass. Similarly, in order to calculate meson masses at the charm-quark mass we need to know κ_{ch}. In reference [76], κ_{ch} is chosen so that the corresponding pseudoscalar mass matches approximately the mass of the η_c. For the clover action, this gives $\kappa_{ch} = 0.129$; however, this is only a rough determination. To extract a better estimate, together with a 1000-sample bootstrap distribution for use in subsequent fits, I fit the degenerate h-h m_P^2 data from Table 5.4 to a quadratic form. By analogy with the κ_s determination, I fix m_P^2 to the square of the physical η_c mass and determine κ_{ch} from this.

The result:

$$\kappa_{ch} = 0.12847\,^{+3}_{-2}. \tag{5.101}$$

This is the value I shall use; note that this is derived solely from the h-h data of Table 5.4 and thus does not involve "using up" a mass parameter from our l-l/h-l datasets.

The fit is shown in Figure 5.5 and the fit parameters are listed in Table 5.5. The model curve is a simple quadratic function of the single heavy quark mass:

$$m_P^2 = a_1 + a_2 m + a_3 m^2.$$

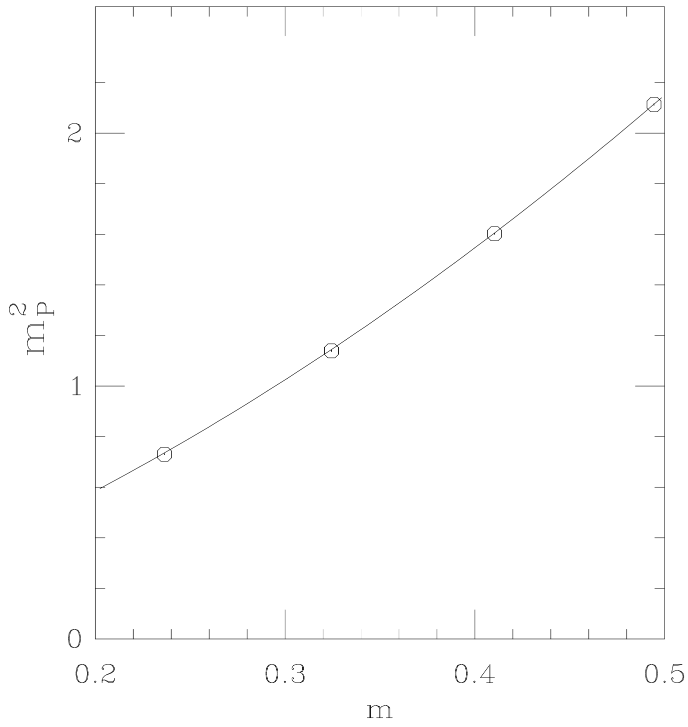

Figure 5.5: Quadratic fit to m_P^2 for the four heavy-heavy data of Table 5.4.

	a_1	a_2	a_3	$\chi^2/d.o.f.$
m_P^2	$-0.049\,^{+4}_{-6}$	$2.35\,^{+3}_{-3}$	$4.10\,^{+4}_{-4}$	10.3/1

Table 5.5: Quadratic fit parameters for the heavy-heavy pseudoscalar mass.

Since here the concern is with obtaining the best *inter*polation between the data points, I do not constrain a_1 to be zero, as would be the case were I interested in the chiral behaviour. Even so, because of the small errors on the data points, the $\chi^2/d.o.f.$ is poor. However, this determination is still significantly more precise than the *ad hoc* choice of 0.129.

In the next section I shall quote mass estimates for the $(c\bar{c})$ mesons η_c and J/Ψ, based only on the *l-l*/*h-l* extrapolations. Figure 5.4 indicates that extrapolating the fit surface towards larger m is not an unreasonable thing to do, although it also suggests that the result will be smaller than that obtained from the *h-h* data

Pseudoscalars		Vectors		κ values
$^{\dagger}m_K$	$0.182\,^{+3}_{-2}$	m_{K^*}	$0.326\,^{+6}_{-5}$	κ_{crit}, κ_s
m_{η_s}	$0.261\,^{+4}_{-3}$	m_ϕ	$0.368\,^{+7}_{-5}$	κ_s, κ_s
m_D	$0.681\,^{+4}_{-4}$	m_{D^*}	$0.713\,^{+3}_{-5}$	$\kappa_{crit}, \kappa_{ch}$
m_{D_s}	$0.721\,^{+3}_{-2}$	$m_{D_s^*}$	$0.752\,^{+3}_{-4}$	κ_s, κ_{ch}
m_{η_c}	$1.08\,^{+1}_{-1}$	$m_{J/\Psi}$	$1.10\,^{+2}_{-1}$	κ_{ch}, κ_{ch}
Splittings				
$m^2_{K^*} - m^2_K$		$0.073\,^{+3}_{-2}$		κ_{crit}, κ_s
$m_{D^*} - m_D$		$0.032\,^{+3}_{-4}$		$\kappa_{crit}, \kappa_{ch}$
$m_{D_s^*} - m_{D_s}$		$0.031\,^{+2}_{-3}$		κ_s, κ_{ch}
$m_{J/\Psi} - m_{\eta_c}$		$0.020\,^{+17}_{-11}$		κ_{ch}, κ_{ch}

Table 5.6: Meson masses and mass-splittings in lattice units extrapolated/interpolated from fits to combined *l-l* and *h-l* data. $^{\dagger}m_K$ is fixed to 493.7 MeV in order to define κ_s.

(our value of κ_{ch} lies close to the second rightmost point on each of the plots in Figure 5.4, $m \sim 0.4$).

5.4 Results from Combined Data Sets

In Table 5.6 I present the masses, in lattice units, of vector and pseudoscalar mesons at various "physical" quark masses. All masses are derived from the fit (B) parameters of Table 5.3. The last column of this table indicates the combination of κ values used in the extrapolation or interpolation of each mass. Note that the mass of the η_c appearing in this table is the result of extrapolating the *l-l*/*h-l* data, *not* the *h-h* number used to fix κ_{ch}. Comparison between the lattice m_{η_c} in physical units and the experimental value provides a check of the accuracy, or otherwise, of the extrapolation of the *l-l*/*h-l* fits into the heavy regime.

For m_{η_s}, m_{K^*} and m_ϕ, the errors are around half those quoted for the *l-l*-only fits in Table 4.10, indicating that the *h-l* data provide a stabilising influence on the

	lattice estimates	experiment	deviation
m_{η_s}	$0.710\,^{+2}_{-2}$ GeV	"0.686 GeV"	$+12.0\sigma$
m_D	$1.85\,^{+2}_{-3}$ GeV	1.870 GeV	-1.0σ
m_{D_s}	$1.96\,^{+2}_{-3}$ GeV	1.969 GeV	-0.5σ
m_{η_c}	$2.94\,^{+5}_{-6}$ GeV	2.979 GeV	-0.8σ
m_{K^*}	$0.884\,^{+1}_{-2}$ GeV	0.892 GeV	-8.0σ
m_ϕ	$0.999\,^{+2}_{-3}$ GeV	1.020 GeV	-10.5σ
m_{D^*}	$1.94\,^{+2}_{-3}$ GeV	2.010 GeV	-3.5σ
$m_{D_s^*}$	$2.04\,^{+2}_{-3}$ GeV	2.110 GeV	-3.5σ
$m_{J/\Psi}$	$2.99\,^{+6}_{-6}$ GeV	3.097 GeV	-1.8σ
$m^2_{K^*} - m^2_K$	$0.538\,^{+2}_{-3}$ $(\mathrm{GeV})^2$	0.55 $(\mathrm{GeV})^2$	-6.0σ
$m_{D^*} - m_D$	$0.087\,^{+7}_{-12}$ GeV	0.14 GeV	-7.6σ
$m_{D_s^*} - m_{D_s}$	$0.083\,^{+5}_{-8}$ GeV	0.141 GeV	-11.6σ
$m_{J/\Psi} - m_{\eta_c}$	$0.05\,^{+5}_{-3}$ GeV	0.118 GeV	-1.4σ

Table 5.7: Meson masses and mass-splittings in physical units.

fit.

The final results, in physical units, using the scale in Equation (5.99), are given in Table 5.7. As with Table 4.11, I indicate the deviation of the lattice result from the experimental value in units of the appropriate errorbar.

Apart from the η_s, all the lattice masses lie below the experimental values. In contrast to Table 4.11, the η_s has risen considerably in mass. The large deviations from experiment for the lighter masses, measured in terms of the corresponding σ's, are disappointing. They arise because of the much smaller errors from the *l-l*/*h-l* fits — smaller by a factor of $\sim$5 compared to Table 4.11. The errorbars belie the fact that, in absolute terms, the *l-l*/*h-l* results for m_{K^*} and m_ϕ are an improvement on the *l-l* data.

The same story applies to the lighter vector-pseudoscalar hyperfine splitting — $m^2_{K^*} - m^2_K$ has risen from 0.53 $(\mathrm{Gev})^2$ to 0.54 $(\mathrm{Gev})^2$, but the smaller errors mean a larger relative deviation.

For the heavier mesons, the relative discrepancies are not so bad and, especially for the pseudoscalar channel, the mass results are extremely encouraging. The larger errors on the η_c and J/Ψ arise from the increasing instability in the extrapolation of the fitting surface to large m; despite having no h-h data in the fit, the results for these heavy mesons are reasonably good. Note that the accuracy of the η_c mass here is a good measure of the validity of the extended extrapolation of the l-l/h-l curve to the charm mass.

The heavier hyperfine splittings are too low by a considerable margin. This has been observed before, and a large part of the discrepancy may be laid at the door of the quenched approximation — see references [75, 76, 77] for detailed discussions of this point. The result for the J/Ψ–η_c splitting agrees with that of $52\,^{+3}_{-4}$ MeV from reference [76], though with much larger errors. Reference [75] quotes $99\,^{+4}_{-7}$ MeV for $m_{D^*} - m_D$ which is comparable with the result here of $87\,^{+\ 7}_{-12}$ MeV.

The small errorbars in the lighter-mass quantities pose something of a problem — should we believe them? I feel the answer must be yes since they are derived from the same bootstrap procedure as all other errors quoted in this work. The bootstrap is known as perhaps the most robust method of error estimation and has a tendency to err on the side of caution in giving larger errors than other procedures.

I suggest, therefore, that the results of this chapter may be giving clear indications of systematic effects in the calculations. Likely candidates include quenching and finite-a effects; for the heavy-quark regime, evidence in, for example, references [75, 76] points a finger in their direction.

The use of combined data in this way, then, gives us a number of results:

1. strong evidence that the meson mass depends only on the sum of quark masses, even in the heavy-light regime;
2. a single functional dependence of meson masses on quark masses spanning different flavour regimes;
3. good estimates for meson masses for a range of quark flavours — u and d through s to c;

4. small errors on these quantities, highlighting possible endemic systematic effects.

These last two are perhaps somewhat contradictory — a "good" estimate indicating systematic errors. However, it is true that the use of the combined l-l/h-l yields better central values for the light vector mesons, while the errors, heavily influenced by the errors on the h-l data are sufficiently small for possible systematics to be seen clearly.

Chapter 6

Summary and Conclusions

The main aim of this work has been the calculation of the hadron spectrum from first-principles QCD. Despite the constraints imposed by the computational model — quenching, a finite cutoff, working in a tiny, periodic box — the results have been good, comparing favourably to other contemporary simulations, and to the ultimate arbiter, Nature.

Quenched lattice calculations are currently in good shape as far as the hadron spectrum goes. The strange-quark sector is directly amenable to simulation, yielding good, clear results, while the light sector, despite the niggles of the chiral extrapolations, is similarly quite robust. The further development of quenched chiral perturbation theory should help us clarify lattice calculations at u and d quark masses.

An interesting aspect of this work is the marriage of the light and heavy-light sectors in a single extrapolation, with the possibility of extension into the heavy-heavy regime. In so far as the lattice-regularised theory can be extended to very heavy quarks, the predictions of masses from this approach have proved to be possible and not inaccurate.

In Figures 6.1 and 6.2 I summarise the meson and baryon mass spectra calculated in this work. It is remarkable, a tribute to the power of the lattice approach and the success of QCD, that we can now reproduce the mass spectrum of the natural world, from the nucleon to the J/ψ meson, from a handful of mathematics.

Obdurate though it may be, QCD holds great rewards for those who would study

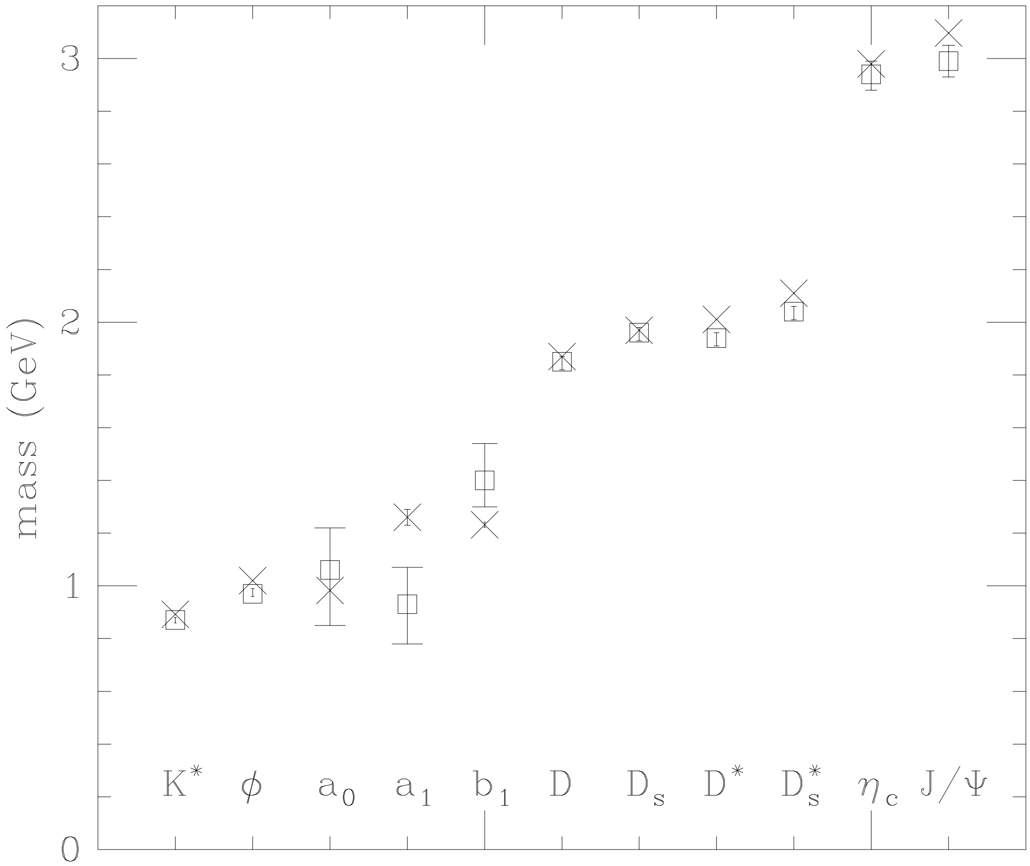

Figure 6.1: Summary plot of the meson spectrum, comparing lattice results (□) with experiment (×).

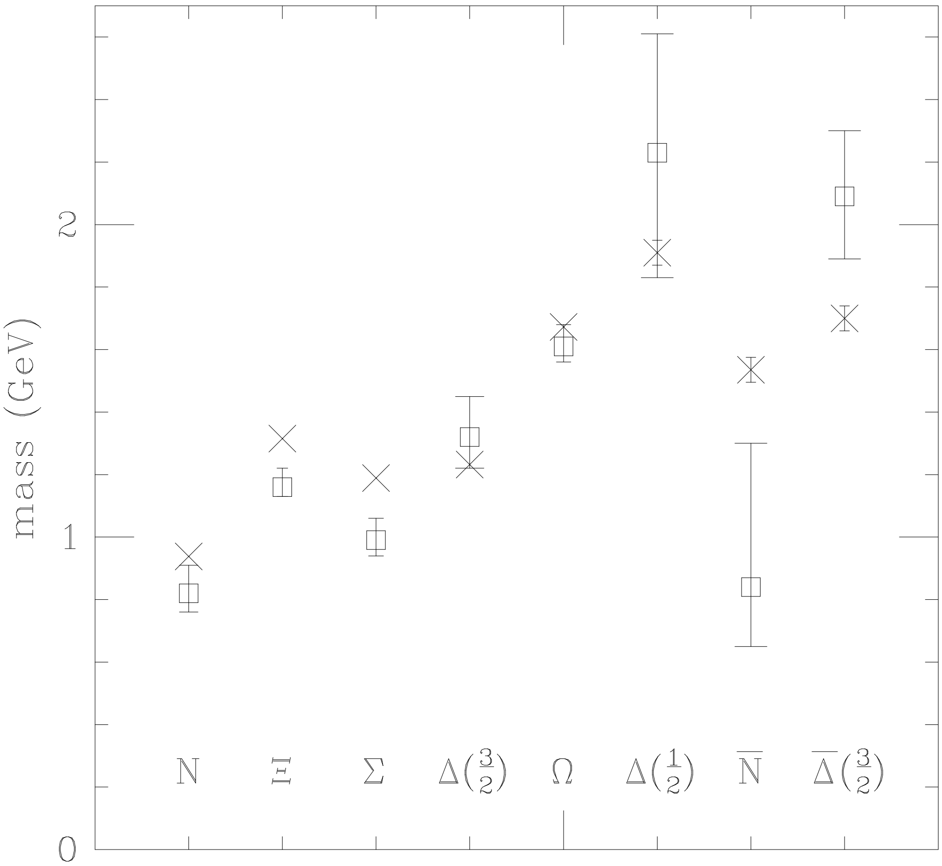

Figure 6.2: Summary plot of the baryon spectrum, comparing lattice results (□) with experiment (×).

it and its basic simplicity sets it alongside Einstein's General Theory of Relativity as worthy of a place out of the shadows, in Plato's world.

Bibliography

[1] D. Gross and F. Wilczek, Phys. Rev. Lett. **30** (1973) 1343.

[2] S. Weinberg, Phys. Rev. Lett. **31** (1973) 494.

[3] H. Fritzsch et al., Phys. Lett. **47 B** (1973) 365.

[4] R.D. Kenway, Rep. Prog. Phys. **52** (1989) 1475.

[5] A.S. Kronfeld, lectures presented at the TASI Summer School *Perspectives in the Standard Model*, Boulder, Colorado, USA, 1991 [Fermilab preprint Fermilab-Conf-92/040-T].

[6] K.G. Wilson, Phys. Rev. **D10** (1974) 2445.

[7] H.B. Nielsen and M. Ninomiya, Nucl.Phys. **B185** (1981) 20.

[8] K.G. Wilson, Adv. Math. **16** (1975) 176.

[9] A.D. Simpson, *Algorithms for Lattice QCD*, Ph.D. thesis, University of Edinburgh (1991).

[10] N. Cabibbo and E. Marinari, Phys. Lett. **119B** (1982) 387.

[11] M. Creutz, Phys. Rev. **D21** (1980) 2308.

[12] A.D. Kennedy and B.J.Pendleton, Phys. Lett. **B156** (1985) 393.

[13] B. Sheikholeslami and R. Wohlert, Nucl.Phys. **B259** (1985) 572.

[14] G. Zweig, CERN report 8419/TH 412 (1964).

[15] See, for example, T-P. Cheng and L-F. Li, *Gauge theory of elementary particle physics*, Oxford (1984) 152.

[16] S.P. Booth, *Applications of Parallel Computers to Particle Physics*, Ph.D. thesis, University of Edinburgh (1991).

[17] A. Ukawa, in *Lattice '92*, Proceedings of the International Symposium, Amsterdam, The Netherlands, 1992, edited by J. Smit and P. Van Baal [Nucl. Phys. B (Proc. Suppl.) **30** (1993) 3].

[18] F. Butler et al., Phys. Rev. Lett. **70** (1993) 2849.

[19] K. Akemi et al., in *Lattice '92* [17] [Nucl. Phys. B (Proc. Suppl.) **30** (1993) 373].

[20] Y. Iwasaki et al., in *Lattice '92* [17] [Nucl. Phys. B (Proc. Suppl.) **30** (1993) 397].

[21] G. Parisi, *Field Theory, Disorder and Simulations*, World Scientific, Singapore (1992).

[22] M. Guagnelli et al., (APE Collaboration), Nucl.Phys. **B378** (1992) 616.

[23] M.-P. Lombardo et al., (APE Collaboration), Ill-(TH)-92-#15 (1992).

[24] C.R. Allton et al., (APE Collaboration), *A High Statistics Lattice Calculation of f_B in the Static Limit on APE*, ROME 93/928 (1993).

[25] C.R. Allton et al. (UKQCD Collaboration), Phys. Lett. **B284** (1992) 377.

[26] C.R. Allton et al. (UKQCD Collaboration), Nucl.Phys. **B**, to be published.

[27] C.R. Allton et al. (UKQCD Collaboration), *The Light Hadron Spectrum and Decay Constants in Quenched Lattice QCD*, Edinburgh Preprint 93/524.

[28] S. Kim and D.K. Sinclair, in *Lattice '92* [17] [Nucl. Phys. B (Proc. Suppl.) **30** (1993) 381].

[29] R. Gupta et al., Phys. Rev. **D43** (1991) 2003.

[30] S. Cabasinio et al., (APE Collaboration), Phys. Lett. **B258** (1991) 202.

[31] P. Bacilieri et al., (APE Collaboration), Nucl.Phys. **B343** (1990) 228.

[32] K.C. Bowler et al., Nucl.Phys. **B220** (1983) 137.

[33] R.D. Kenway, in *Proceedings of the XIIth International Conference on High Energy Physics*, Leipzig, 1984, edited by A. Meyer and E. Wieczorek (Akademie der Wissenschaften der DDR, Zeutben, 1984) 51.

[34] A. Billoire, E. Marinari and G. Parisi, Phys. Lett. **162B** (1985) 160.

[35] P. Bacilieri et al., (APE Collaboration), Phys. Lett. **B214** (1988) 115 and Nucl.Phys. **B317** (1989) 509.

[36] G. Kilcup in *Lattice '88*, Proceedings of the International Symposium, Batavia, Illinois, 1988, edited by A.S. Kronfeld and P.B. Mackenzie [Nucl. Phys. B (Proc. Suppl.) **9** (1989) 201].

[37] V.N.Gribov, Nucl.Phys. **B139** (1978) 1.

[38] E. Marinari, R. Ricci and C. Parinello, in *Lattice '90*, Proceedings of the International Symposium, Tallahassee, Florida, 1990, edited by U.M. Heller, A.D. Kennedy and S. Sanielevici [Nucl. Phys. B (Proc. Suppl.) **20** (1991) 199].

[39] M.L. Paciello et al., Phys. Lett. **B289** (1992) 405.

[40] A. Bartoloni et al., (APE Collaboration), in *Lattice '92* [17] [Nucl. Phys. B (Proc. Suppl.) **30** (1993) 469].

[41] C. Bernard et al., in *Lattice '92* [17] [Nucl. Phys. B (Proc. Suppl.) **30** (1993) 465].

[42] S. Güsken et al., in *Lattice '89*, Proceedings of the International Symposium, Capri, Italy, 1989, edited by R. Petronzio et al. [Nucl. Phys. B (Proc. Suppl.) **17** (1990) 361]
and Phys. Lett. **B227** (1989) 266.

[43] E. Eichten, G. Hockney and H.B. Thacker, in *Lattice '89* [42] [Nucl. Phys. B (Proc. Suppl.) **17** (1990) 529].

[44] C.R. Allton et al. (UKQCD Collaboration), Phys. Rev. **D47** (1993) 5128.

[45] W.H. Press, B.P. Flannery, S.A. Teukolsky and W.T. Vetterling, *Numerical Recipes, The Art of Scientific Computing*, C.U.P (1988) 673–675.

[46] D.S. Henty, *private communication.*

[47] D.S. Henty, *private communication.*

[48] S. Collins, *An Investigation of Hadron Mass Calculations in Lattice QCD*, Ph.D. thesis, University of Edinburgh, 1993.

[49] M. Bochicchio et al., Nucl.Phys. **B262** (1985) 331.

[50] B. Efron, S.I.A.M. Review 21 (1979) 460.

[51] S. Ono, Phys. Rev. **D17** (1978) 888.

[52] H. Lipps et al., Phys. Lett. **126B** (1983) 250.

[53] M. Maiani and G. Martinelli, Phys. Lett. **178B** (1986) 265.

[54] R.D. Loft and T.A. DeGrand, Phys. Rev. **D39** (1989) 2678.

[55] S. Cabasinio et al., (APE Collaboration), Phys. Lett. **B258** (1991) 195.

[56] S.R. Sharpe, talk at the *Workshop on Lattice QCD - Physics and Computing*, Ringberg Castle, Germany, 1993.

[57] A. Abada et al., Nucl.Phys. **B376** (1992) 172.

[58] G. Martinelli et al., Nucl.Phys. **B378** (1992) 591.

[59] 1992 Review of Particle Properties, Phys. Rev. **D45** (1992) II.4.

[60] A. Borelli et al., *New improved operators: a convenient redefinition*, CERN preprint TH.6587/92 (1992).

[61] G.P. Lepage and P.B. Mackenzie, in *Lattice '90* [38] [Nucl. Phys. B (Proc. Suppl.) **20** (1991) 173].

[62] F. Butler et al., *Meson Decay Constant Predictions of the Valence Approximation to Lattice QCD*, IBM preprint IBM-RC-18763.

[63] G. Martinelli et al., *Non-perturbative renormalisation of two-quark operators with an improved lattice fermion action*, in preparation.

[64] J. Gasser and H. Leutwyler, Nucl.Phys. **B250** (1985) 465, and references therein.

[65] M. Lüscher, Commun. Math. Phys. **104** (1986) 177.

[66] J. Gasser and H. Leutwyler, Phys. Lett. **B 184** (1987) 83;
Phys. Lett. **B 188** (1987) 477.

[67] S.R. Sharpe, in *Lattice '89* [42] [Nucl. Phys. B (Proc. Suppl.) **17** (1990) 146].

[68] S.R. Sharpe, Phys. Rev. **D 41** (1990) 3233.

[69] S.R. Sharpe, Phys. Rev. **D 46** (1992) 3146.

[70] C.W. Bernard and M.F.L. Golterman, Phys. Rev. **D 46** (1992) 853.

[71] C.W. Bernard and M.F.L. Golterman, in *Lattice '92* [17] [Nucl. Phys. B (Proc. Suppl.) **30** (1993) 217].

[72] G. Veneziano, Nucl.Phys. **B117** (1976) 519, and references therein.

[73] S.R. Sharpe, in *Lattice '92* [17] [Nucl. Phys. B (Proc. Suppl.) **30** (1993) 213].

[74] For a review of potential models, see W. Lucha et al., Phys. Rep. **200** (1991) 127.

[75] C.R. Allton et al. (UKQCD Collaboration), *Mass Splittings in Heavy-Quark Systems from Quenched Lattice QCD*, Edinburgh preprint 93/523.

[76] C.R. Allton et al. (UKQCD Collaboration), Phys. Lett. **B 292** (1992) 408.

[77] A.X. El-Khadra, in *Lattice '91*, Proceedings of the International Symposium, Tsukuba, Japan, 1991, edited by M. Fukugita at al. [Nucl. Phys. B (Proc. Suppl.) **26** (1992) 372].